General Disclaimer

One or more of the Following Statements may affect this Document

- This document has been reproduced from the best copy furnished by the organizational source. It is being released in the interest of making available as much information as possible.

- This document may contain data, which exceeds the sheet parameters. It was furnished in this condition by the organizational source and is the best copy available.

- This document may contain tone-on-tone or color graphs, charts and/or pictures, which have been reproduced in black and white.

- This document is paginated as submitted by the original source.

- Portions of this document are not fully legible due to the historical nature of some of the material. However, it is the best reproduction available from the original submission.

Produced by the NASA Center for Aerospace Information (CASI)

HEAT TRANSFER LABORATORY
DEPARTMENT OF MECHANICAL AND INDUSTRIAL ENGINEERING
UNIVERSITY OF ILLINOIS AT URBANA-CHAMPAIGN
URBANA, ILLINOIS 61801

SURFACE ROUGHNESS EFFECTS ON BIDIRECTIONAL REFLECTANCE

RECEIVED
AUG 14 1972
JPL TU OFFICE

by

T. F. SMITH

R. G. HERING

(UILU-ENG-72-4001) SURFACE ROUGHNESS EFFECTS ON BIDIRECTIONAL REFLECTANCE T.F. Smith, et al (Illinois Univ.) Jun. 1972 126 p CSCL 20F
N73-12728
Unclas
G3/23 47604

Technical Report No. ME-TR-661-2

UILU-ENG 72-4001

June 1972

Research Supported by
Jet Propulsion Laboratory
California Institute of Technology
under
Contract No. 951661

SURFACE ROUGHNESS EFFECTS ON BIDIRECTIONAL REFLECTANCE

by

T. F. Smith

R. G. Hering

Research Supported by

Jet Propulsion Laboratory

California Institute of Technology

under

Contract No. 951661

This work was performed for the Jet Propulsion Laboratory, California Institute of Technology, sponsored by the National Aeronautics and Space Administration under Contract NAS7-100.

Technical Report No. ME-TR-661-2

UILU ENG 72 4001

Heat Transfer Laboratory

Department of Mechanical and Industrial Engineering

University of Illinois at Urbana-Champaign

Urbana, Illinois 61801

June 1972

FOREWORD

Except for minor changes, this report constitutes the doctoral dissertation of Mr. T. F. Smith which was submitted in partial fulfillment of the requirements for the degree of Doctor of Philosophy in Mechanical Engineering in the Graduate College of the University of Illinois at Urbana-Champaign.

ACKNOWLEDGMENT

This research was sponsored by Jet Propulsion Laboratory, California Institute of Technology, under Contract No. 951661. The JPL Technical Representative early in the program was Mr. Joseph A. Plamondon and, later, Mr. William M. Hagemeyer. The authors wish to acknowledge the many fruitful discussions held with the technical representatives during the course of this study. Others at JPL who contributed valuable advice include Mr. William F. Carroll and Dr. John W. Lucas. Mr. Conrad Mook of NASA Headquarters maintained continued interest in this and other associated studies which were an outgrowth of a program sponsored under NASA Grant NGR-14-005-036.

Certain members of the staff of the Department of Mechanical and Industrial Engineering at the University of Illinois at Urbana-Champaign contributed to the successful completion of this research. Special appreciation is expressed to Professor W. E. Bair, Mr. J. N. Gabbard, and Mr. J. L. Link for their assistance in the design and construction of the bidirectional reflectance facility. Photographs of the facility are attributed to Mr. R. W. Deller. The authors wish to express their appreciation to Professor K. J. Trigger, Dr. B. P. Bardes, and Dr. L. L. Tschopp for their assistance in sample preparation, and to Mr. J. L. Guerrero-Alvarez for acquiring scanning electron microscope photographs of the samples. The authors would like to acknowledge the many helpful discussions with Dr. A. F. Houchens and Mr. W. D. Fischer. The assistance of Mrs. J. Kempka of the Publications Office in preparing this report is gratefully acknowledged.

Finally, the authors would like to acknowledge Mr. D. F. Stevison and Mr. G. L. Denman of Wright-Patterson Air Force Base for their assistance in acquiring surface profile measurements.

ABSTRACT

An experimental study of surface roughness effects on bidirectional reflectance of metallic surfaces is presented. A facility capable of irradiating a sample from normal to grazing incidence and recording plane of incidence bidirectional reflectance measurements was developed. Samples consisting of glass, aluminum alloy, and stainless steel materials were selected for examination. Samples were roughened using standard grinding techniques and coated with a radiatively opaque layer of pure aluminum. Mechanical surface roughness parameters, rms heights and rms slopes, evaluated from digitized surface profile measurements are less than 1.0 μm and 0.28, respectively. Rough surface specular, bidirectional, and directional reflectance measurements for selected values of polar angle of incidence and wavelength of incident energy within the spectral range of 1 to 14 μm are reported. The Beckmann bidirectional reflectance model is compared with reflectance measurements to establish its usefulness in describing the magnitude and spatial distribution of energy reflected from rough surfaces.

The influence of surface roughness on reflectance measurements can be summarized by reference to optical roughness and mechanical rms slope. Optical roughness is defined as the ratio of mechanical rms height to wavelength of incident energy and exhibits values less than unity for the rough surfaces examined. As optical roughness diminishes, rough surface monochromatic reflectances (specular, bidirectional, directional) approach the corresponding values appropriate to those for a smooth surface at the same

direction of incident energy. Specular and directional reflectances decrease as optical roughness increases and are ordered according to mechanical rms slope with smaller reflectance values corresponding to larger rms slope values. Bidirectional reflectances for rough surfaces with nearly identical mechanical rms slopes confirm that as optical roughness increases, the distribution of reflected energy departs from that of a smooth surface to a distribution with significant amounts of reflected energy in directions of reflection other than the specular direction. Bidirectional reflectances for rough surfaces with nearly identical optical roughness values display the same trend as mechanical rms slope increases. Thus, the importance of reporting surface roughness parameters rms height and rms slope is established.

Comparison of the Beckmann model with reflectance measurements reveals the following general conclusions. First, specular and bidirectional reflectance results evaluated from the model using mechanical surface roughness parameters do not agree with the corresponding monochromatic reflectance measurements. Second, a significant improvement between predictions of the model and monochromatic reflectance measurements is observed when optical surface roughness parameters are used in the model. An optical method based on monochromatic specular reflectance measurements for near-normal incidence provided optical rms height and optical rms slope determined for each wavelength of incident energy. Optical roughness is then defined with optical rms height instead of mechanical rms height. Specular reflectance results are evaluated from the model using an average optical rms slope determined from optical rms slopes for each wavelength. Specular reflectance measurements are adequately described by specular reflectance results evaluated from the model when values of optical roughness multiplied

by the cosine of polar angle of incidence are less than 27 times average optical rms slope. Specular reflectance measurements for intermediate to near-grazing polar angles of incidence, however, are not well represented by the model. Bidirectional reflectance results evaluated from the model adequately describe bidirectional reflectance measurements provided optical roughness and optical rms slope are less than 0.05 and 0.02, respectively.

TABLE OF CONTENTS

		Page
1.	INTRODUCTION	1
2.	LITERATURE SURVEY	3
	2.1 OPTICALLY SMOOTH SURFACE	4
	2.2 SMALL OPTICAL ROUGHNESS	5
	2.3 LARGE OPTICAL ROUGHNESS	7
	2.4 SUMMARY OF SURFACE ROUGHNESS EFFECTS	9
3.	BDR FACILITY	11
	3.1 DESCRIPTION OF FACILITY	13
	3.2 METHOD OF MEASUREMENT	20
	3.3 CALIBRATION MEASUREMENTS	24
4.	BDR MODEL	29
	4.1 DESCRIPTION OF BDR MODEL	29
	4.2 DISCUSSION OF BDR MODEL	31
5.	SAMPLE PREPARATION AND SPECIFICATION	39
	5.1 PREPARATION	39
	5.2 SPECIFICATION	41
6.	REFLECTANCE MEASUREMENTS	51
	6.1 SPR MEASUREMENTS	51
	6.2 BDR MEASUREMENTS	66
	6.3 DIRECTIONAL REFLECTANCE MEASUREMENTS	75
7.	EXAMINATION OF A BDR MODEL	85
	7.1 SPR COMPARISON	85
	7.2 BDR COMPARISON	94
8.	SUMMARY AND CONCLUSIONS	102
REFERENCES		107

NOMENCLATURE

dA	differential element of surface area
A_D	detector surface area
ΔA_S	monochromator entrance slit area
$\Delta A_S^-, \Delta A_S^+$	irradiated monochromator entrance slit area for incident and reflected radiation
ΔA_o	source area
a	correlation length
$B, \overline{B}, E, H, \overline{H}, P$	geometrical functions
C	autocorrelation function
F_{sc}	fraction of incident radiation which is scattered by a perfectly conducting material
f_{bd}	bidirectional reflectance for a perfectly conducting material
f_{sc}	scattered component of bidirectional reflectance for a perfectly conducting material
$\overline{f}_{sc}$	scattered component of bidirectional reflectance for a perfectly conducting material of large optical roughness
f_{sp}	specular component of bidirectional reflectance for a perfectly conducting material
G	amplifier gain
I^-, I_r^+	intensity of incident and reflected radiation
$\Delta I_b^-, \Delta I_{b,r}^+$	background intensity for incident and reflected radiation
ΔI_c^+	intensity of radiation emitted by chopper
ΔI_e^+	intensity of radiation emitted by sample
ΔI_s^+	intensity of radiation emitted by shutter
i	summation index
K	parameter containing monochromator, detector, and amplifier factors
M	summation index

m	rms slope
m_m, m_o	mechanical and optical rms slope
N	number of data points
p	probability density function
R	ratio of bidirectional reflectance to that in specular direction
$\overline{R}$	ratio of reflected energy per unit time, area, and solid angle to that in specular direction
S	detector responsivity
U	function defined in Eq. (4.1.7)
$V^-, \Delta V_r^+$	voltage signal for incident and reflected radiation
$\Delta V_b^-, \Delta V_{b,r}^+$	background voltage signal for incident and reflected radiation
$\overline{V}$	ratio of voltage signal for reflected radiation to that in specular direction
x,y,z	spatial coordinates on surface
α	parameter for Dirac delta function
δ	Dirac delta function
θ', θ	polar angle of incident and reflected radiation
θ_{max}	maximum polar angle of reflection for viewing a sample, Eq. (3.2.12)
λ	wavelength
ρ_{bd}	bidirectional reflectance
ρ_{dh}	directional refectance
ρ_s	specular reflectance
$\rho_{s,o}, \rho_{s,r}$	smooth and rough surface specular reflectance
σ	rms height
σ_m, σ_o	mechanical and optical rms height
τ	correlation distance
$\overline{\tau}$	transmittance of optical system

ϕ', ϕ	azimuthal angle of incident and reflected radiation
ω', ω	solid angle of incident and reflected radiation
ω_D	detector solid angle

SUBSCRIPTS

D	detector
m	mechanical
S	slit

SUPERSCRIPTS

+	emergent intensity
-	incident intensity

LIST OF FIGURES

		Page
Figure 3.1	Directions of Incidence and Reflection	12
Figure 3.2	Schematic Diagrams of BDR Facility	14
Figure 3.3	Irradiating Optical System	15
Figure 3.4	Sample Holder and Goniometer System	15
Figure 3.5	Detecting Optical System	16
Figure 3.6	Electronic and Recording System	16
Figure 3.7	Angular Calibration Measurements	27
Figure 4.1	Specular Component from Beckmann BDR Model	32
Figure 4.2	Scattered Component from Beckmann BDR Model for Large Optical Roughness	34
Figure 4.3	BDR Model	36
Figure 5.1	SEM Photographs of Rough Surfaces	42
Figure 5.2	Surface Roughness Profiles	45
Figure 5.3	Roughness Height Probability Density Function and Autocorrelation Function	48
Figure 5.4	SEM Photographs of Profilometer Stylus Scratches	49
Figure 6.1	SPR Measurements for Smooth Samples	52
Figure 6.2	SPR Measurements for Glass Rough Samples	54
Figure 6.3	SPR Measurements for Aluminum Alloy Rough Samples	55
Figure 6.4	SPR Measurements for Stainless Steel Rough Samples	56
Figure 6.5	SPR Measurements for Glass Rough Samples	58
Figure 6.6	SPR Measurements for Aluminum Alloy Rough Samples	59
Figure 6.7	SPR Measurements for Stainless Steel Rough Samples	60
Figure 6.8	SPR Measurements for Glass Rough Samples	63
Figure 6.9	SPR Measurements for Aluminum Alloy Rough Samples	64
Figure 6.10	SPR Measurements for Stainless Steel Rough Samples	65

Page

Figure 6.11 BDR Distributions for Glass Rough Samples 67

Figure 6.12 BDR Distributions for Aluminum Alloy Rough Samples 68

Figure 6.13 BDR Distributions for Stainless Steel Rough Samples 69

Figure 6.14 BDR Distributions for Prescribed rms Slope ($m_m \simeq 0.1$) 74

Figure 6.15 BDR Distributions for Prescribed Optical Roughness ($\sigma_m/\lambda \simeq 0.1$) 76

Figure 6.16 BDR Distributions for Prescribed Optical Roughness ($\sigma_m/\lambda \simeq 0.25$) 77

Figure 6.17 BDR Distributions for Prescribed Optical Roughness ($\sigma_m/\lambda \simeq 0.55$) 78

Figure 6.18 Directional Reflectance Measurements for Aluminum Alloy Rough Samples 80

Figure 6.19 Directional Reflectance Measurements for Stainless Steel Rough Samples 81

Figure 6.20 Directional Reflectance Measurements for Rough Samples 83

Figure 7.1 Optical and Mechanical Surface Roughness Parameters 89

Figure 7.2 Comparison of Beckmann Model with SPR Measurements for Glass Rough Samples 91

Figure 7.3 Comparison of Beckmann Model with SPR Measurements for Aluminum Alloy Rough Samples 92

Figure 7.4 Comparison of Beckmann Model with SPR Measurements for Stainless Steel Rough Samples 93

Figure 7.5 Comparison of Beckmann Model for Different Surface Roughness Parameters with BDR Measurements 96

Figure 7.6 Comparison of Beckmann Model with BDR Measurements for G-3 Sample 98

Figure 7.7 Comparison of Beckmann Model with BDR Measurements for A-3 Sample 99

Figure 7.8 Comparison of Beckmann Model with BDR Measurements for S-7 Sample 100

LIST OF TABLES

Page

Table 3.1 Dimensions for Source Mask and Monochromator Entrance Slits 25

Table 5.1 Abrasive Size, Sample Number, and Surface Topography Parameters 40

Table 7.1 Mechanical and Optical Surface Roughness Parameters 88

1. INTRODUCTION

Placement of man and temperature sensitive equipment aboard spacecraft has created a need for precise spacecraft thermal control. Temperature of a spacecraft in a space environment may be controlled by regulation of radiant heat exchange between spacecraft components and their thermal environment. It is often desirable to determine before flight of a spacecraft radiant heat exchange and, consequently, spacecraft temperature. Radiant heat transfer can be evaluated once the radiative properties of the spacecraft components, spacecraft geometry, thermal environment, and either component temperature or heat flux are specified. The radiative properties are of particular interest in this research. The fundamental radiative property from which all other surface properties can be developed is spectral bidirectional reflectance. This property describes the spatial distribution of radiant energy reflected by a surface which is irradiated by monochromatic radiant energy from a prescribed direction.

Experiments confirm that spectral bidirectional reflectance of an opaque material is strongly dependent upon direction and wavelength of incident energy as well as the surface characteristics. In view of the ranges of interest for directions of incidence and reflection as well as wavelength of incident energy, the number of spectral bidirectional reflectance measurements required for a single surface is enormous. Consequently, it is important to develop bidirectional reflectance models that accurately describe the measurement characteristics. In order to substantiate

these models, however, a limited number of measurements is required. An objective of this research is to acquire spectral bidirectional reflectance measurements for representative opaque engineering materials. In addition, spectral directional reflectance measurements are also reported for the same materials. This radiative property represents the fraction of incident monochromatic radiant energy that is reflected into hemispherical space. A comparison between the measurements and a bidirectional reflectance model is made in order to investigate the accuracy and useful range of the model.

Development of bidirectional reflectance models or presentation of reflectance measurements for engineering materials should be accompanied with information about the surface characteristics. Topographical, chemical, and physical characteristics are commonly used to describe surfaces of engineering materials. Since simultaneous consideration of all these effects is complex, it is useful to assess the influence of each factor separately. Emphasis is placed in this research on the influence of surface topography on spectral bidirectional reflectance. Surface topography information is presented for selected engineering materials for which the previously mentioned reflectance measurements are reported.

In Chapter 2, literature pertinent to this research is reviewed. An experimental facility developed to acquire spectral bidirectional reflectance measurements is described in Chapter 3. A bidirectional reflectance model selected for investigation is reviewed in Chapter 4. In Chapter 5, preparation and specification of test samples are discussed. Spectral reflectance measurements for these test samples are presented in Chapter 6 and compared with a bidirectional reflectance model in Chapter 7. Summary of and conclusions drawn from this research are presented in Chapter 8.

2. LITERATURE SURVEY

Spectral bidirectional reflectance describes the spatial distribution of reflected energy due to irradiation from a prescribed direction by radiant energy within a small wavelength interval about a selected wavelength. For brevity, bidirectional reflectance is denoted by BDR and, unless otherwise stated, all radiative properties are understood to be monochromatic. Experiments [1-11]* confirm that BDR is strongly dependent upon direction and wavelength of incident energy as well as the surface characteristics. Directions of incidence and reflection contained within hemispherical space above a considered surface area element are of interest. The wavelength range of importance is 0.2 to 100 μm since the major contribution of radiant energy as a result of solar irradiation and that emitted by engineering materials at room temperature and higher is found in this wavelength range. Specification of chemical, physical, and topographical characteristics is necessary to describe a surface. Emphasis is given here to the influence of surface roughness on BDR for materials sufficiently thick to be considered opaque. Surface roughness is commonly expressed in terms of root mean square (rms) roughness height [12] measured from a mean surface plane. Typical rms heights for surfaces produced by common engineering production methods are within the range 0.01 to 10 μm [12]. Upon examination of a rough surface profile, it is realized that at least one other parameter is necessary in order to adequately describe the surface contour. An important second parameter is rms slope, and it has received considerably less attention than rms height. Based on reported rms slopes for engineering surfaces, the rms

*Numbers in brackets refer to entries in REFERENCES.

slope range of interest is estimated to be 0.01 to 1.0 [13].

A general discussion of surface roughness effects on BDR has been given by Bennett [14]. Surface roughness effects are generally categorized in terms of optical roughness defined as the ratio of a characteristic roughness height of the surface to a characteristic wavelength of incident energy. If the characteristic height is taken as the rms height and the characteristic wavelength as the wavelength of incident energy, then for the previously cited ranges for these quantities, the optical roughness range of interest is approximately 0.0001 to 50. Unless otherwise stated, reference to surfaces of small and large optical roughness values refer to surfaces with optical roughness values less than and greater than unity, respectively.

Surface roughness effects on BDR are reviewed in three sections. Results for an optically smooth surface are discussed in Section 2.1. In Sections 2.2 and 2.3, results are examined for small and large optical roughness values, respectively. In each section, BDR measurements and models are reviewed. Summary of the literature survey is given in Section 2.4.

2.1 OPTICALLY SMOOTH SURFACE

An optically smooth surface reflects incident energy according to the laws of specular reflection which implies that reflected energy lies in the plane of incidence with identical polar angles of incidence and reflection and with equal solid angles of transfer [15]. Two general classifications of materials are considered, namely, electrical conductors and non-conductors. Measurements [16] confirm that specular reflectance, denoted by SPR, for both materials is nearly independent of direction of incidence for unpolarized energy incident from polar

angles of incidence less than 50 degrees. Furthermore, non-conductors have a relatively small value for SPR at normal incidence (black glass: 0.05) that increases with increasing polar angle of incidence. Conductors have a large value for SPR at normal incidence (aluminum: 0.9) that decreases with increasing polar angle of incidence until grazing incidence is attained.

SPR for an optically smooth, chemically and physically uncontaminated surface can be predicted from solution of the Maxwell equations of electrodynamics. The solution is expressed in terms of the Fresnel equations [17,18]. SPR for unpolarized incident energy is given in terms of polar angle of incidence as well as wavelength dependent material properties called optical constants. Various techniques [19-21] have been employed to evaluate the optical constants from SPR measurements. However, surface damage resulting from surface preparation may cause the optical constants of thin surface layers which are important for radiative properties of materials to differ significantly from those of the bulk material. SPR measurements [14,22] for an electropolished surface are observed to be higher than those for a mechanically polished surface. Surface damage effects, however, are not as important for wavelengths in the infrared.

2.2 SMALL OPTICAL ROUGHNESS

It is convenient to examine surface roughness effects for small optical roughness by investigating their influence on SPR. SPR [4,5, 8,23-27] for small optical roughness exhibits the following characteristics. First, SPR decreases with increasing optical roughness for fixed polar angle of incidence. Thus, as the surface becomes rougher or as the wavelength becomes shorter, the energy observed in the

specular direction decreases. This could be a result of increased scattering by, or multiple reflections within, surface roughness elements. For fixed optical roughness, SPR increases with increasing polar angle of incidence. Thus, the surface becomes more specular as polar angle of incidence increases.

BDR measurements [4-6,8,26-28] for small optical roughness exhibit the following characteristics. For optical roughness values less than 0.05, BDR distributions are similar to those for specular reflection. As optical roughness exceeds this value, greater amounts of reflected energy are observed in directions of reflection other than near the specular direction. For fixed optical roughness, BDR distributions approach those for specular reflection as polar angle of incidence approaches grazing incidence. Furthermore, BDR distributions attain maxima in the specular direction for optical roughness values less than approximately 0.5 [6]. For larger optical values, however, the maxima occur at polar angles of reflection greater than the specular direction.

Theoretical investigations that attempt to describe surface roughness effects on BDR for small optical roughness are based on diffraction effects. Numerous diffraction models have been developed in connection with reflection of radio and radar waves from rough surfaces. A review of these models and relevant literature is available in a book by Beckmann and Spizzichino [29]. Although more recent BDR models have been suggested [30,31], a complete examination of these models in view of engineering application and BDR measurements is lacking. The Beckmann model has been previously examined by Houchens and Hering [32] and shown to have a wider range of engineering application than some other models.

Beckmann developed a model for a perfectly conducting rough surface. Since absorption is absent, the model essentially describes surface roughness effects on the spatial distribution of reflected energy. The rough surface was taken isotropic with a statistical description for the roughness elements. A more detailed description of this model is given in Chapter 4. According to the model, surface roughness parameters that characterize the surface profile are rms height and rms slope. Comparisons [26,28,32] of the Beckmann model with SPR and BDR measurements demonstrate that the model exhibits similar characteristics as the measurements for optical roughness values less than 0.2 and for near-normal incidence. As previously noted [26,32], there are insufficient measurements available for well-documented rough surfaces to substantiate conclusively BDR models for small optical roughness values.

2.3 LARGE OPTICAL ROUGHNESS

Characteristics of SPR measurements for large optical roughness are not as well defined as those for small optical roughness. Toporets [33] reported SPR measurements for polar angles of incidence less than 80 degrees that exhibit the following characteristics. SPR increases with increasing optical roughness for fixed polar angle of incidence. Moreover, for fixed optical roughness, SPR decreases with increasing polar angle of incidence. These characteristics are contrary to those observed for small optical roughness. SPR measurements [34-36] for polar angles of incidence greater than 80 degrees exhibit similar characteristics as those for small optical roughness. BDR measurements [5-8,27,37-39] for large optical roughness exhibit the following characteristics. As optical roughness increases, greater amounts of reflected energy are

found in directions of reflection further removed from the specular direction. The diffuse reflection limit [15] in which the intensity of reflected energy is uniform over hemispherical space is attained only for near-normal incidence [5-7,10,11]. For other than near-normal incidence, BDR distributions exhibit maxima in the plane of incidence at polar angles of reflection greater than the specular direction. As optical roughness increases, these so-called off-specular peaks occur at polar angles of reflection further removed from the specular direction. As polar angle of incidence approaches grazing incidence, BDR distributions are similar to those for specular reflection. BDR measurements reported by Voishvillo [40] for polar angle of incidence of 70 degrees exhibit a peak in the specular direction as well as a smaller peak at polar angle of reflection greater than the specular direction.

Theoretical attempts to develop BDR models that describe the measurements for large optical roughness are formulated using the methods of geometrical optics. As noted by Toporets [36], however, this method applies only for directions of incidence other than near-grazing incidence and diffraction effects must be accounted for in analyses for near-grazing incidence. SPR measurements for polar angles of incidence greater than 80 degrees [34-36] were correlated with an expression similar to that for the specular component of the Beckmann model [32]. BDR models have been developed for surfaces composed of mirror-like roughness elements [13, 39-44] as well as diffusely reflecting roughness elements [44]. The roughness element dimensions are taken large relative to wavelength of incident energy. Although wavelength does not appear in the expressions developed, the models are wavelength dependent since the reflectance of the roughness element surfaces is generally wavelength dependent. For surfaces composed of mirror-like roughness elements, a statistical

distribution function has been utilized to specify the probability that a surface area contains roughness elements of given slope. The roughness parameter employed in the distribution function is related to rms slope. For surfaces composed of diffusely reflecting roughness elements, the roughness element slopes have been assumed equal. Hence, BDR models for large optical roughness are independent of optical roughness. Diffraction models [32,45] for large optical roughness are also expressed only in terms of rms slope. Since a very limited amount of information is available for the rms slope of engineering materials, the importance of this surface roughness parameter for correlating BDR measurements and models has not been established. Comparison of BDR models with measurements have almost always been performed by adjusting the parameters of the models until reasonable agreement is obtained. Comparison [39,42,46] of BDR models [39,41,42] with reported BDR measurements illustrates that the models do exhibit characteristics similar to those of the measurements.

2.4 SUMMARY OF SURFACE ROUGHNESS EFFECTS

This literature survey of surface roughness effects on BDR reveals the following:

1. Experiments confirm that BDR is strongly dependent upon direction and wavelength of incident energy as well as surface topography.
2. At least two surface roughness parameters are necessary to characterize the surface profile, namely, rms height and rms slope. The rms height has received considerably more experimental investigation than rms slope. Both parameters, however, have received theoretical investigation.
3. Surface roughness effects on BDR measurements are conveniently discussed in terms of optical roughness. As optical roughness

approaches zero, the specular reflection limit is reached. Diffuse reflection is attained only for large optical roughness and for near-normal incidence. Off-specular peaks are observed for other than near-normal incidence for large optical roughness.

4. BDR models have been developed by utilizing the concepts of physical and geometrical optics and are applicable to small and large optical roughness values, respectively. BDR models for small optical roughness are expressed in terms of rms height and rms slope, but only rms slope appears in BDR models for large optical roughness.

5. Comprehensive comparisons of analytical models with measurements are lacking. BDR measurements are inadequate both in quantity and scope for confirmation of any BDR model.

3. BDR FACILITY

Before a description of the BDR facility is given, the definition of BDR used in this research is presented. The coordinate system illustrated in Fig. 3.1 aids in defining BDR. Radiant energy incident within solid angle $d\omega'$ about direction θ',ϕ' is reflected by surface area element dA into solid angle $d\omega$ about direction θ,ϕ. BDR which is here denoted by the symbol $\rho_{bd}(\theta',\phi';\theta,\phi)$ is defined as the ratio of intensity of reflected energy to incident energy. Thus,

$$\rho_{bd}(\theta',\phi';\theta,\phi) = \frac{dI_r^+(\theta,\phi)}{I^-(\theta',\phi') \cos\theta' \, d\omega'} \tag{3.1}$$

where $I^-(\theta',\phi')$ and $dI_r^+(\theta,\phi)$ denote intensities of incident and reflected energy, respectively. As noted in Chapter 2, surface roughness effects can be conveniently examined to some extent by reference to SPR. SPR, denoted by the symbol $\rho_s(\theta',\phi')$, is defined as the ratio of reflected intensity in the specular direction ($\theta = \theta', \phi = \phi' + \pi$) to incident intensity.

$$\rho_s(\theta',\phi') = \frac{I_r^+(\theta',\phi' + \pi)}{I^-(\theta',\phi')} \tag{3.2}$$

In addition to SPR, directional reflectance also aides in examination of surface roughness effects. Directional reflectance is defined as the ratio of energy reflected into hemispherical space to incident energy. In terms of BDR, this property is expressed as follows

$$\rho_{dh}(\theta',\phi') = \int_\omega \rho_{bd}(\theta',\phi';\theta,\phi) \cos\theta \, d\omega \tag{3.3}$$

where the integration is over all solid angles of reflection.

Examination of reported BDR measurements and models as discussed

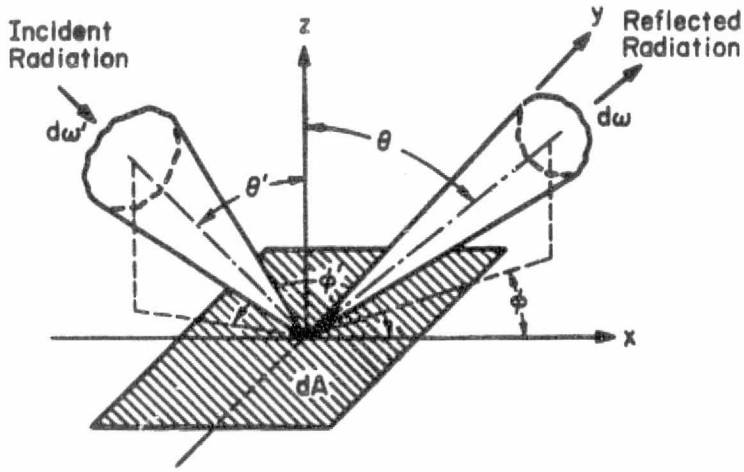

Figure 3.1 Directions of Incidence and Reflection

in Chapter 2 reveals that considerable information about the validity of the surface roughness parameters as suggested by the measurements and models can be obtained from plane of incidence BDR measurements. Furthermore, the added complexity of BDR facilities [47,48] for recording measurements outside the plane of incidence is not justified for the present investigation. Consequently, a facility capable of acquiring plane of incidence BDR measurements was developed. The plane of incidence is formed by direction of incident energy and the mean surface normal. Azimuthal angle of reflection ϕ, therefore, assumes the values of ϕ' and $\phi' + 180$ degrees. It was noted in Chapter 2 that there are insufficient BDR measurements available to substantiate application of any small optical roughness BDR model. Therefore, BDR measurements were acquired within the spectral interval 1 to 14 μm where the small optical roughness results are expected to be applicable.

3.1 DESCRIPTION OF FACILITY

Schematic diagrams of the BDR facility are presented in Fig. 3.2. The reflectometer consists of an irradiating optical system, sample holder and goniometer system, detecting optical system, and electronic and recording system. The systems are composed of numerous components whose general arrangement may be observed by reference to photographs in Figs. 3.3, 3.4, 3.5, and 3.6. Descriptions of the systems as well as their components follow. More detailed information about some of the components is available elsewhere [49-54].

The irradiating optical system (Fig. 3.3) consists of source, shutter, and mirrors. Supports for these components are attached to the source arm. A globar housed in a water cooled jacket and powered by a regulated power supply provides a source of radiant energy. A

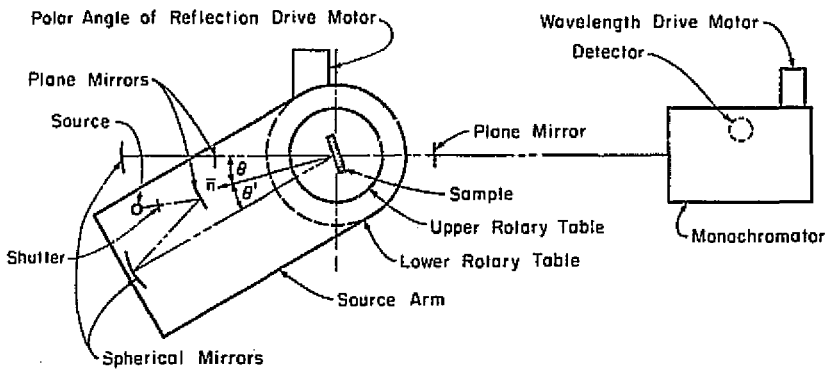

(a) Top View

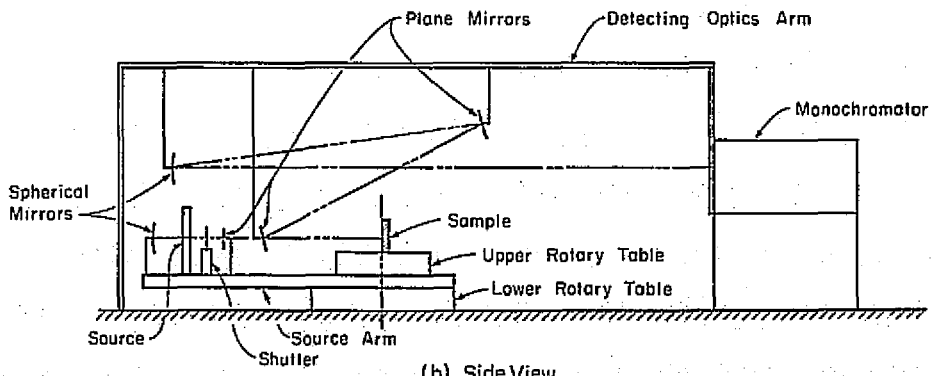

(b) Side View

Figure 3.2 Schematic Diagrams of BDR Facility

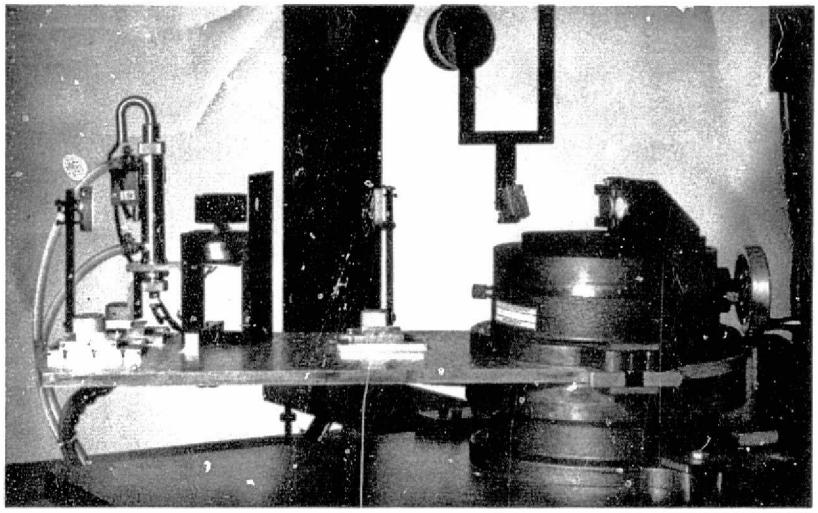

Figure 3.3 Irradiating Optical System

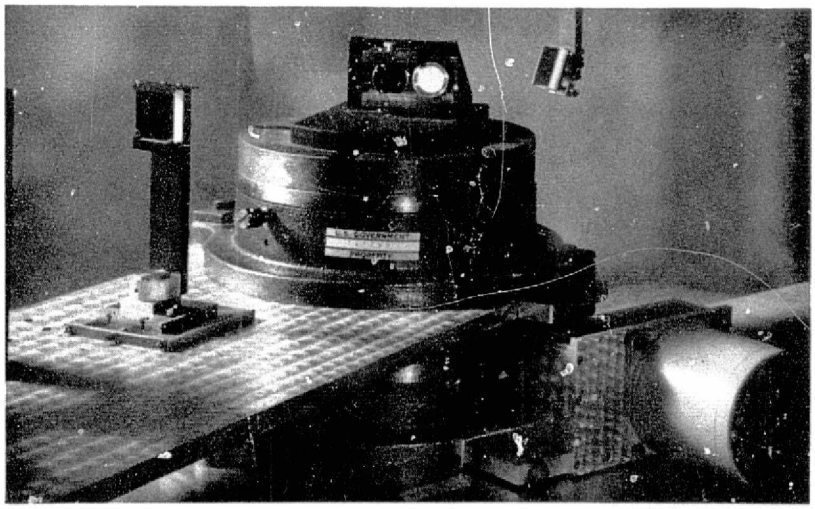

Figure 3.4 Sample Holder and Goniometer System

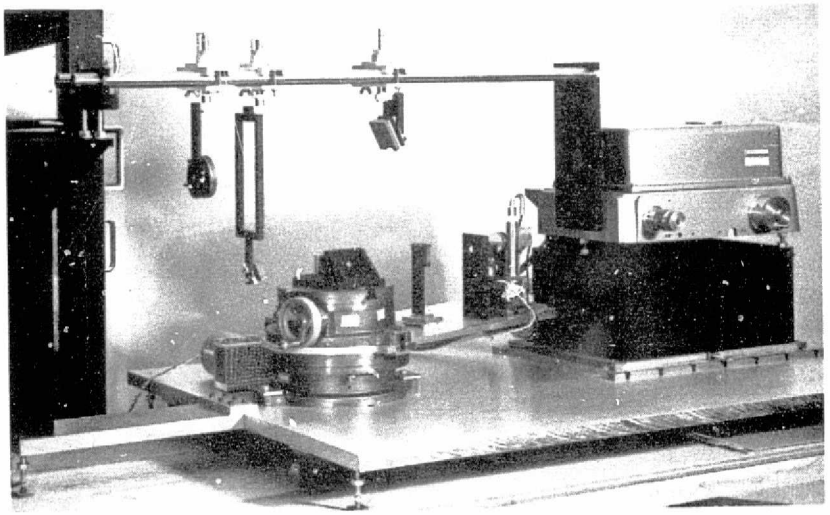

Figure 3.5 Detecting Optical System

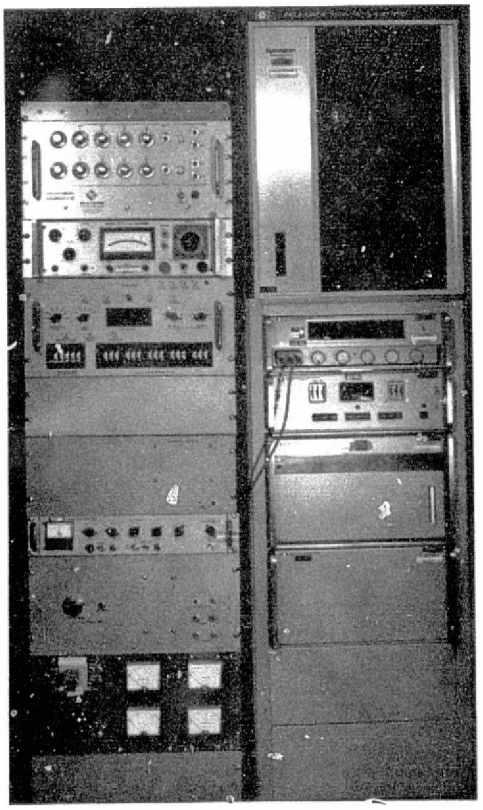

Figure 3.6 Electronic and Recording System

shutter attached to a rotary solenoid allows elimination of sample irradiation by the radiant energy source when background radiation measurements are recorded. The rotary solenoid is activated by a voltage signal from the control interface which is described later. Emitted energy of the source is focused on the sample by a plane mirror and a spherical mirror. The spherical mirror has a diameter of 40.5 mm and a radius of curvature of 462.15 mm. Solid angle of incident energy is determined by the spherical mirror and has a value of 0.0060 steradians.

The sample holder and goniometer system are shown in Fig. 3.4. The sample holder is designed so that the front surface of a plane mirror sample conincides with the axis of rotation of the goniometer. The goniometer consists of two coaxial rotary tables. The sample holder is affixed to the rotary portion of the upper table. The source arm is rigidly connected to both the base of the upper rotary table and the rotating element of the lower rotary table. Polar angles of incidence θ' from normal incidence ($\theta' = 0$ degrees) to grazing incidence ($\theta' = 90$ degrees) are manually set to an accuracy of ± 0.025 degrees with the upper rotary table. Azimuthal angle of incidence ϕ' is varied by rotation of the sample about its normal. A 200 step per revolution Slo-Syn driving motor is employed to scan over polar angle of reflection θ by driving the lower rotary table through a speed reducer. One step of the motor is equivalent to 0.01 degree change of the θ angle. A Slo-Syn two-axis preset indexer that is activated by the control interface drives this motor. Azimuthal angle of reflection ϕ is altered by scanning over θ and passing from one side to the other side of the mean surface normal of the sample.

The detecting optical system (Fig. 3.5) is stationary and consists of mirrors, monochromator, and detector. Radiant energy reflected by the

sample is focused on the entrance slits of a monochromator by two plane mirrors and a spherical mirror. In order to allow continuous scanning throughout the plane of incidence and reduce blockage of incident energy, these mirrors are suspended from an arm rigidly attached to the monochromator. Supports for these mirrors are positioned so that interference with the irradiating optical system components is eliminated as the source arm is rotated. The plane mirror that views reflected energy from the sample is contained in the plane of incidence. Blockage of incident energy by this mirror is confined to a 16 degree angular interval centered at the direction of incident energy ($\theta = \theta'$, $\phi = \phi'$). The spherical mirror has a diameter of 71.4 mm and a radius of curvature of 820.0 mm. Solid angle of reflection is controlled by the spherical mirror and has a value of 0.0060 steradians.

A Perkin-Elmer Model 99 monochromator with sodium chloride prism is employed to provide spectral measurements. An internal chopper is utilized to interrupt the light beam. An erratic reference signal from the chopper was corrected by replacement of the original chopper motor and mechanical system that furnished the reference signal to the lock-in-voltmeter with a synchronous motor and photodiode system, respectively. The photodiode system consists of a stationary narrow light beam, a semicircular blade attached to the chopper shaft, and a stationary photodiode. The alternating voltage signal from the photodiode provides synchronization of the lock-in-voltmeter with the reference signal. Wavelength calibration of the monochromator drum was aided by attaching a 200 step per revolution Slo-Syn driving motor to the wavelength drum shaft. The preset indexer previously mentioned also drives this motor.

A thermocouple detector mounted inside the monochromator is employed to transform the cyclic radiant energy incident on the detector into a cyclic voltage signal. By adjustment of a plane mirror located beyond the exit slits of the monochromator, blockage of the radiant energy by the detector was eliminated.

The electronic and recording system is shown in Fig. 3.6. The uppermost instrument in the left-hand rack is the Slo-Syn two-axis preset indexer. Below the indexer, in the order in which they appear in the photograph, are the lock-in-voltmeter, control interface, background shutter control, photomultiplier tube power supply, reference signal control, and source power supply. A Hewlett-Packard Model 2012B digital data acquisition system is located in the rack to the right in Fig. 3.6. Function of these instruments is briefly discussed.

The cyclic voltage signal generated by the thermal radiation detector is amplified by a Brower Laboratories Model 131 Lock-in-Voltmeter. This instrument consists of a preamplifier located near the thermal radiation detector and the main amplifier shown in Fig. 3.6. The output of the amplifier is digitized and recorded by the digital data acquisition system. Raw data is recorded on magnetic tape and reduced as well as analyzed with the aid of a digital computer.

Activation of the preset indexer and data acquisition system is the function of the control interface. The interface was built using integrated circuits and other standard electrical components. The interface has the capability of independently stepping the wavelength drive motor and the polar angle of reflection drive motor. At each position of these motors, there is a time delay before activation of the recorder in order to allow the detector and amplifier to respond to the change in

radiant energy signal. The output voltage signal of the amplifier may be recorded up to ten times when noise levels are high. Background radiation measurements may be recorded by activation of the rotary solenoid. Two modes of operation are possible, namely, wavelength scan or angle scan. In the wavelength scan mode, the set of five thumbwheel switches to the left in Fig. 3.6 is used to preset the desired number of total steps of the wavelength drive motor. In the angle scan mode, the set of thumbwheel switches to the right is used. Provisions have been incorporated in the control interface to record data at small angular increments for directions of reflection where the reflectometer signal is expected to vary rapidly (for example, near the specular direction) and at large angular intervals in regions where the signal changes slowly. Angular increments of 0.01, 0.02, 0.05, 0.1, 0.2, 0.5, 1.0, and 2.0 degrees are available.

3.2 METHOD OF MEASUREMENT

The relation between BDR and output voltage signal of the lock-in-voltmeter is determined by first considering the signal observed when the radiant energy incident on the sample is viewed directly. To perform this measurement, the goniometer is adjusted by setting polar angles of incidence and reflection to 0 and 180 degrees, respectively, and removing the sample holder. The amplifier voltage signal may be expressed as

$$V^- = G \int_{\lambda} \int_{\omega_D} \int_{A_D} S(\lambda, A_D)\, \overline{\tau}(\lambda)\, (I^- - \Delta I_c^+ + \Delta I_b^-) \cdot \cos\theta_D'\, dA_D\, d\omega_D\, d\lambda \qquad (3.2.1)$$

where the Δ-symbol is used here and throughout this section to denote a small but finite quantity. The amplifier is assumed to have a linear

response with gain G. S denotes the detector responsivity. Reflectance and transmittance of the optical components are represented by $\overline{\tau}$. I^- and ΔI_c^+ represent the intensities of radiant energy of the source and chopper, respectively. Emission by the optical components, stray energy and equivalent stray electrical signals are represented by ΔI_b^-. θ_D' is the polar angle for radiant energy incident on the detector and A_D is the irradiated detector area. Radiant energy incident on the detector is contained within solid angle ω_D. For sufficiently small wavelength interval $\Delta\lambda$ about the wavelength of interest, the factors S, $\overline{\tau}$, I^-, ΔI_c^+, and ΔI_b^- may be considered independent of λ within $\Delta\lambda$. Furthermore, for radiant energy contained within a small solid angle $\Delta\omega_D$ about θ_D', the intensities and polar angle of incidence may be assumed to vary imperceptibly within $\Delta\omega_D$. Since the solid angle of reflection $\Delta\omega$ is the limiting solid angle of the reflectometer, $\Delta\omega_D = \Delta\omega$. For sufficiently small irradiated detector area, S, I^-, ΔI_c, and ΔI_b^+ can be assumed independent of location within ΔA_D. The irradiated entrance slit area of the monochromator ΔA_S^- determines the size of the irradiated detector area and is hereafter referred to in the analysis. Taking into account the preceding observations, the integrations indicated in Eq. (3.2.1) can be performed to yield

$$V^- = K(I^- - \Delta I_c^+ + \Delta I_b^-)\ \Delta A_S^-\ \Delta\omega \tag{3.2.2}$$

where $K(=GS\,\overline{\tau}\cos\theta_D'\ \Delta\lambda)$ depends principally on λ.

When the source emission is blocked by the shutter, the voltage signal is due to emission by the shutter, chopper, and optical components as well as stray energy and electrical signals. The background voltage signal is then given by

$$\Delta V_b^- = K(\Delta I_s^+ - \Delta I_c^+ + \Delta I_b^-)\ \Delta A_S^-\ \Delta\omega \tag{3.2.3}$$

where ΔI_s^+ is the intensity of radiant energy emitted by the shutter. Subtraction of Eq. (3.2.3) from Eq. (3.2.2) yields

$$V^- - \Delta V_b^- = K(I^- - \Delta I_s^+)\, \Delta A_S^-\, \Delta\omega \tag{3.2.4}$$

Replacement of the sample holder and adjustment of the goniometer to the desired directions of incidence and reflection, the voltage signal due to reflected energy from the sample is given as

$$\Delta V_r^+(\theta,\phi) = K[\rho_{bd}(\theta',\phi';\theta,\phi)\, I^- \cos\theta'\Delta\omega' - \Delta I_c^+ + \Delta I_{b,r}^+(\theta,\phi) + \Delta I_e^+(\theta,\phi)]\, \Delta A_S^+\, \Delta\omega \tag{3.2.5}$$

where $\Delta I_e^+(\theta,\phi)$ is the intensity of radiant energy emitted by the sample. $\Delta I_{b,r}^+(\theta,\phi)$ is the background intensity and is considered a function of direction of reflection. ΔA_S^+ is the irradiated entrance slit area which is not necessarily equal to ΔA_S^-. Blockage of the source yields a voltage signal due to shutter, chopper, background, and sample intensities.

$$\Delta V_{b,r}^+(\theta,\phi) = K[\rho_{bd}(\theta',\phi';\theta,\phi)\, \Delta I_s^+ \cos\theta'\Delta\omega' - \Delta I_c^+ + \Delta I_{b,r}^+(\theta,\phi) + \Delta I_e^+(\theta,\phi)]\, \Delta A_S^+\, \Delta\omega \tag{3.2.6}$$

Subtraction of Eq. (3.2.6) from Eq. (3.2.5) yields

$$\Delta V_r^+(\theta,\phi) - \Delta V_{b,r}^+(\theta,\phi) = K\rho_{bd}(\theta',\phi';\theta,\phi)[I^- - \Delta I_s^+] \cdot \cos\theta'\Delta\omega'\Delta A_S^+\, \Delta\omega \tag{3.2.7}$$

The ratio of Eq. (3.2.7) to Eq. (3.2.4) gives an expression for BDR in terms of recorded voltage signals.

$$\rho_{bd}(\theta',\phi';\theta,\phi) = \frac{1}{\cos\theta'\Delta\omega'}\left[\frac{\Delta V_r^+(\theta,\phi) - \Delta V_{b,r}^+(\theta,\phi)}{V^- - \Delta V_b^-}\right]\frac{\Delta A_S^-}{\Delta A_S^+} \tag{3.2.8}$$

The relation between ΔA_S^- and ΔA_S^+ is now discussed.

There are fundamentally two methods by which the irradiated sample area can be viewed by the entrance slits of the monochromator. In the first method, hereafter called overviewing, the entrance slits view an area on the sample larger than the irradiated area. For this arrangement, the relation between ΔA_S^- and ΔA_S^+ is

$$\Delta A_S^+ = \Delta A_S^- \cos\theta/\cos\theta' \tag{3.2.9}$$

where ΔA_S^- is the irradiated sample area for normal incidence which is also the source area. $\Delta A_S^-/\cos\theta'$ is the entrance slit area. Equation (3.2.8) can then be written as

$$\rho_{bd}(\theta',\phi';\theta,\phi) = \frac{1}{\cos\theta\Delta\omega'}\left[\frac{\Delta V_r^+(\theta,\phi) - \Delta V_{b,r}^+(\theta,\phi)}{V^- - \Delta V_b^-}\right] \tag{3.2.10}$$

In the second method, called underviewing, the entrance slits view an area on the sample smaller than the irradiated area. For this method, the entrance slits are fully irradiated and $\Delta A_S^+ = \Delta A_S^-$. Equation (3.2.8) thus becomes

$$\rho_{bd}(\theta',\phi';\theta,\phi) = \frac{1}{\cos\theta'\Delta\omega'}\left[\frac{\Delta V_r^+(\theta,\phi) - \Delta V_{b,r}^+(\theta,\phi)}{V^- - \Delta V_b^-}\right] \tag{3.2.11}$$

The maximum polar angle of reflection such that the entrance slits are fully irradiated is

$$\theta_{max} = \cos^{-1}[\cos\theta'\Delta A_S/\Delta A_o] \tag{3.2.12}$$

where ΔA_S is the entrance slit area which is smaller than the source area ΔA_o. θ_{max} may also be limited by the sample area since the detector should not view an area larger than the sample area for this method.

Since the difference between the incident and reflected energy voltage signals can be many orders of magnitude, it is more convenient to make relative measurements between signals of the same order of magnitude and then perform only a limited number of absolute measurements. For a given wavelength and direction of incidence, BDR measurements are normalized with respect to that obtained in the specular direction. The normalized relations between BDR and voltage signals are written as follows for the two viewing methods.

Overviewing

$$R \cos \theta / \cos \theta' = \overline{V} \tag{3.2.13a}$$

Underviewing

$$R = \overline{V} \tag{3.2.13b}$$

where

$$R = \frac{\rho_{bd}(\theta',\phi';\theta,\phi)}{\rho_{bd}(\theta',\phi';\theta',\phi' + \pi)} \tag{3.2.14a}$$

and

$$\overline{V} = \frac{\Delta V_r^+(\theta,\phi) - \Delta V_{b,r}^+(\theta,\phi)}{\Delta V_r^+(\theta',\phi' + \pi) - \Delta V_{b,r}^+(\theta',\phi' + \pi)} \tag{3.2.14b}$$

For BDR measurements that are presented in Chapter 6, the overviewing method was utilized for polar angles of incidence of 10, 30, and 60 degrees and the underviewing method for polar angle of incidence of 80 degrees. The source and monochromator entrance slit dimensions for the various polar angles of incidence are given in Table 3.1.

3.3 CALIBRATION MEASUREMENTS

The wavelength of radiant energy emerging from the monochromator exit slits is determined by the wavelength drum setting [54]. Spectral calibration of the drum was obtained by observing the well-documented

Table 3.1

Dimensions for Source Mask and Monochromator Entrance Slits

θ', degrees	Source Mask, mm		Monochromator Entrance Slits, mm	
	Width	Height	Width	Height
10	1.90	3.43	2.075	12
30	1.50	3.33	2.075	12
60	0.71	3.33	2.075	12
80	6.35	19.0	2.000	6.35

emission and absorption spectra of various substances. The emission lines of a mercury arc lamp were observed for calibration in the 1.0 to 2.3 μm spectral range and absorption lines of water vapor, carbon dioxide, and polystyrene film in the 2.3 to 15 μm spectral range. Wavelength identification of these lines was determined by comparison of observed lines with those available elsewhere [54-57]. Slit widths as recommended in the cited references were used for the calibration measurements. Using a least-square technique similar to that of Fryer [58] to fit a curve through the drum position-wavelength data, a table of drum number versus wavelength was generated. This technique yielded a wavelength accuracy of ±0.025 μm. The spectral bandwidth of radiant energy is centered about the wavelength and is determined by the slit width. For slit widths shown in column 4 of Table 3.1, the bandwidth is approximately 0.08 μm at a wavelength of 1 μm, 0.35 μm at 3.0 μm, and 0.09 μm at 14 μm. These bandwidths are not expected to significantly influence the accuracy of the measurements since BDR does not change rapidly with wavelength within the considered spectral range.

Angular alignment of the reflectometer was verified by observing

the angular distribution of incident energy as well as that reflected from a plane mirror sample. Figure 3.7 displays measurements for wavelength of 2.3 μm and for polar angles of incidence of 0, 10, 30, 60, and 80 degrees. The radial coordinate $\overline{R}$ is given by Eq. (3.2.13a). Measurements for polar angle of incidence of 80 degrees have been multiplied by the factor $\cos\theta/\cos\theta'$. Angular alignment measurements for other wavelengths are similar to those reported in Fig. 3.7 and, consequently, are not presented. Data for polar angle of incidence of 0 degrees correspond to incident energy measurements, and these have been rotated by 180 degrees for presentation in this figure. Incident energy measurements were acquired by adjustment of the reflectometer as discussed in Section 3.2. The maxima of the distributions occur at polar angle of reflection within 0.1 degrees of $\theta = 180$ degrees for incident energy and of $\theta = \theta'$ for the plane mirror sample. Further verification of the optical alignment as well as accuracy and repeatability of the measurements was obtained by comparing these measurements with results from a geometrical optics analysis [42] of the irradiating and detecting optical systems. Good agreement is shown in Fig. 3.7 between the data and the geometrical optics results which are represented by solid curves. Due to the finite size solid angles, the reflectometer applies a broadening factor to reflectance of specularly reflecting samples and as displayed in Fig. 3.7, causes a spread of the measurements and analytical results. For infinitesimally small solid angles, $\overline{R}$ would have a value of unity for each polar angle of incidence.

The relation between BDR and voltage signal was verified by measuring BDR of a diffusely reflecting sample made from sulfur flowers [59]. These measurements are also displayed in Fig. 3.7 for a wavelength of

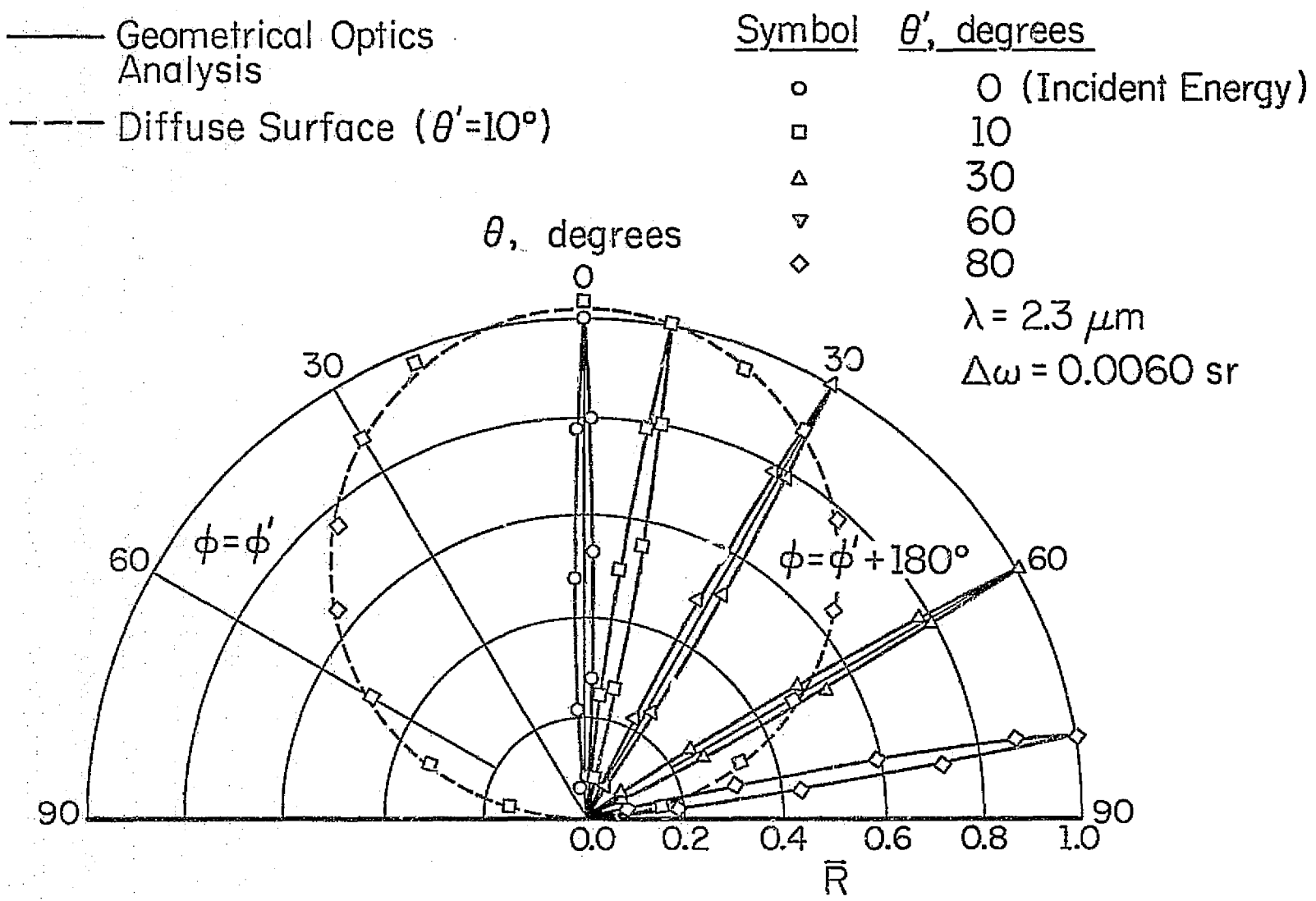

Figure 3.7 Angular Calibration Measurements

2.3 μm and polar angle of incidence of 10 degrees. A diffuse surface has an $\overline{R}$ distribution given by $\cos\theta/\cos\theta'$ and is represented in this figure by the broken curve. Good agreement between measurements and theory for a diffuse surface is shown.

It should be noted that the data points displayed in Fig. 3.7 are taken from a larger set of measurements for each case. Measurements for the plane mirror sample were recorded at 1 degree angular intervals for $\theta' - 10^\circ \leq \theta \leq \theta' - 2^\circ$ as well as $\theta' + 2^\circ \leq \theta \leq \theta' + 10^\circ$ and at 0.1 degree intervals for $\theta' - 2^\circ < \theta < \theta' + 2^\circ$. For the sulfur sample, measurements were recorded at 2 degree angular intervals. The time required to record the former set of measurements for each polar angle of incidence was approximately 15 minutes but for the latter, 50 minutes was necessary. Tests were performed to evaluate variation of source output and electronic drift over the time interval necessary to acquire the measurements. Results showed that the source output and drift varied less than 2 percent for the larger time interval. Since shorter time intervals were used for the measurements presented in Chapter 6, the source variation and drift is not expected to significantly influence the accuracy of BDR measurements.

4. BDR MODEL

The BDR model selected for comparison with reflectance measurements reported in Chapter 6 is attributed to Beckmann [29]. Houchens and Hering [32] examined this model in view of certain theoretical criteria and demonstrated that it has a wider range of engineering application than some other physical optics models. It is not the purpose here to discuss this model at length, but to present some results that are pertinent to later comparisons. Detailed development and discussion are available elsewhere [29,32]. In Section 4.1, a description of the model is presented,and representative results are reported in Section 4.2.

4.1 DESCRIPTION OF BDR MODEL

Beckmann developed a model for a perfectly conducting, randomly rough surface with negligible shadowing by, and multiple reflections within, adjacent roughness elements. Since absorption is absent, the model essentially describes the influence of surface roughness on the spatial distribution of reflected energy. According to the model, the surface roughness parameters that influence BDR are rms height σ and rms slope m. Optical roughness is then defined as σ/λ where λ is the wavelength of incident energy. The general form of the Beckmann model can be written as follows

$$f_{bd}(\theta',\phi';\theta,\phi) = f_{sp}(\theta')\, U(\theta',\phi';\theta,\phi) + f_{sc}(\theta',\phi';\theta,\phi) \qquad (4.1.1)$$

The symbol f_{bd} denotes BDR for a perfectly conducting material. f_{sp} is referred to as the specular component with U designating that this component contributes to f_{bd} only in the direction of specular reflection. f_{sc} is called the scattered component and it describes the spatial

distribution of energy reflected throughout hemispherical space. Specific expressions for f_{sp} and f_{sc} are given by [60]

$$f_{sp}(\theta') = \exp\{-[4\pi(\sigma/\lambda)\cos\theta']^2\} \tag{4.1.2}$$

$$f_{sc}(\theta',\phi';\theta,\phi) = \frac{2\pi(\sigma/\lambda)^2 B \exp\{-[(\sigma/\lambda) E]^2\}}{\cos\theta\cos\theta' m^2} \cdot \sum_{M=1}^{\infty} \frac{[(\sigma/\lambda) E]^{2M}}{M(M!)} \exp\left[\frac{-2\pi^2}{M}\frac{(\sigma/\lambda)^2 H}{m^2}\right] \tag{4.1.3}$$

where

$$B = \left[\frac{1 + \cos\theta\cos\theta' + \sin\theta\sin\theta'\cos(\phi' - \phi)}{\cos\theta + \cos\theta'}\right]^2 \tag{4.1.4}$$

$$E = 2\pi(\cos\theta + \cos\theta')$$

$$H = \sin^2\theta + \sin^2\theta' + 2\sin\theta\sin\theta'\cos(\phi' - \phi) \tag{4.1.5}$$

rms slope is related to correlation length a by the relation

$$m = \sqrt{2}\,(\sigma/a) \tag{4.1.6}$$

The expression for U introduced in Eq. (4.1.1) is

$$U(\theta',\phi';\theta,\phi) = 2\delta[\sin^2\theta' - \sin^2\theta]\,\delta[\phi' - (\phi' \pm \pi)] \tag{4.1.7}$$

where $\delta(\alpha)$ is the Dirac delta function for parameter α.

For large optical roughness ($\sigma/\lambda \gg 1$), the specular component is zero for all but near-grazing incidence and Eq. (4.1.3) reduces to the following [60].

$$\overline{f}_{sc}(\theta',\phi';\theta,\phi) = \frac{\overline{B}}{2\pi m^2\cos\theta\cos\theta'} \exp\left[-\frac{\overline{H}}{2m^2}\right] \tag{4.1.8}$$

where

$$\overline{B} = \frac{B}{(\cos\theta + \cos\theta')^2} \tag{4.1.9}$$

$$\overline{H} = \frac{H}{(\cos\theta + \cos\theta')^2} \tag{4.1.10}$$

Note that the expression for $\overline{f}_{sc}$ is independent of wavelength and depends only on a single surface roughness parameter rms slope.

4.2 DISCUSSION OF BDR MODEL

Portions of the following discussion of the Beckmann BDR model have been extracted from [60] and are repeated here for reference purposes. Since the Beckmann BDR model applies to perfectly conducting material, all incident energy must be accounted for in the reflected energy leaving the surface. According to the model, reflected energy is represented by the specular and scattered components. The fraction of energy incident from direction θ',ϕ' which is accounted for by the scattered component $F_{sc}(\theta',\phi')$ may be evaluated by integrating the product of f_{sc} and the cosine of the polar angle of reflection over all solid angles of reflection

$$F_{sc}(\theta',\phi') = \int_{\omega} f_{sc}(\theta',\phi';\theta,\phi) \cos\theta \, d\omega \tag{4.2.1}$$

The sum of the fraction of incident energy from direction θ',ϕ' accounted for by the specular and scattered components should be unity.

$$f_{sp}(\theta') + F_{sc}(\theta',\phi') = 1 \tag{4.2.2}$$

It has been shown [42] that the conservation of energy requirement expressed by Eq. (4.2.2) is usually satisfied within a few percent if rms slope is restricted to values less than about 0.14. However, the magnitude of the discrepancy depends on the value of optical roughness, rms slope, and polar angle of incidence.

Typical results for the specular component are illustrated in Fig. 4.1 where $f_{sp}(\theta')$ distributions are shown for selected values of optical roughness. For prescribed direction of incidence, the specular component decreases with increasing optical roughness. With optical

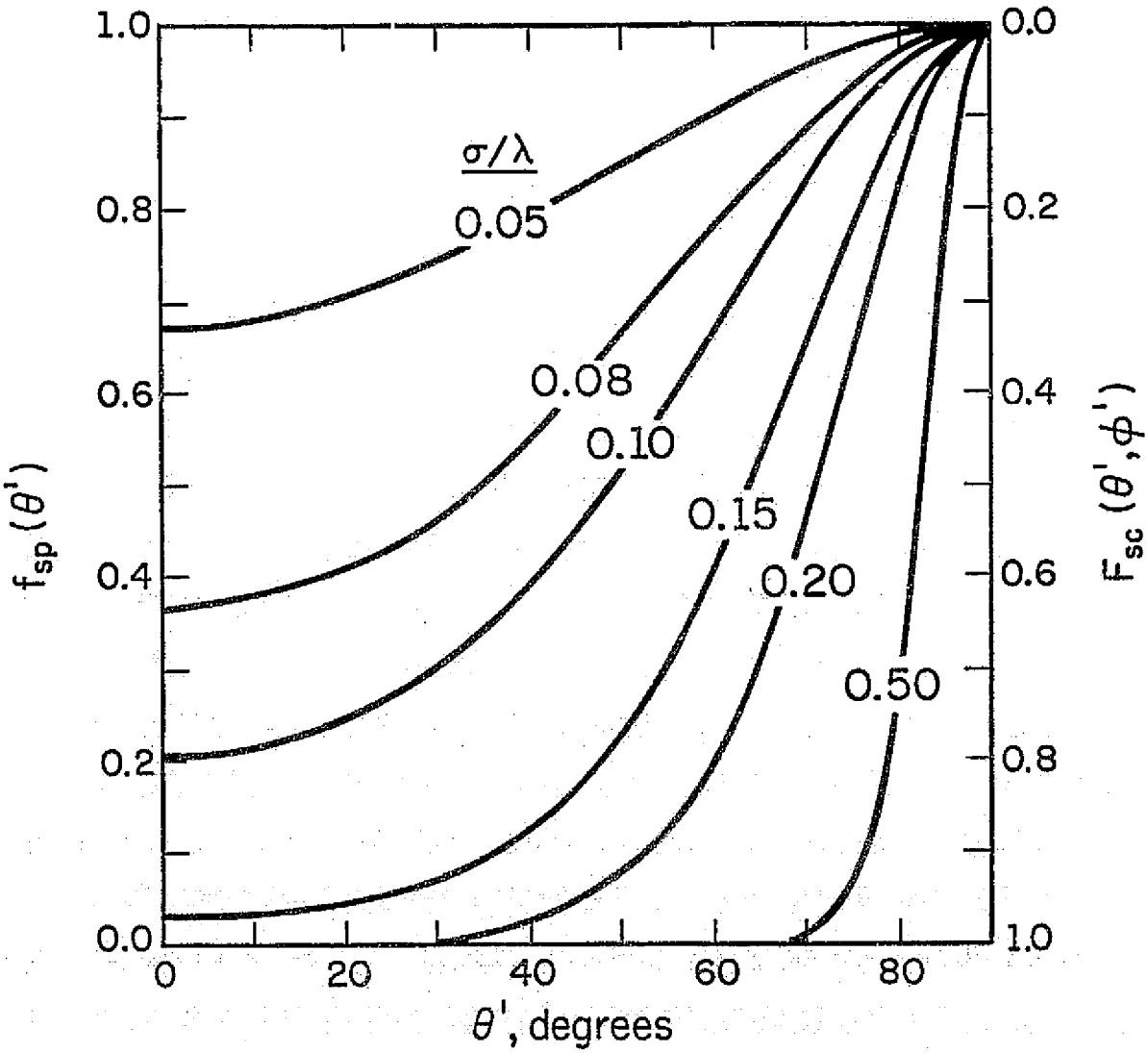

Figure 4.1 Specular Component from Beckmann BDR Model

roughness prescribed, the specular component increases with increasing polar angle of incidence. Since, according to Eq. (4.2.2), the factor $[1 - f_{sp}(\theta')]$ represents the fraction of incident energy which is scattered, $F_{sc}(\theta',\phi')$, the right-hand ordinate in Fig. 4.1 may be used to evaluate this quantity for a surface of prescribed optical roughness irradiated from a specific direction. Apportionment of reflected energy between the specular and scattered components is determined by polar angle of incidence and optical roughness.

With direction of incident energy and value of optical roughness specified, the magnitude of the scattered energy is fixed. Its spatial distribution is uniquely determined by rms slope. The general influence of rms slope on the scattered component is similar for all polar angles of incidence and values of optical roughness. Some representative results are illustrated in Fig. 4.2. The product of the scattered component for large optical roughness and cosine of polar angle of reflection is shown versus polar angle of reflection for normal irradiation and rms slope values of 0.040, 0.057, 0.094, and 0.14. The product of BDR and cos θ is the fraction of incident energy reflected per unit time and per unit area into a unit solid angle around the direction of reflection. No azimuthal angles are indicated on the figure since for normal irradiation BDR is azimuthally symmetric. A diffusely reflecting surface is represented in the figure by the dashed curve. The angular spread about the specular direction within which the scattered energy is significant increases with increasing rms slope. The increasing angular spread of the scattered energy is accompanied with a reduction of BDR in the specular direction. Thus, the surface tends toward a diffusely reflecting surface as rms slope increases. Even for the

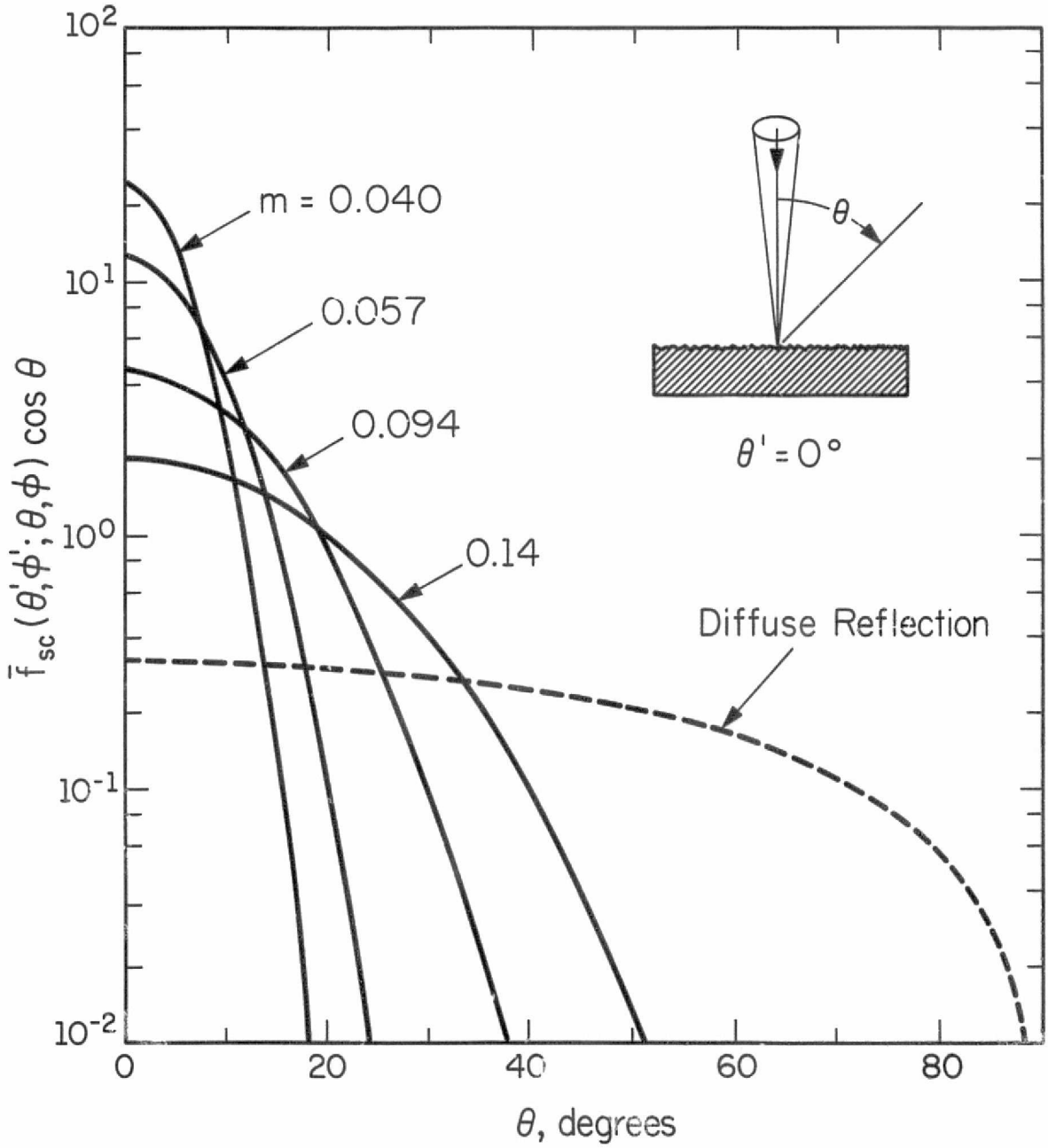

Figure 4.2 Scattered Component from Beckmann BDR Model for Large Optical Roughness

largest value of rms slope ($m = 0.14$), however, the spatial distribution of reflected energy differs significantly from that for diffuse reflection.

For a fixed value of rms slope, the dependence of the spatial distribution of scattered energy on direction of incidence is markedly different for large and small values of optical roughness. The product of the scattered component and $\cos\theta$ for rms slopes equal to 0.094 and 0.14 is shown in Fig. 4.3 versus polar angle of reflection for large optical roughness ($\sigma/\lambda \gg 1$) and a small value of optical roughness ($\sigma/\lambda = 0.1$). For each value of optical roughness, distributions are shown for polar angles of incidence equal to 0, 20, 45, and 60 degrees, and for each polar angle of incidence results are shown for selected values of azimuthal angle of reflection.

Consider the distributions for rms slope equal to 0.14. It is important to note the strong reflection of energy into the plane containing the specular direction (strong forward scattering). For large optical roughness, (Fig. 4.3a), the maximum value of $\bar{f}_{sc} \cos\theta$ increases sharply, and the angular spread of the scattered energy around the specular direction decreases for increasing polar angle of incidence. Of particular note is the rapid decrease of energy scattered out of the plane of incidence with increasing polar angle of incidence. For small optical roughness, (Fig. 4.3b), the maximum value of $f_{sc} \cos\theta$ decreases with increasing polar angle of incidence due to the increasing magnitude of the incident energy which undergoes specular reflection. In contrast to the distributions for large optical roughness, the lobes of scattered energy in the plane of incidence for small optical roughness and moderate to large polar angles of incidence are not centered about the specular direction

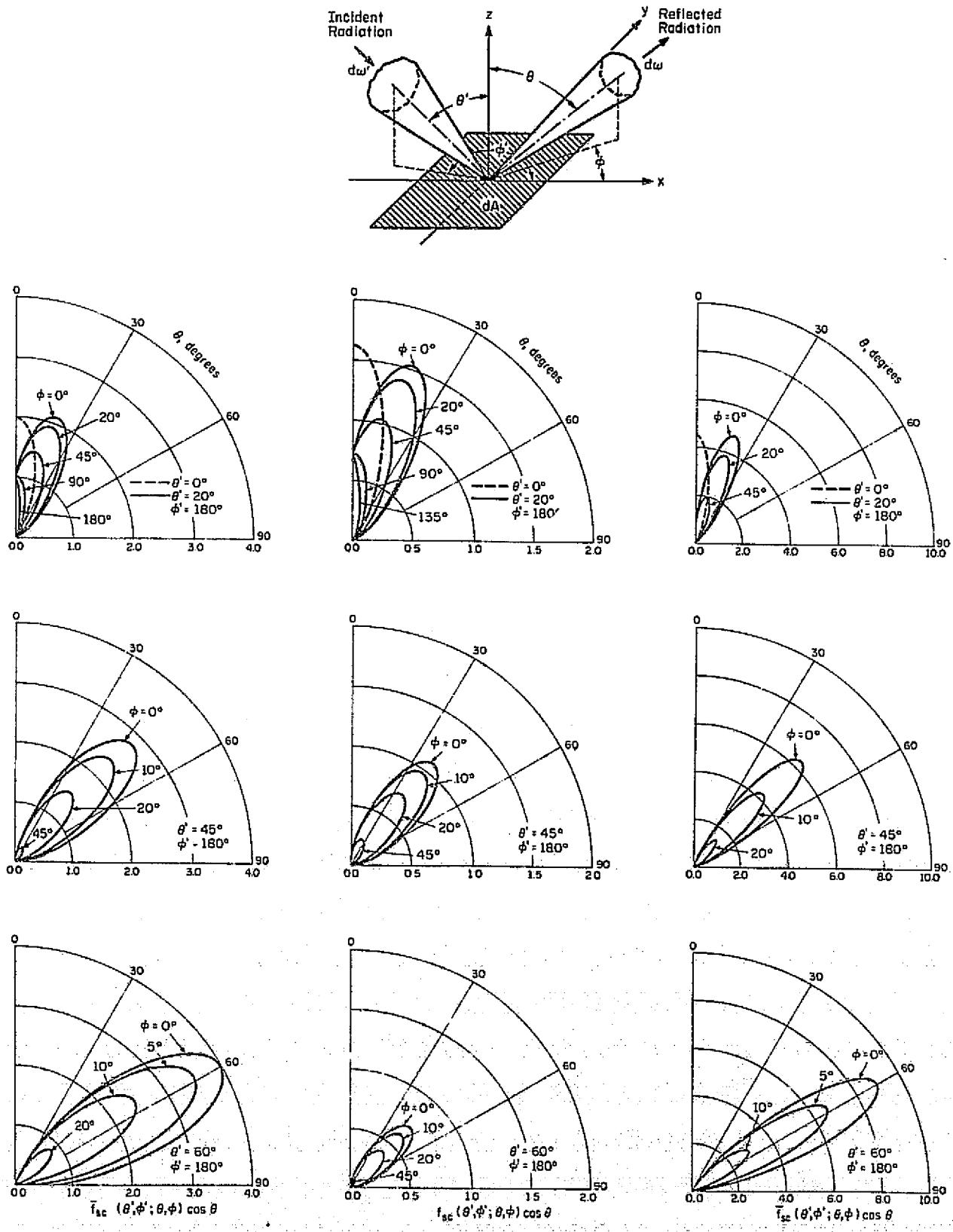

(a) Large optical roughness, m = 0.14

(b) σ/λ = 0.1
m = 0.14

(c) Large optical roughness, m = 0.094

Figure 4.3 BDR Model

but are shifted toward the surface normal.

It should be noted that the scattered component contains a singularity for polar angle of reflection equal to 90 degrees. This accounts for the generally small, but finite, value of the product $f_{sc} \cos \theta$ for grazing reflection. This error results from neglecting shadowing effects in the derivation of BDR.

Since the Beckmann model is limited to perfectly conducting surface, it is necessary to modify Eq. (4.1.1) for application to engineering materials. The approximate method employed here to account for energy absorption consists of multiplying the perfect conductor relation by SPR of a smooth surface of the same material [25,29]. BDR of an engineering material is then expressed as

$$\rho_{bd}(\theta',\phi';\theta,\phi) = \rho_{s,o}(\theta',\phi')\, f_{bd}(\theta',\phi';\theta,\phi) \tag{4.2.3}$$

where $\rho_{s,o}(\theta',\phi')$ denotes smooth surface SPR.

In Chapter 7, the BDR model is compared with rough surface SPR measurements by utilizing the following expression for SPR

$$\frac{\rho_{s,r}(\theta',\phi')}{\rho_{s,o}(\theta',\phi')} = f_{sp}(\theta') + f_{sc}(\theta',\phi';\theta',\phi' + \pi) \cos \theta' \, \Delta\omega$$

$$= \exp\{-[(\sigma/\lambda)P]^2\} + \frac{\Delta\omega(\sigma/\lambda)^2 P}{2m^2} \exp\{-[(\sigma/\lambda) P]^2\}$$

$$\cdot \sum_{M=1}^{\infty} \frac{[(\sigma/\lambda) P]^{2M}}{M(M!)} \tag{4.2.4}$$

where $\rho_{s,r}(\theta',\phi')$ is rough surface SPR and $P = 4\pi \cos \theta'$. In Eq. (4.2.4), the first term on the right-hand side is the specular component and the second term is the contribution of the scattered component to energy reflected into the specular direction. Birkebak [61] presented an expression

for the second term that includes an extra multiplicative factor $4/\cos^2 \theta'$.

5. SAMPLE PREPARATION AND SPECIFICATION

In this chapter, test samples selected for this research are discussed. Sample preparation is presented in Section 5.1. Specification of surface characteristics for the test samples is discussed in Section 5.2.

5.1 PREPARATION

Shape, size, and distribution of roughness elements on surfaces of engineering materials are influenced by the material mechanical properties as well as the method of surface preparation. These effects may be partially investigated by selection of test samples of different materials and utilization of different abrasive sizes for surface preparation. Test samples consisted of glass, 6061-T6 aluminum alloy, and 303 stainless steel discs. Glass samples were 2 mm thick with a 27 mm diameter and were purchased with a smooth finish. Metallic samples were 6 mm thick with a 25 mm diameter. The influence of "as received" condition for the metallic samples was eliminated by polishing one face of the metallic discs to a smooth finish utilizing a 0.5 μm diamond paste as the abrasive. One smooth surface sample of each material was retained and the other samples were roughened with abrasives that consisted of 6 μm diamond paste, 1000 grit silicon carbide powder, and 600, 400, 320, 240, 180, as well as 120, grit silicon carbide paper. The abrasive used in roughening each sample and corresponding sample number are shown in columns 1, 2, 3, 6, and 9 of Table 5.1. The G-1, A-1, and S-1 samples are referred to as the smooth samples. All samples were ultrasonically cleaned and then coated with a vacuum deposited layer of pure aluminum to a thickness of approximately 0.1 μm. Specification of surface characteristics for the test samples is discussed in

Table 5.1

Abrasive Size, Sample Number, and Surface Topography Parameters

Average Abrasive Size[1]		Sample Substrate Material								
		Glass			Aluminum Alloy			Stainless Steel		
Grit	μm	Number	σ_m [2]	m_m [3]	Number	σ_m	m_m	Number	σ_m	m_m
		G-1			A-1			S-1		
	6				A-2	0.0570	0.0238			
1000	8.5				A-3	0.145	0.0443	S-8	0.496	0.0300
600	17.5	G-5	0.837	0.142	A-4	0.286	0.101	S-2	0.109	0.0410
400	23	G-2	0.270	0.0834	A-5	0.314	0.104	S-3	0.134	0.0395
320	30	G-3	0.358	0.108	A-6	0.751	0.190	S-4	0.240	0.0536
240	60	G-4	0.374	0.133	A-9	0.987	0.216	S-6	0.279	0.0798
180	80				A-8	0.804	0.178	S-5	0.251	0.0883
120	110	G-6	0.927	0.274	A-7	0.794	0.156	S-7	0.368	0.105

[1]Relation between grit size and average micrometer size was obtained from [62].

[2]σ_m--mechanical rms height, μm.

[3]m_m--mechanical rms slope.

the succeeding section.

5.2 SPECIFICATION

It is common practice to describe the surface finish of engineering materials in terms of the chemical, physical, and topographical characteristics of the surface [14,63,64]. As mentioned in the previous section, test samples were coated with a 0.1 μm thick layer of pure aluminum. For this layer thickness, the sample retains the roughness topography of the substrate material while providing a radiatively opaque surface of high electrical conductivity with the well-documented optical properties of pure aluminum [65]. Upon exposure to an atmospheric environment, an aluminum oxide film of approximately 25 Å thickness [66] forms on the aluminum film. Bennett [66] reported that the decrease in SPR for a 25 Å aluminum oxide film formed on an aluminum film is less than 0.1 percent for wavelengths longer than 0.9 μm. Thus, the oxide film is not expected to significantly effect reflectance measurements.

Qualitative surface topography information was obtained from scanning electron microscope (SEM) secondary electron emission photographs as displayed in Fig. 5.1 for selected samples. Photographs for a magnification of 1000 X represent a sample area approximately 100 μm wide, whereas those for a magnification of 10,000 X correspond to a 10 μm wide area. The width of the irradiated sample area for reflectance measurements is greater than the width of the sample area shown in the photographs for the lower magnification by at least a factor of seven. No preferential orientation of roughness was evident when other areas of the sample were viewed with the SEM. In each photograph the electron intensity profile is illustrated for a position indicated by the tick marks

1000 X Magnification | 10,000 X Magnification

(a) 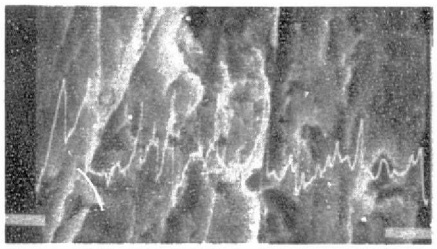 G-6 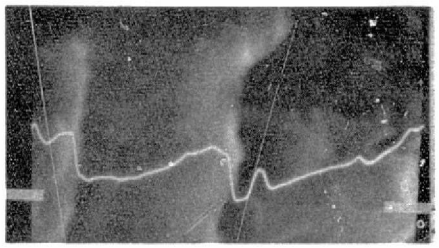 (b)

(c) 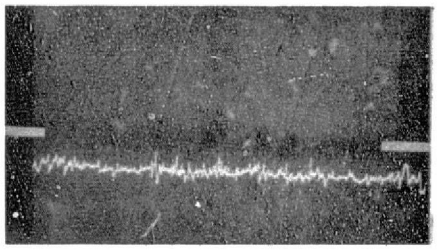 A-2 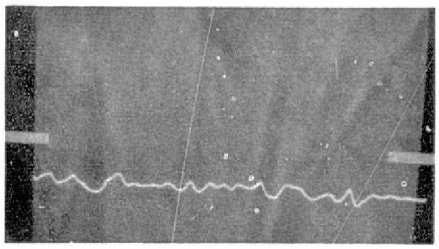 (d)

(e) 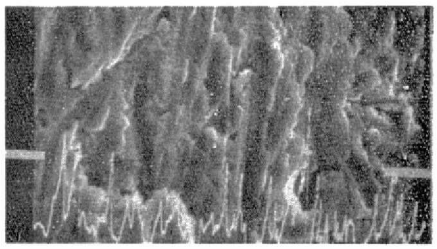 A-9 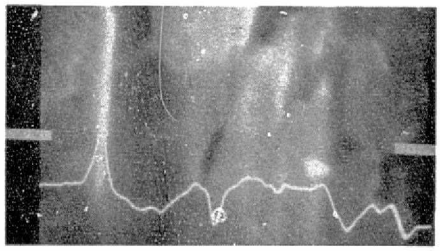 (f)

(g) S-7 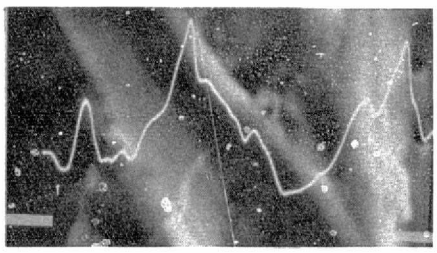 (h)

(i) 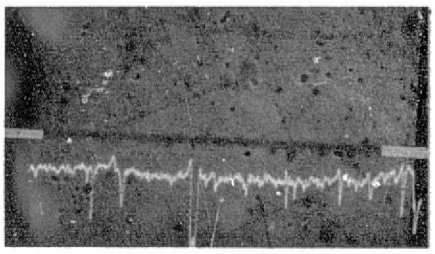 S-8 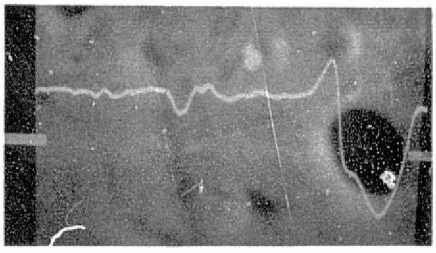 (j)

Figure 5.1 SEM Photographs of Rough Surfaces

located on the sides of the photographs. The dark line observed on some photographs is due to residual electrical charge on the surface when a single scan was recorded for the electron intensity profile. The surface roughness profile cannot be directly inferred from the intensity profile since sharp edges yield disproportionately more intense intensity signals. Analysis of stereopair photographs from an SEM can provide quantitative evaluation of surface topography parameters [67]. This procedure was not utilized in this study, however. According to the photographs, the A-2 sample has the smoothest finish and the G-6 and A-9 samples have the roughest finish for the sample photographs shown. The surface of the S-8 sample consists of numerous pits of less than 3 μm diameter that are separated by relatively smooth areas. These characteristics may influence the reflection properties of this sample.

Surface roughness parameters for the test samples were evaluated from surface profile measurements recorded with a Talysurf Model 3 profilometer attached to a digital data acquisition system [68]. The profilometer has a 2.5 μm radius stylus. The voltage signal corresponding to the vertical displacement of the stylus was digitized and recorded on magnetic tape for computer analysis. The horizontal position for each digitized vertical position was derived from information concerning the horizontal speed of the stylus drive and the digitizing rate of the data acquisition system. A total of 2,897 vertical positions equally spaced within a horizontally traversed distance of 3.01 mm was acquired for each surface profile scan. One scan in the vicinity of the irradiated surface area was recorded for each sample.

Surface roughness parameters could be evaluated directly from the recorded profiles,but it is more convenient to use the mean surface plane as a reference. The mean surface plane was determined by using a least-squares technique to fit a first order polynomial to the profiles [69]. The resulting linear equation represents the mean surface plane. For convenience of computation and presentation, a transformation was applied to the recorded profiles so that the mean surface plane coincides with the x-axis of an x-z Cartesian coordinate system and the z-axis corresponds to the height of the rough surface as measured from the mean surface plane. Graphical display of the transformed profiles revealed that some of the surfaces exhibited waviness. Waviness could be caused by slight movement of the sample as the profile was recorded. It was necessary to repeat some of the scans because sample movement was noticed while recording the profile. A least-squares technique was used to fit a second order polynomial to the transformed profiles that exhibited waviness. Surface roughness profiles for samples that exhibited waviness were obtained by subtraction of waviness as described by the second order polynomial from the transformed profiles. Representative portions of surface roughness profiles for selected samples are shown in Fig. 5.2 where the ordinate z represents roughness height. Surface roughness parameters were evaluated from analysis of these as well as similar profiles for other samples.

It was noted in Chapter 2 that rms height and rms slope represent two surface roughness parameters that are necessary to characterize a rough surface profile. These parameters were evaluated from the surface roughness profiles using the following expression for rms height

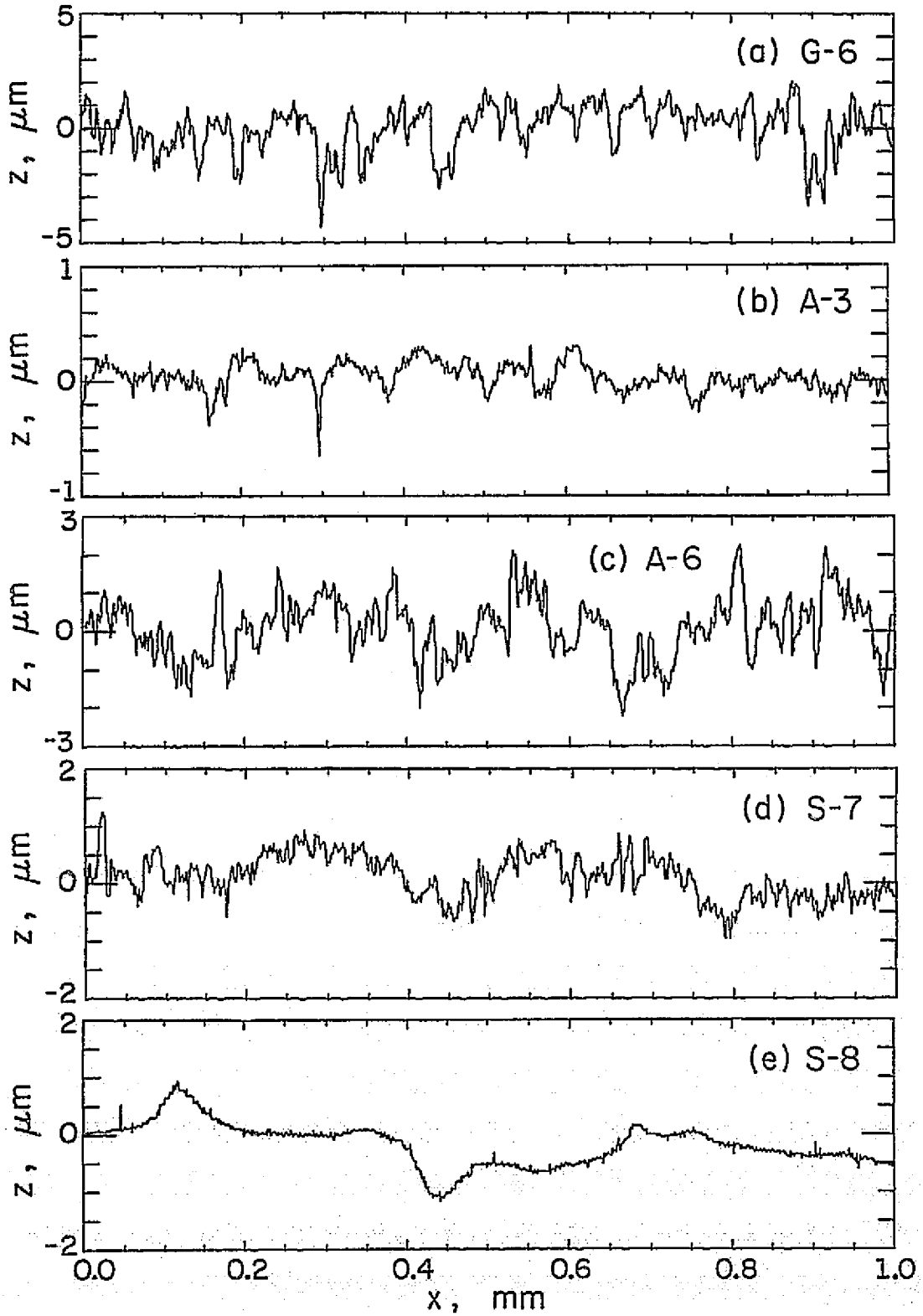

Figure 5.2 Surface Roughness Profiles

$$\sigma_m = \left[\frac{1}{N-1} \sum_{i=1}^{N} (z_i)^2 \right]^{1/2} \tag{5.2.1}$$

and the following expression for rms slope

$$m_m = \left[\frac{1}{N-2} \sum_{i=1}^{N-1} \left(\frac{\Delta z_i}{\Delta x_i} \right)^2 \right]^{1/2} \tag{5.2.2}$$

In Eqs. (5.2.1) and (5.2.2) subscripts m indicate that the surface roughness parameters were evaluated from mechanically acquired measurements. N represents the number of profile data points. Δz_i is the distance perpendicular to the mean surface plane between two profile points, and Δx_i is the distance parallel to the mean surface plane between the corresponding profile points. Results of the calculations are presented in Table 5.1. In general, rms height and rms slope are ordered according to the abrasive size used for surface preparation. The exceptions could possibly be due to surface preparation technique. Newness of the abrasive, pressure on the sample, speed of polishing wheel, amount of lubricant, and length of time determine the roughness attained by the sample. These affects are not expected to influence the conclusions derived from this research since the surface characteristics are specified. Samples of identical substrate material are numbered according to increasing rms height. The S-8 sample possesses the largest rms height but the smallest rms slope of the stainless steel samples. These characteristics are also displayed by SEM photographs shown in Fig. 5.1 for this sample. Except for the S-8 sample, rms slopes are nearly proportional to rms height with the proportionality constant equal to approximately 1/4.

Further quantitative specification of the surface roughness profiles was determined by calculation of roughness height probability density

function and autocorrelation function [29,70]. The difference between the minimum and maximum values of roughness height for each sample was divided into 45 equal height intervals [70] for calculation of probability density function. Representative results of this analysis are presented in Fig. 5.3. The graphs to the left in this figure display the normalized roughness height probability density function, $p(z)\ \sigma_m\sqrt{2\pi}$ as a function of normalized roughness height z/σ_m. The graphs to the right represent the autocorrelation function $C(\tau)$ as a function of correlation distance τ. Also shown on the respective graphs are results for a Gaussian roughness height probability density function described by the expression

$$p(z) = \frac{1}{\sigma_m\sqrt{2\pi}} \exp\left[-z^2/(2\sigma_m^2)\right] \tag{5.2.3}$$

and the Gaussian autocorrelation function given by the relation

$$C(\tau) = \exp\left[-(\tau/a_m)^2\right] \tag{5.2.4}$$

where a_m is correlation length. Correlation length was taken as the value of correlation distance where the autocorrelation function for the profile measurements attained a value of e^{-1} [29]. It appears that the statistical properties of the rough surface are adequately described by Gaussian distributions.

As the profilometer traverses the rough surface, a scratch develops due to the finite weight (100 mg) required for the stylus to maintain contact with the surface. SEM photographs of the scratches on the A-9 and S-3 samples are shown in Fig. 5.4. Two scratches are shown for the A-9 sample, and two photographs of different magnifications are shown for a scratch on the S-3 sample. Observe that for the aluminum alloy sample, the stylus plows through the surface irregularities

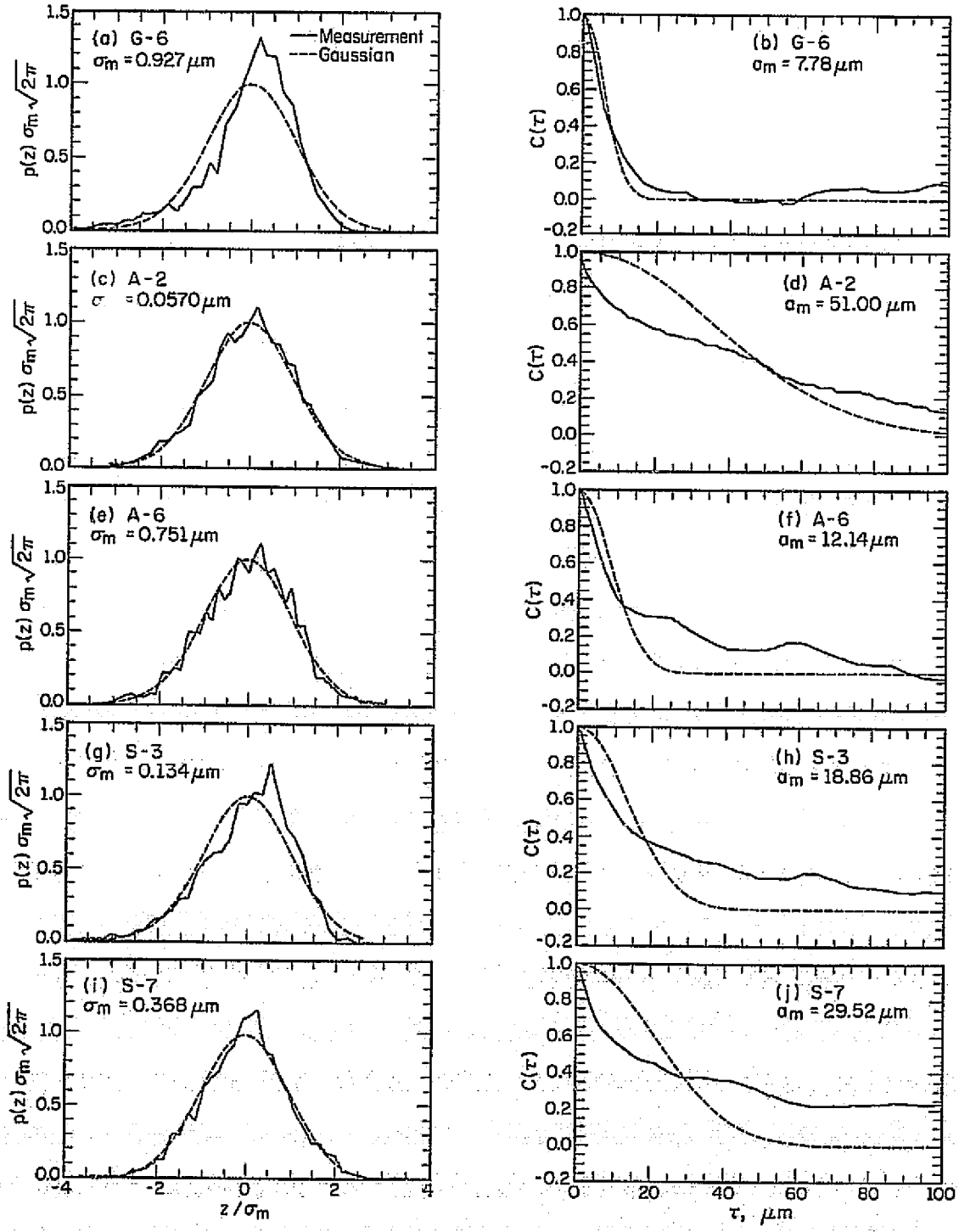

Figure 5.3 Roughness Height Probability Density Function and Autocorrelation Function

A-9 145 X Magnification

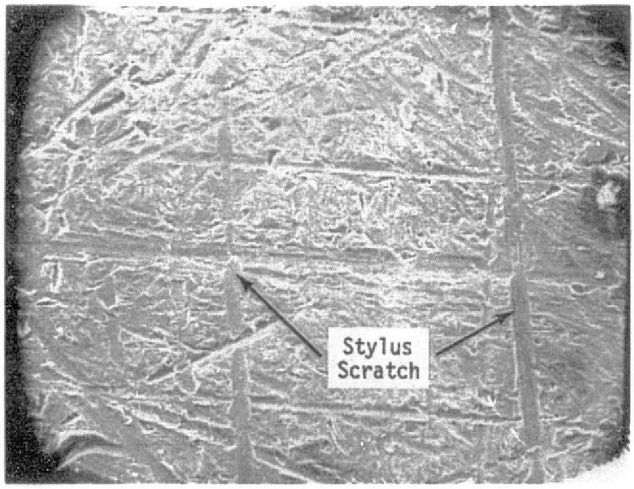

(a)

650 X Magnification

S-3

1300 X Magnification

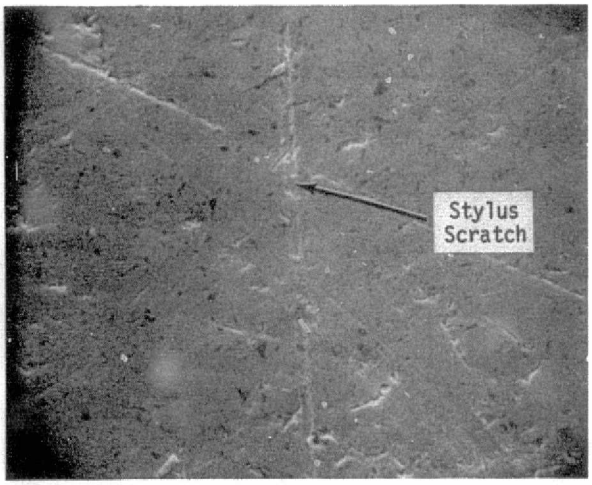

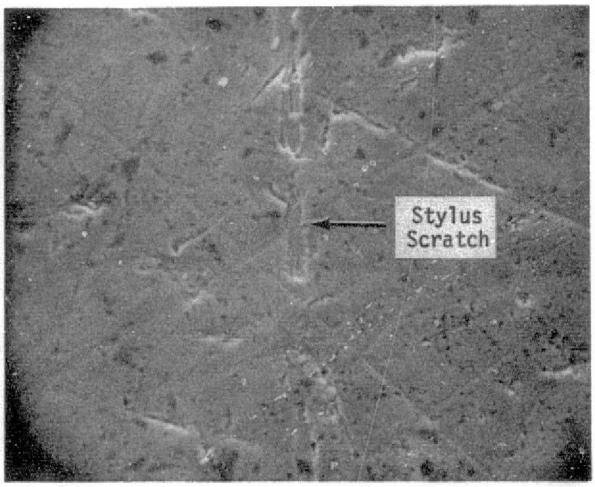

(b)

(c)

Figure 5.4 SEM Photographs of Profilometer Stylus Scratches

instead of following them whereas, for the stainless steel sample, the stylus fails to maintain contact with the surface. Further investigation is necessary to ascertain the influence of these observations on the surface profile information obtained, the resultant surface roughness parameters determined therefrom, and reflectance measurements.

6. REFLECTANCE MEASUREMENTS

Presentation of reflectance measurements is subdivided into three sections. SPR and BDR measurements are reported in Sections 6.1 and 6.2, respectively. In Section 6.3, directional reflectance measurements are discussed. For all reflectance measurements, test samples were oriented such that azimuthal angle of incidence has a value of 180 degrees and, therefore, azimuthal angle of reflection attains values of 0 and 180 degrees.

6.1 SPR MEASUREMENTS

SPR measurements for smooth and rough surfaces are reported in Sections 6.1.1 and 6.1.2, respectively. Measurements for smooth samples are necessary to calculate SPR and BDR values for the rough surfaces and, also, are intended to further demonstrate the accuracy of the BDR facility described in Chapter 3.

6.1.1 Smooth Surfaces

SPR measurements for glass, aluminum alloy, and stainless steel smooth samples were acquired, and average values for the three samples are displayed in Fig. 6.1 as a function of wavelength of incident energy for polar angles of incidence equal to 10, 30, 60, and 80 degrees. Individual sample measurements deviated from these average values by less than 1 percent with the maximum occurring at a wavelength of 1 μm. In comparison to SPR measurements for polar angle of incidence equal to 5 degrees as reported by Bennett [66] for aged aluminum film, SPR measurements for polar angle of incidence equal to 10 degrees presented in Fig. 6.1 differ by less than 1 percent for wavelengths longer than 2 μm and less than 3.3 percent

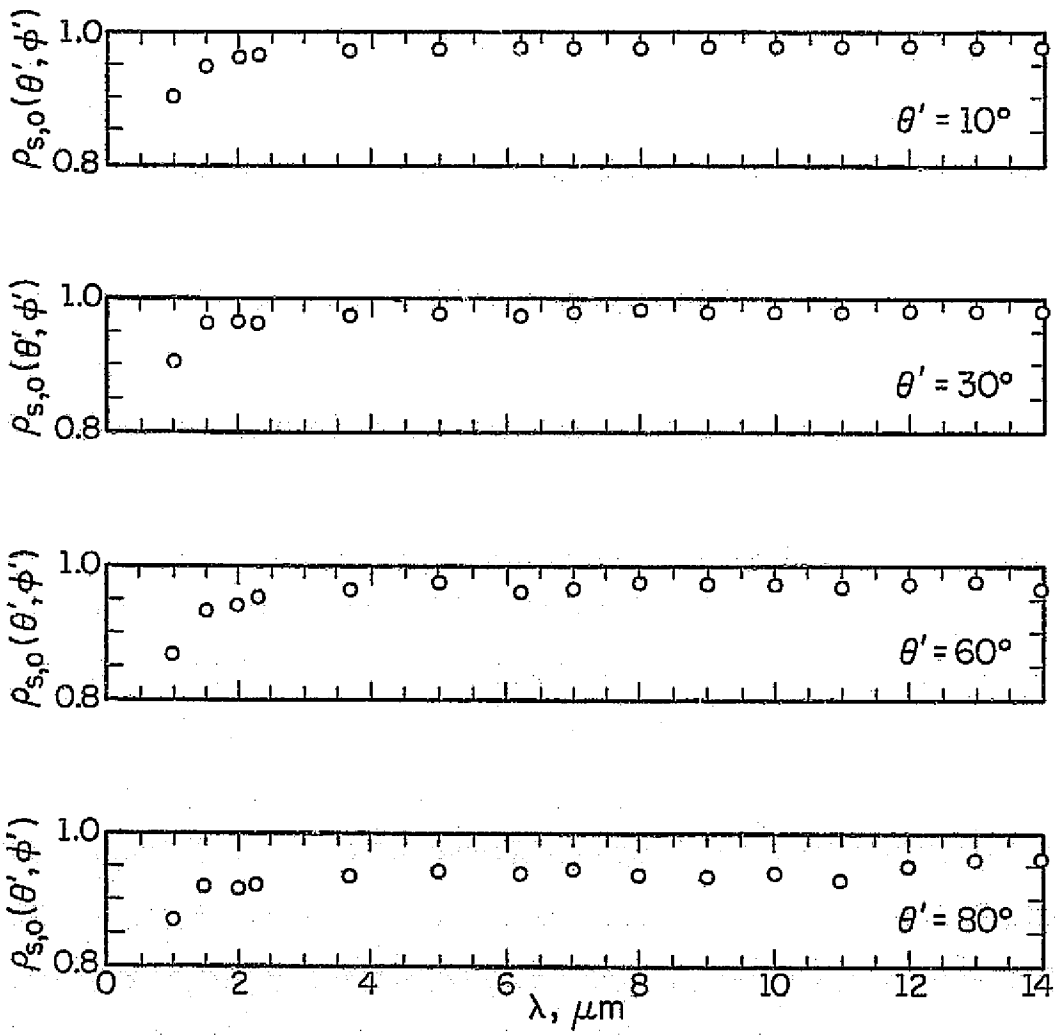

Figure 6.1 SPR Measurements for Smooth Samples

for shorter wavelengths. The difference at shorter wavelengths may be attributed to substrate surface preparation and evaporation conditions which are known to strongly influence SPR at these wavelengths [66]. Further examination of measurement accuracy particularly for other than near-normal incidence was made by calculating SPR from the Fresnel equations [18] using reported optical constant values for aluminum film [65]. For wavelengths longer than 2 μm, SPR measurements were within 1 percent of the calculated values for all polar angles of incidence. The maximum difference for short wavelengths ($\lambda \leq 2.0$ μm) was 4.1 percent which occurred at a polar angle of incidence equal to 60 degrees and wavelength of 1 μm. This large difference may also be attributed to substrate preparation and evaporation conditions and, therefore, the measurements are not necessarily in error by that amount.

6.1.2 Rough Surfaces

SPR measurements for glass, aluminum alloy, and stainless steel rough samples are illustrated in Figs. 6.2, 6.3, and 6.4, respectively. Measurements are reported for wavelengths of incident energy within the spectral range of 1 to 14 μm and for polar angles of incidence equal to 10, 30, 60, and 80 degrees. The ordinates represent the ratio of SPR for a rough surface, $\rho_{s,r}(\theta',\phi')$, to the corresponding value for a smooth surface of the same substrate material, $\rho_{s,o}(\theta',\phi')$. Certain characteristic trends of rough surface SPR measurements are evident in these figures. First, SPR of the rough surface approaches that of the smooth surface as wavelength increases. This trend is primarily due to a decrease in scattering by the rough surface as confirmed by BDR measurements since directional reflectance measurements indicate

Symbol	Sample	σ_m, μm	m_m	Symbol	Sample	σ_m, μm	m_m
○	G-2	0.270	0.0834	▽	G-6	0.927	0.274
□	G-3	0.358	0.108				
△	G-4	0.374	0.133				
◇	G-5	0.837	0.142				

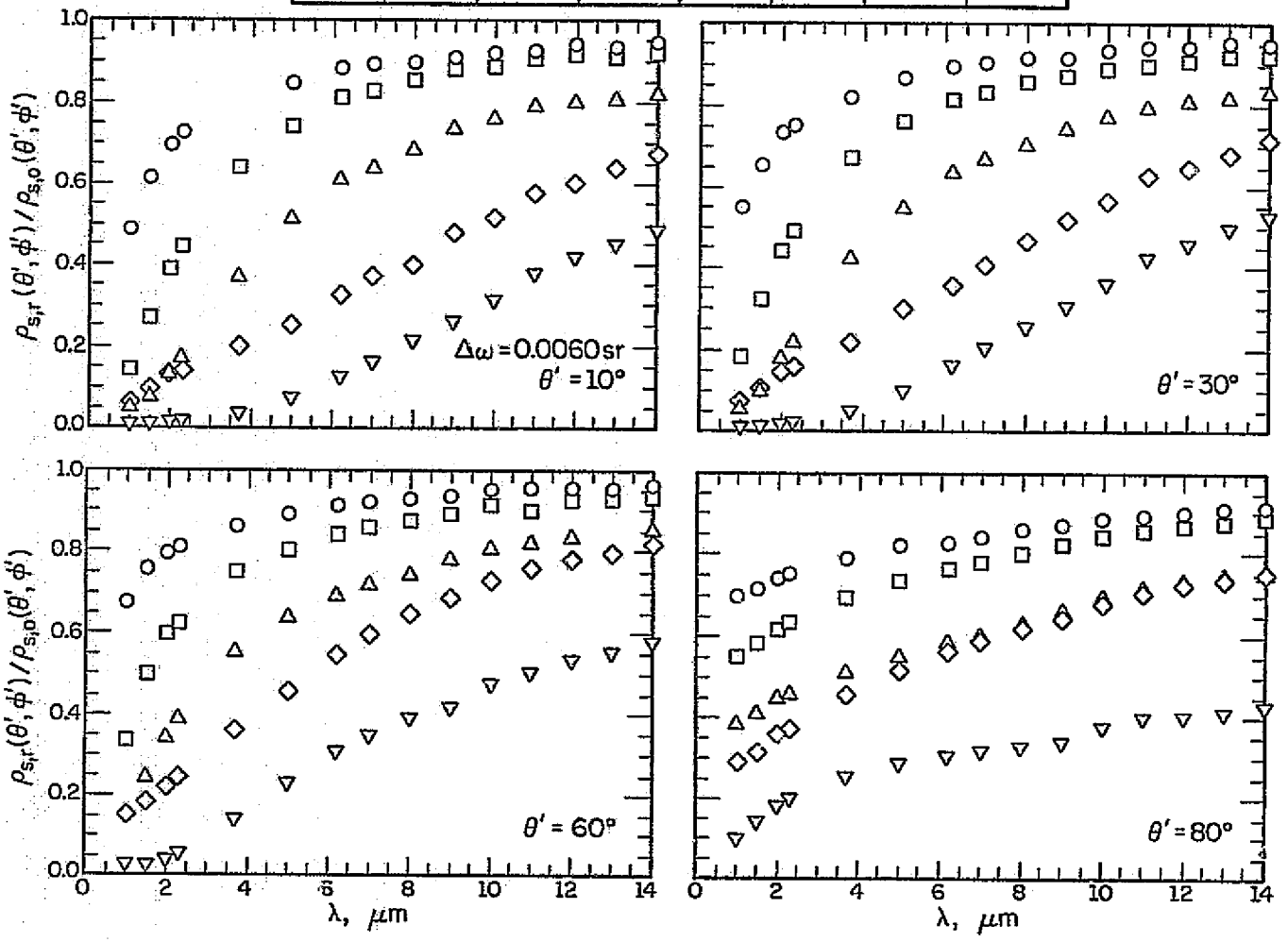

Figure 6.2 SPR Measurements for Glass Rough Samples

Symbol	Sample	$\sigma_m, \mu m$	m_m	Symbol	Sample	$\sigma_m, \mu m$	m_m
○	A-2	0.0570	0.0238	▽	A-6	0.751	0.190
□	A-3	0.145	0.0443	◊	A-7	0.794	0.156
△	A-4	0.286	0.101	◿	A-8	0.804	0.178
◇	A-5	0.314	0.104	◹	A-9	0.987	0.216

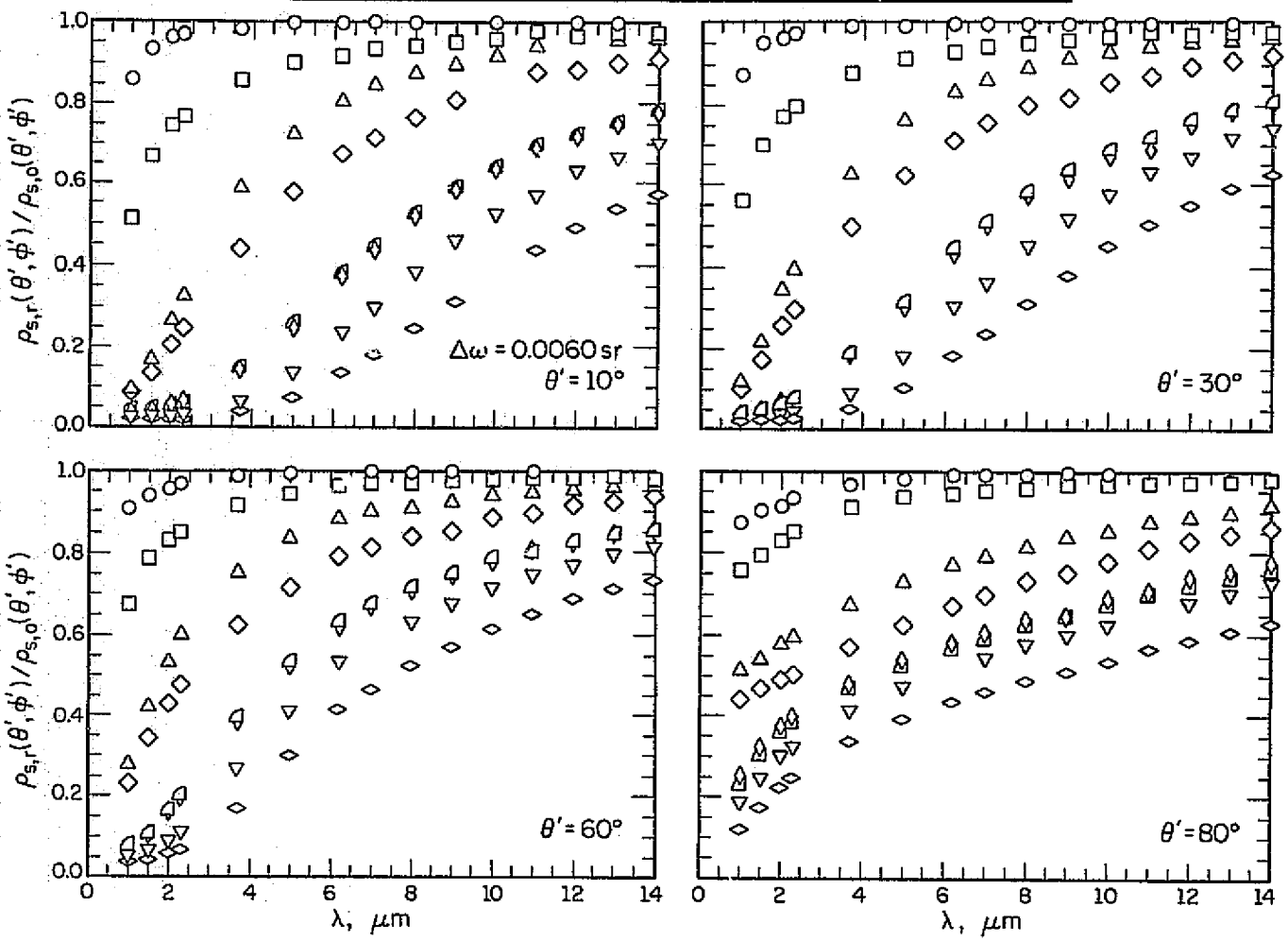

Figure 6.3 SPR Measurements for Aluminum Alloy Rough Samples

Symbol	Sample	σ_m, μm	m_m	Symbol	Sample	σ_m, μm	m_m
○	S-2	0.109	0.0410	◁	S-6	0.279	0.0798
□	S-3	0.134	0.0395	◇	S-7	0.368	0.105
△	S-4	0.240	0.0536	◊	S-8	0.496	0.0300
◇	S-5	0.251	0.0883				

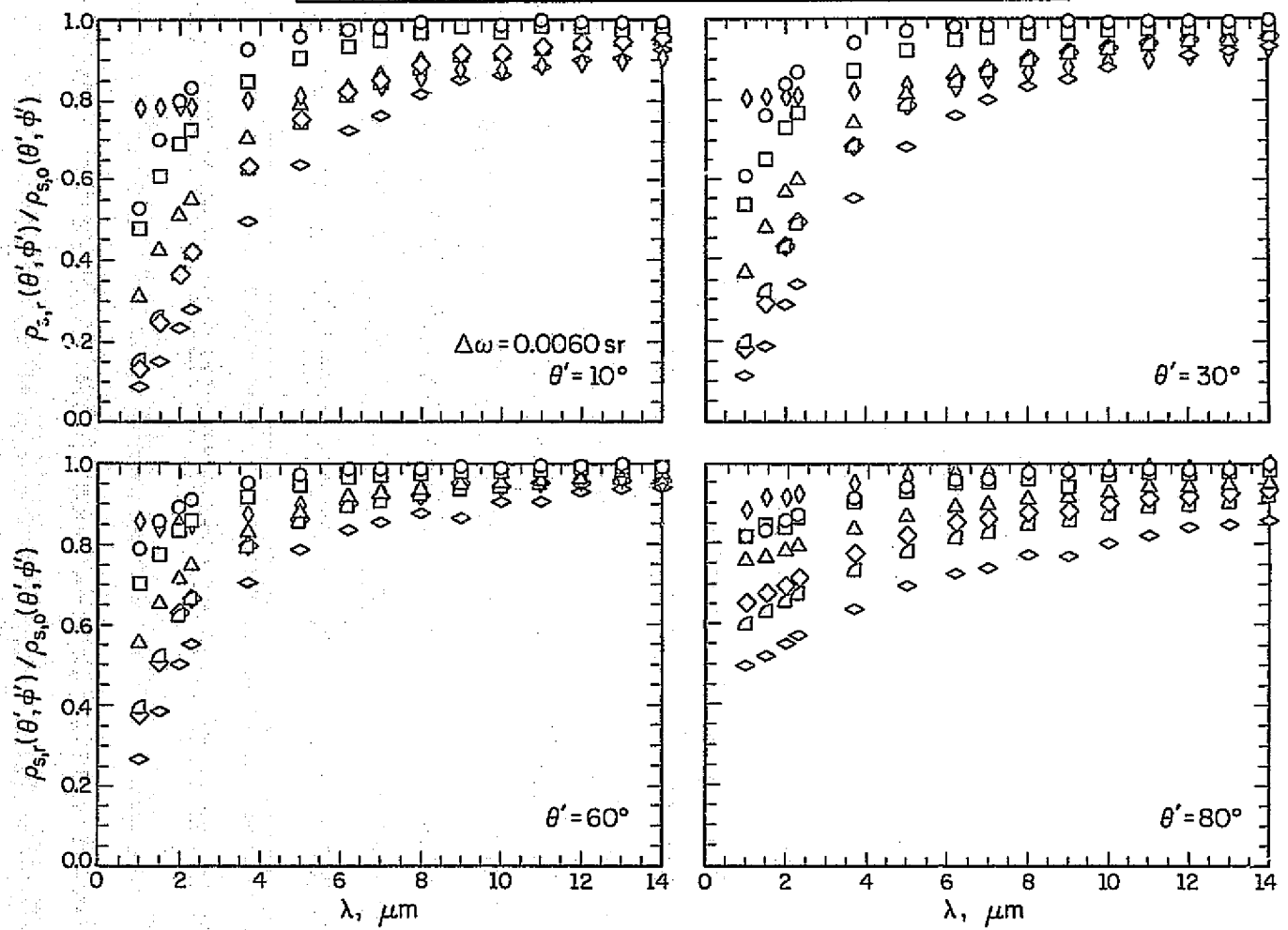

Figure 6.4 SPR Measurements for Aluminum Alloy Rough Samples

only a small increase in the magnitude of reflected energy as wavelength increases. BDR and directional reflectance measurements are presented later in this chapter. Except for a few samples, SPR decreases as roughness increases. BDR measurements illustrate an increase in scattering by the rough surface as roughness increases which results in smaller amounts of reflected energy in the specular direction and, therefore, lower SPR values. Directional reflectance measurements exhibit a small decrease with increasing roughness which is insufficient in amount to explain the decrease of SPR measurements. At long wavelengths ($\lambda \geq 10$ μm), SPR measurements for each substrate material are ordered according to the magnitude of rms height with the exception of the A-6 sample. The dependency of SPR on rms height at long wavelengths is characteristic of BDR models based on diffraction theory [32]. The behavior of SPR for short wavelengths can be explained by reference to rms slope. As displayed by the measurements, SPR decreases as rms slope increases. BDR models based on geometrical optics analysis [13] also exhibit a decrease of SPR as rms slope increases. Furthermore, these models suggest that two surfaces of identical material and equal rms slopes should have equal SPR values. rms slopes for the A-6 and A-9 samples are nearly equal and as observed in Fig. 6.3, their SPR measurements for near-normal incidence ($\theta' = 10$ degrees) are similar at short wavelengths.

The influence of surface roughness parameters on SPR can be further viewed by reference to Figs. 6.5, 6.6, and 6.7 where rough surface SPR measurements are plotted as a function of optical roughness, σ_m/λ. This ratio appears in BDR models based on diffraction theory [32] and as discussed in Chapter 2 is useful for examining surface roughness effects on BDR. As expected, SPR approaches that for a smooth surface as optical

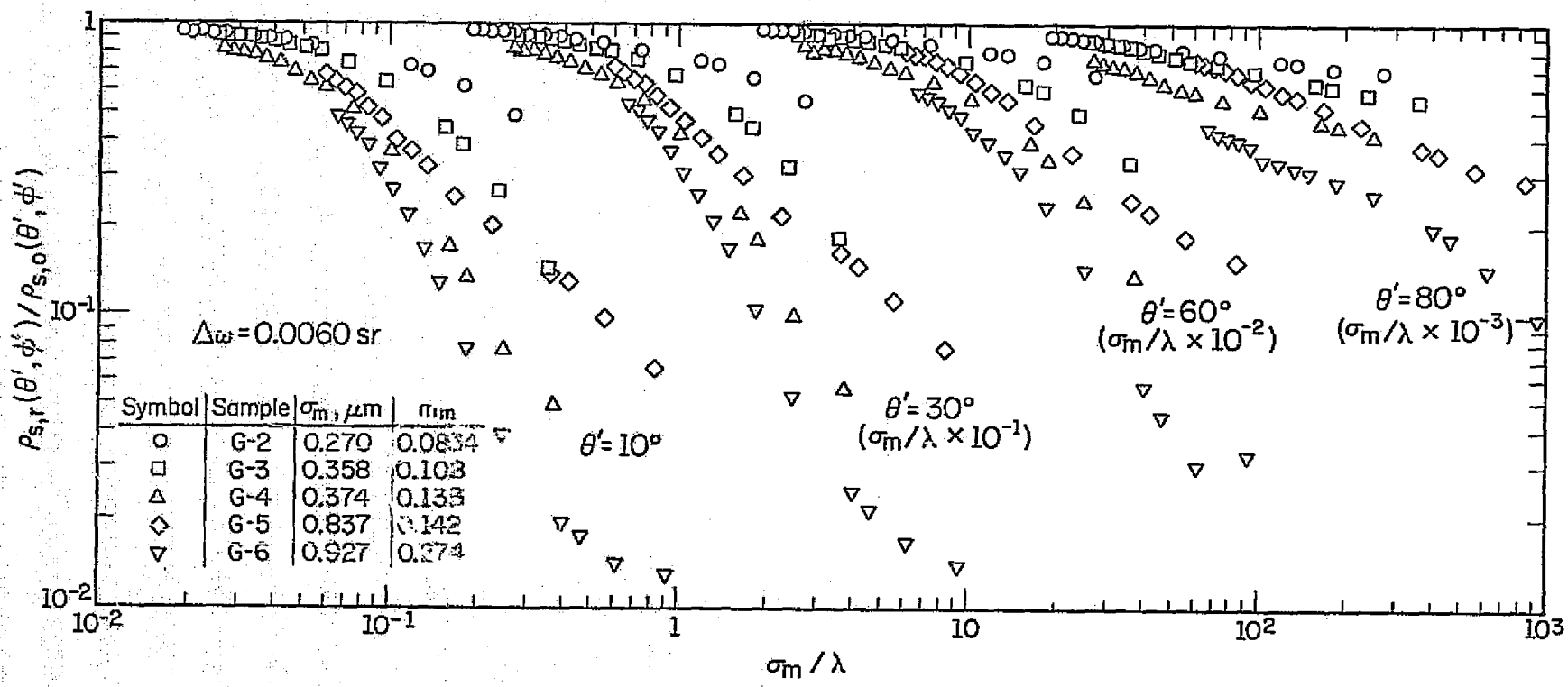

Figure 6.5 SPR Measurements for Glass Rough Samples

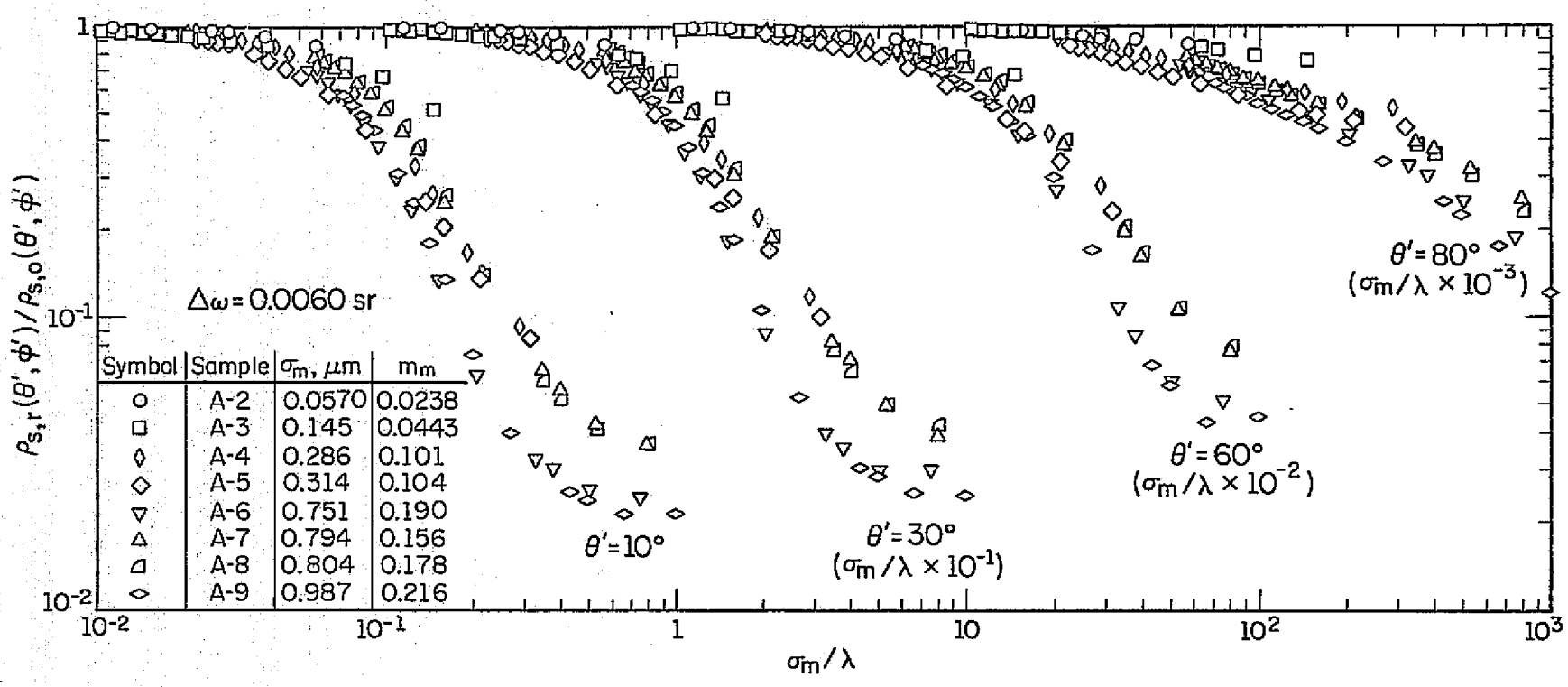

Figure 6.6 SPR Measurements for Aluminum Alloy Rough Samples

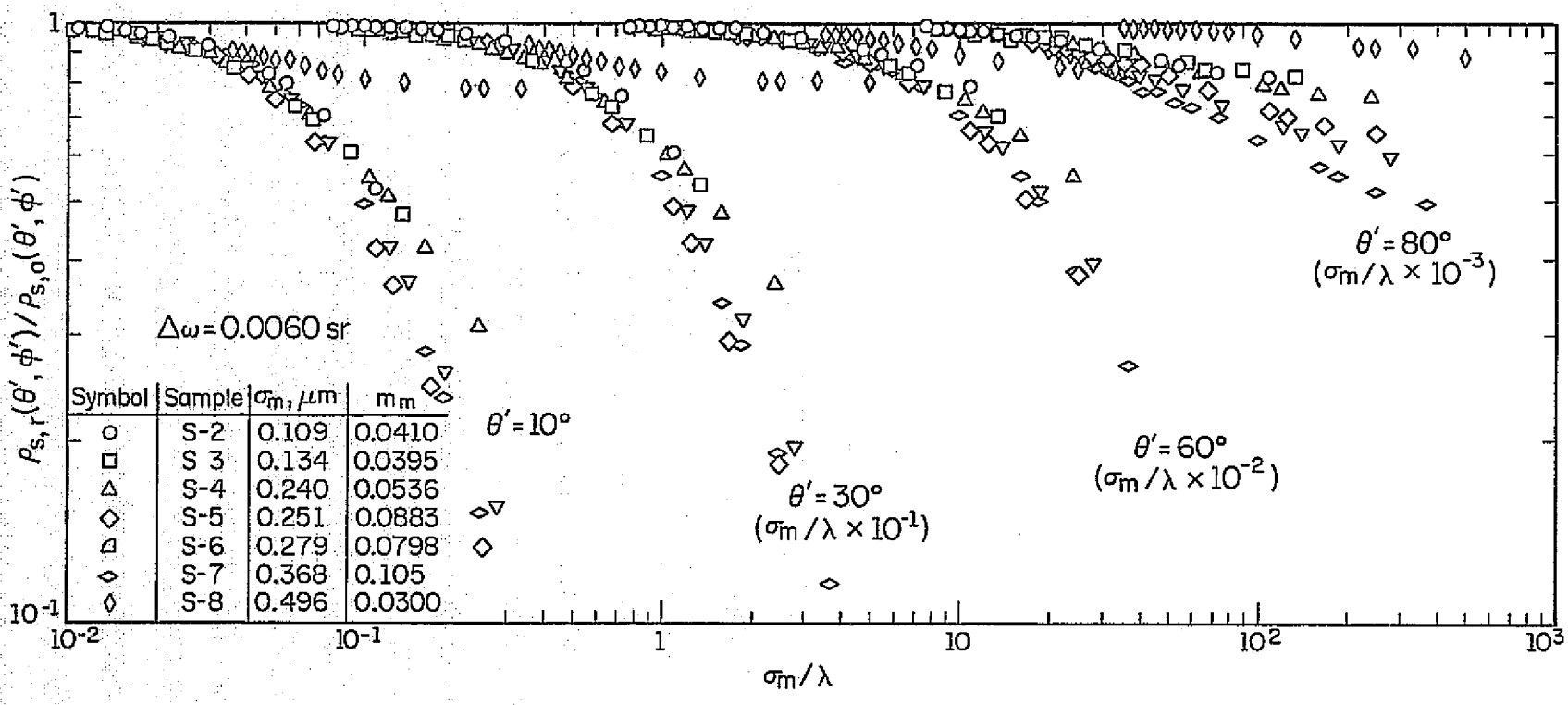

Figure 6.7 SPR Measurements for Stainless Steel Rough Surfaces

roughness diminishes. SPR measurements can be correlated with optical roughness for optical roughness values less than 0.02, but the degree of correlation depends on rms slope. As optical roughness increases, SPR measurements for each substrate material are ordered according to rms slope. This trend, however, is not fully developed in SPR measurements at polar angles of incidence of 10, 30, and 60 degrees for the G-5 sample and some of the stainless steel samples. At near-grazing incidence (θ' = 80 degrees), SPR measurements with the exception of the S-6 sample are in agreement with this trend for the largest optical roughness values shown for each sample. SPR measurements at near-normal incidence for the G-6, A-6 through A-9, and S-8 samples are relatively insensitive to optical roughness for optical roughness values greater than 0.8, 0.6, and 0.2, respectively. Geometrical optics models [13] predict an independence of SPR on optical roughness. This characteristic, however, becomes less pronounced as polar angle of incidence increases. Thus, as observed in Chapter 2, polar angle of incidence strongly influences the range of application of BDR models. As previously observed, rms slopes for the A-6 and A-9 samples are nearly identical and as displayed in Fig. 6.6, their SPR measurements coincide. This characteristic is also exhibited by the A-7 and A-8 samples and their rms slopes are nearly equal. These observations illustrate the importance of rms slope for correlating SPR measurements.

Some cited trends for SPR depend on polar angle of incidence whereas others may be examined by reference to Figs. 6.5, 6.6, and 6.7. SPR increases with increasing polar angle of incidence up to 60 degrees for all samples and continues to increase for the S-8 sample at near grazing incidence. A decrease of SPR for polar angle of incidence equal to 80

degrees is observed for the A-2 sample for all optical roughness values and for other samples (excluding the S-8 sample) only for the smallest optical roughness values. SPR for the largest optical roughness value for each sample (excluding the A-2 sample) continues to increase at near-grazing incidence. Torrance [71] reported SPR measurements that exhibited trends similar to those observed here. The increase of SPR with increasing polar angle of incidence is primarily a result of a decrease in scattering as indicated by BDR measurements. The decrease in scattering is of greater magnitude than the decrease of directional reflectance which displays a decrease even at polar angle of incidence of 60 degrees. The decrease of SPR at near-grazing incidence and small optical roughness values is attributed to the decrease of directional reflectance since BDR distributions approach specular reflection characteristics as polar angle of incidence increases.

The term $(\sigma/\lambda) \cos \theta'$ appears in diffraction BDR models [32] and suggests a means for correlating SPR measurements for various polar angles of incidence. SPR measurements for glass, aluminum alloy, and stainless steel rough samples are displayed in Figs. 6.8, 6.9, and 6.10, respectively, as a function of this parameter with σ_m as rms height. As observed in these figures, SPR measurements for polar angles of incidence equal to 10 and 30 degrees lie along a single curve when plotted against this parameter. For larger polar angles of incidence, SPR measurements, however, are not in agreement with this correlation. Typical results for polar angles of incidence equal to 60 and 80 degrees are represented in Fig. 6.8 by SPR measurements for the G-2 and G-6 samples. The agreement for these polar angles of incidence, however, improves as the value of $(\sigma_m/\lambda) \cos \theta'$ increases. The solid curves displayed in these figures

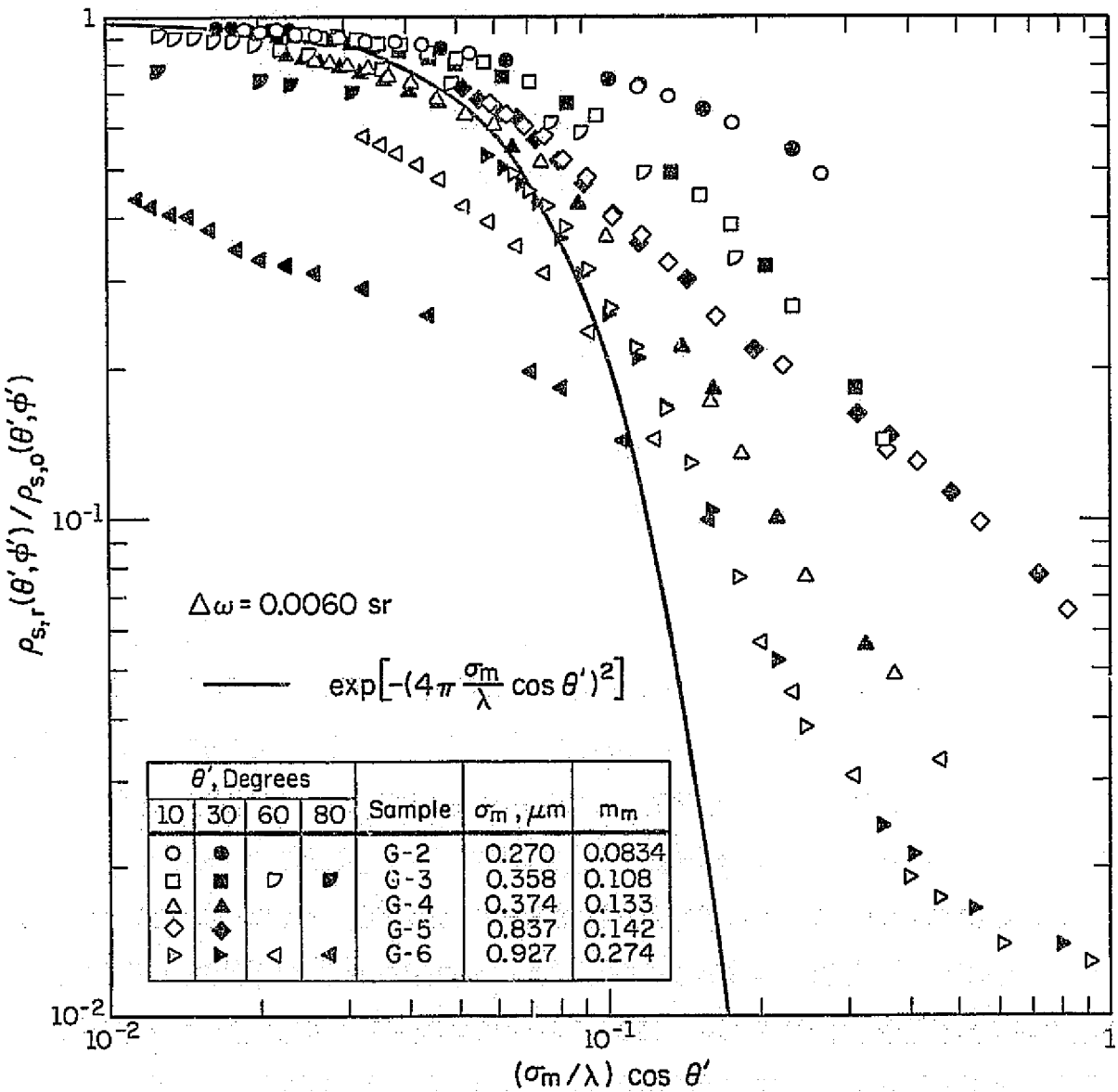

Figure 6.8 SPR Measurements for Glass Rough Samples

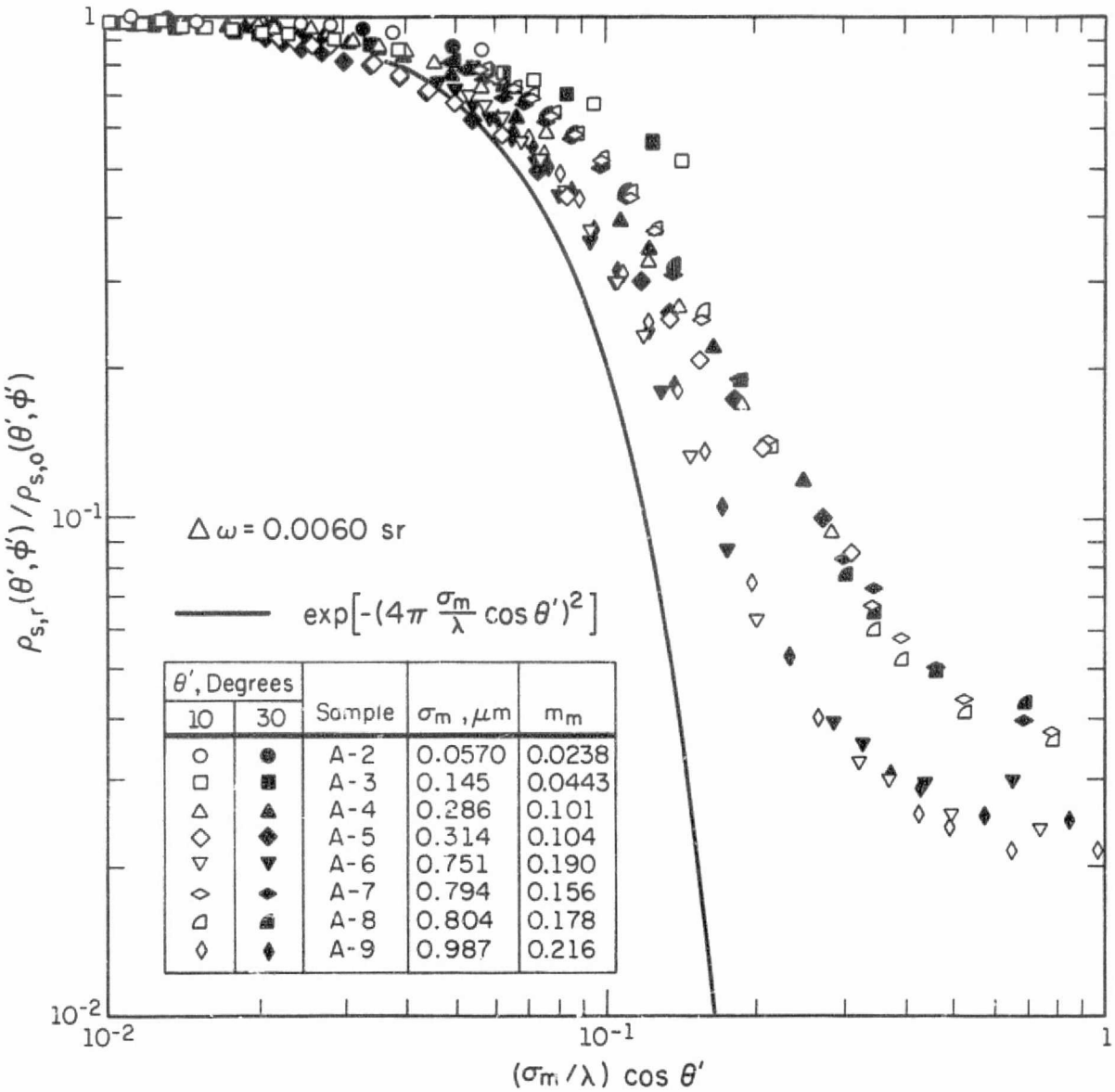

Figure 6.9 SPR Measurements for Aluminum Alloy Rough Samples

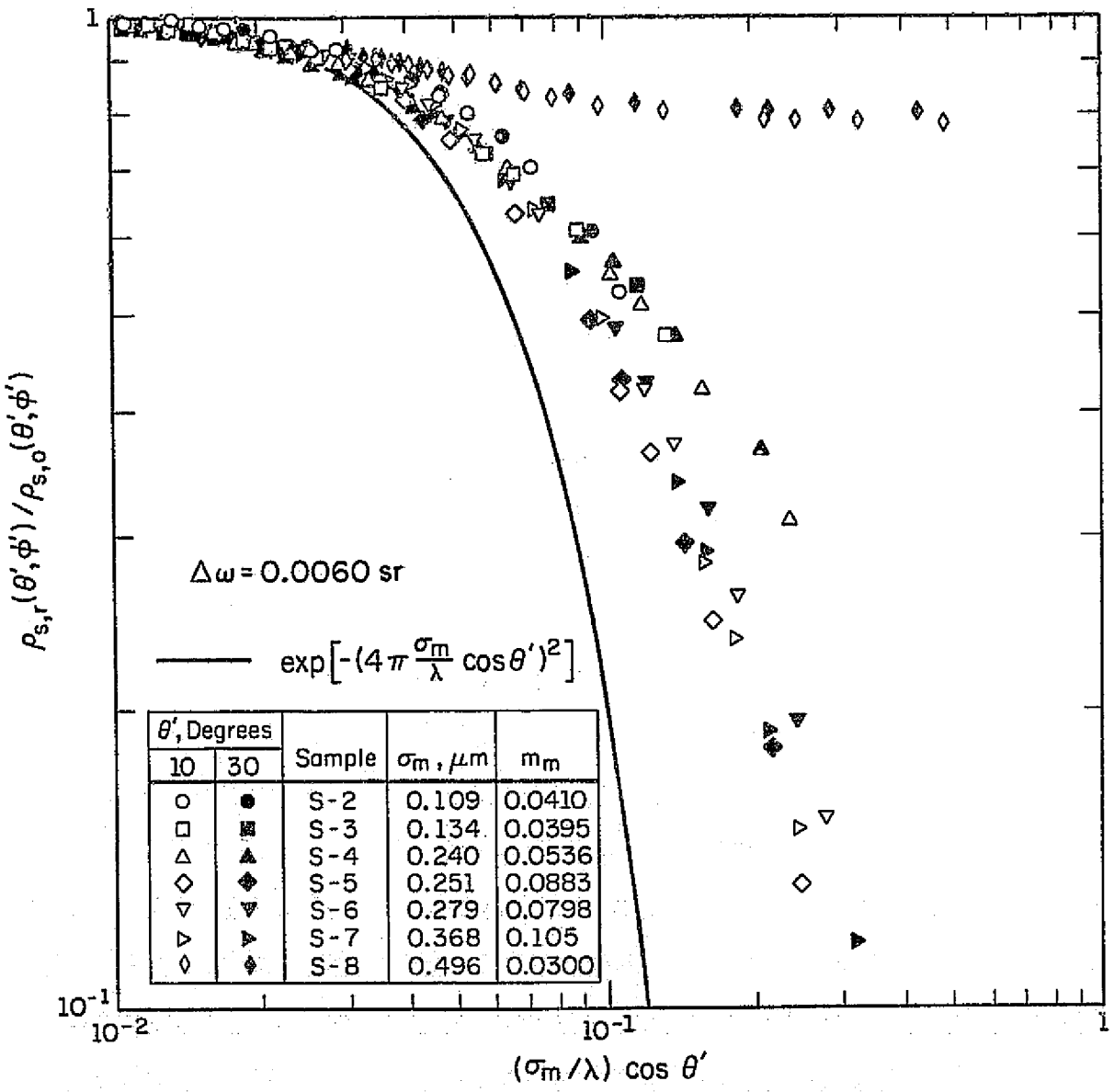

Figure 6.10 SPR Measurements for Stainless Steel Rough Samples

represent the specular component of the Beckmann BDR model, Eq. (4.2.4), with σ_m as rms height. Agreement between the specular component and SPR measurements is limited to polar angles of incidence equal to 10 and 30 degrees and strongly depends on rms slope. Adjustment of the constant 4π could improve the agreement but there is no justification for this procedure at the present.

Comparison of SPR for the three substrate materials reveals that SPR measurements at long wavelengths shown in Figs. 6.2, 6.3, and 6.4 are ordered with rms height for rms height less than 0.37. At larger rms heights, the metallic samples generally exhibit higher SPR values than the glass samples for a given rms height. For short wavelengths, the influence of rms slope becomes significant and as previously noted, some trends are not well defined. Comparison between SPR for short wavelengths can be performed by reference to Figs. 6.5, 6.6, and 6.7 where SPR is plotted as a function of optical roughness. The general trends indicate that SPR measurements are ordered with rms slope. This is particularly evident for polar angle of incidence equal to 80 degrees where SPR measurements are in sequence with rms slope. Exceptions, however, are the A-2, S-3, and S-6 samples which do not deviate significantly from this order.

6.2 BDR MEASUREMENTS

Representative plane of incidence BDR measurements for glass, aluminum alloy, and stainless steel rough samples are illustrated in Figs. 6.11, 6.12, and 6.13, respectively, for selected wavelengths and for polar angles of incidence equal to 10, 30, 60, and 80 degrees. The ordinate $\overline{R}$ is given by Eq. (3.2.13a). BDR measurements for polar angle

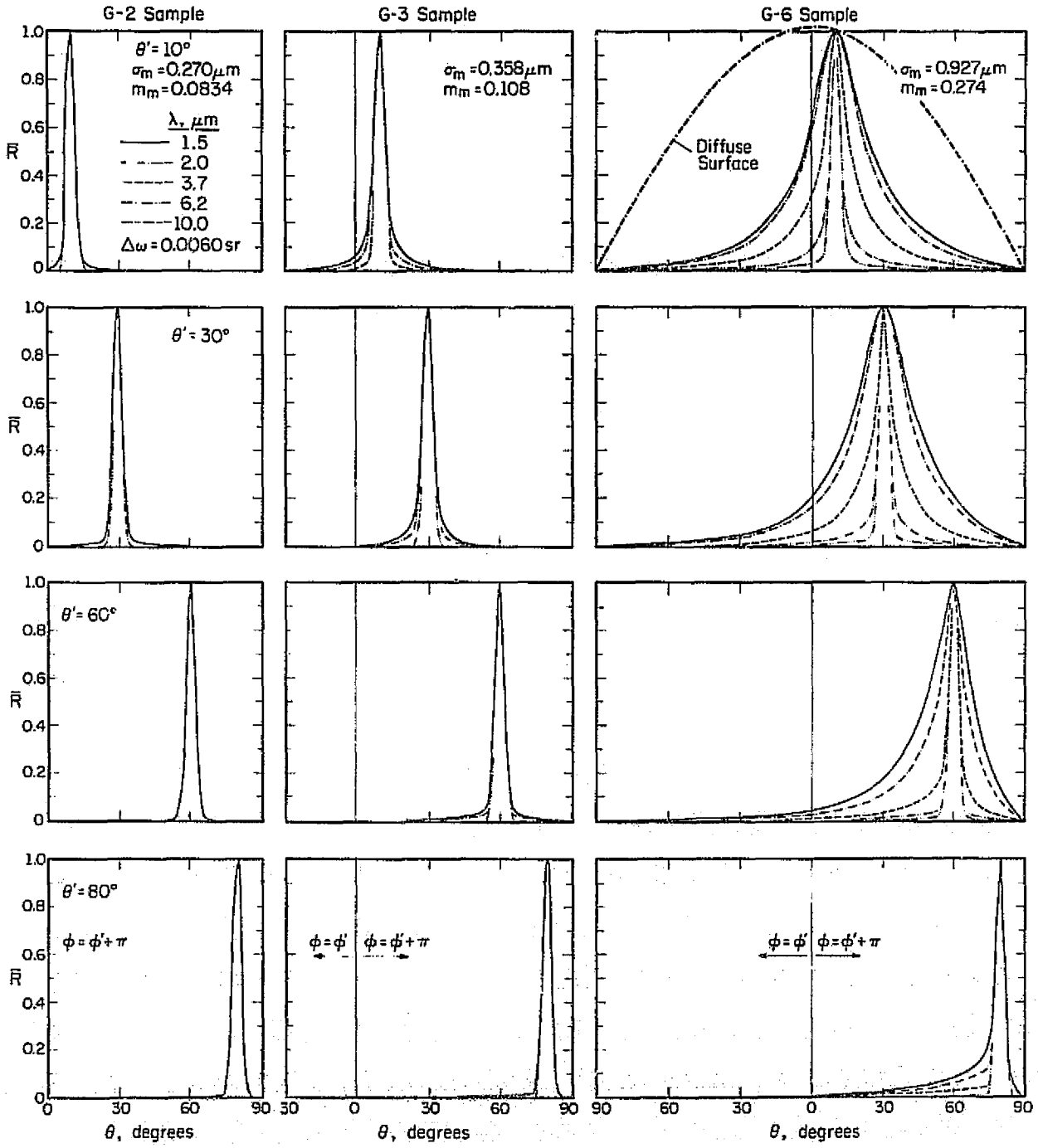

Figure 6.11 BDR Distributions for Glass Rough Samples

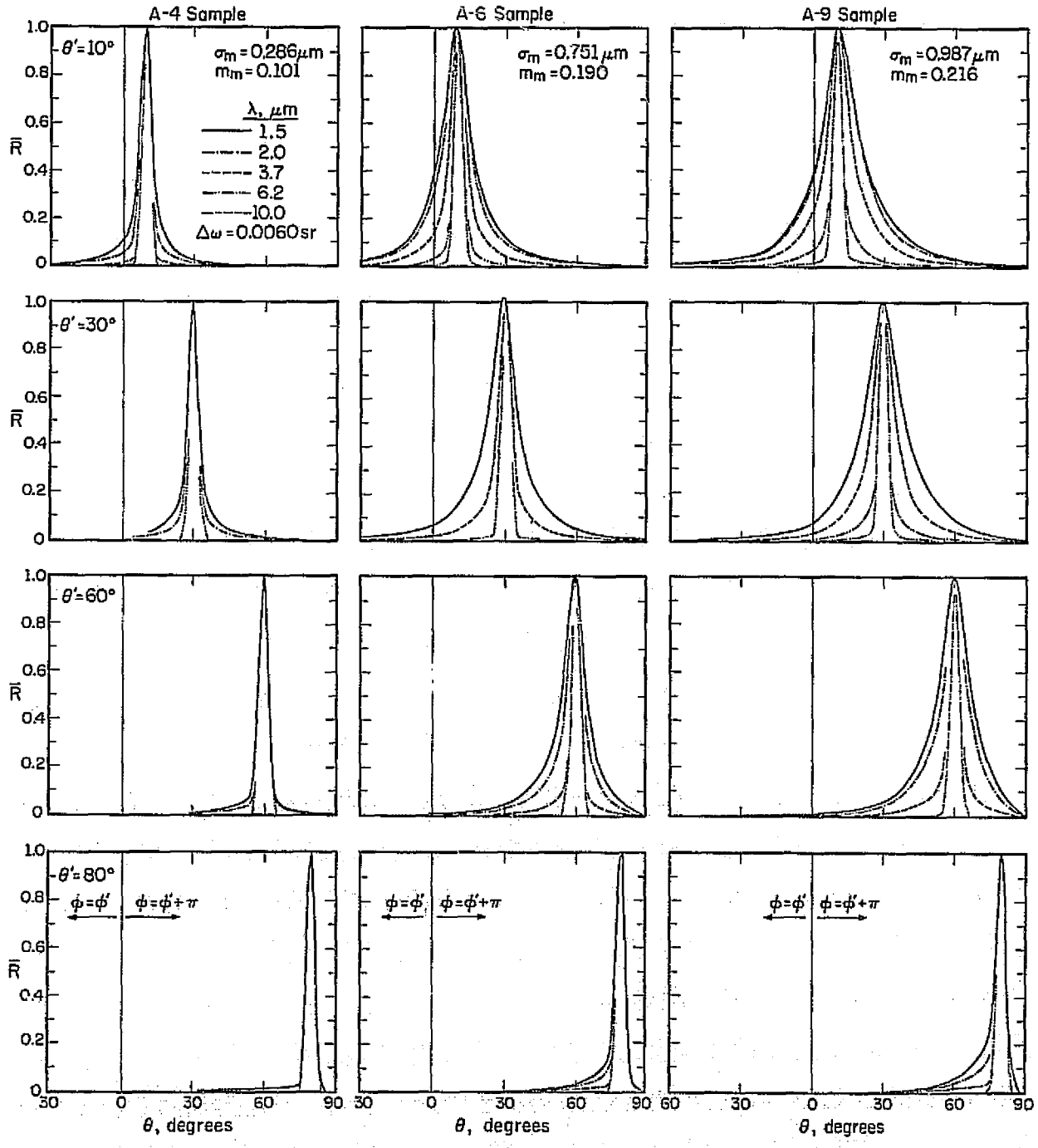

Figure 6.12 BDR Distributions for Aluminum Alloy Rough Samples

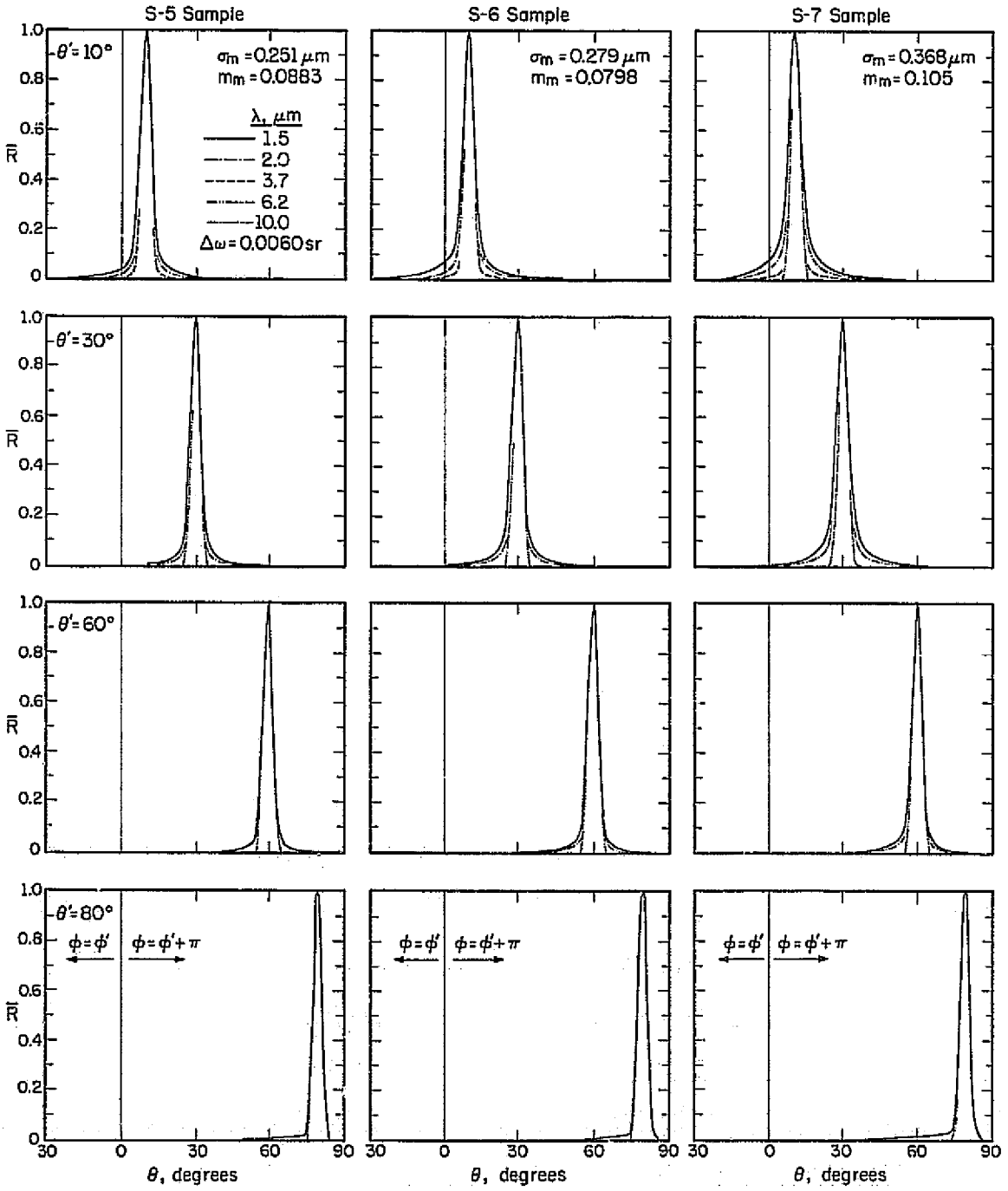

Figure 6.13 BDR Distributions for Stainless Steel Rough Samples

of incidence equal to 80 degrees were recorded using the underviewing method, Eq. (3.2.13b), and for presentation in these figures have been multiplied by the factor cos θ/cos θ'. BDR measurements were recorded at a 1 degree angular interval for polar angles of reflection within ±4 degrees of the specular direction and at a 2 degree angular interval for the remaining values of polar angle of reflection. In order to maintain clarity of the graphs, broken and solid curves are used to represent the data. Where appropriate, BDR distributions have been extrapolated for polar angles of reflection at which blockage of incident energy occurs. Absolute value of BDR can be evaluated from the following expression

$$\rho_{bd}(\theta',\phi';\theta,\phi) = \rho_{s,o}(\theta',\phi') \left[\frac{\rho_{s,r}(\theta',\phi')}{\rho_{s,o}(\theta',\phi')}\right]\left[\frac{\rho_{bd}(\theta',\phi';\theta,\phi)\cos\theta}{\rho_{bd}(\theta',\phi';\theta',\phi'+\pi)\cos\theta'}\right]\frac{1}{\cos\theta\,\Delta\omega'} \tag{6.2.1}$$

where smooth surface SPR is read from Fig. 6.1. The ratio within the first set of brackets is obtained from Figs. 6.2, 6.3, or 6.4 and that in the second set which is equivalent to $\bar{R}$ from Figs. 6.11, 6.12, or 6.13. For discussion purposes only, BDR distributions for the G-2 sample are similar to those for the A-3, S-3, and S-4 samples, the G-3 sample to the G-5 and A-5 samples, the A-6 sample to the G-4, A-7, and A-8 samples, and those for the A-2, S-2, and S-8 samples to a smooth surface.

Some general comments can be cited concerning the characteristics of illustrated BDR distributions as well as those not displayed. First, specular reflection is approached with increasing wavelength and/or as polar angle of incidence nears grazing incidence. BDR measurements displayed as shown in these figures exhibit specular reflection characteristics

for optical roughness values less than about 0.05 for near-normal incidence and 0.1 for near-grazing incidence. A smooth surface would have non-zero $\overline{R}$ values only for polar angles of reflection within a 10 degree angular interval centered about the specular direction with a value of unity at the specular direction. Secondly, as roughness increases, greater amounts of reflected energy are found at polar angles of reflection further removed from the specular direction. The G-6 sample has the largest rms slope and exhibits the greatest amount of scatter of incident energy, Fig. 6.1. Its BDR distributions for short wavelengths and for near-normal incidence, however, differ considerably from that for a diffusely reflecting surface which is represented in these figures by the factor $\cos\theta/\cos\theta'$. Thirdly, the maxima of BDR occur at the specular direction, and off-specular peaks [6] are not observed when the factor of $\cos\theta/\cos\theta'$ is removed from $\overline{R}$. The greater than unity $\overline{R}$ values for the A-6 sample at short wavelengths and polar angle of incidence equal to 30 degrees is possibly due to an angular shift caused by this sample not being seated properly in the sample holder. Finally, BDR distributions are generally in agreement with the order of SPR with a lower SPR implying greater scattering by the rough surface. In accordance with SPR measurements for the G-4 and G-5 samples, BDR distributions for the G-4 sample exhibit more scattering at long wavelengths and less scattering at short wavelengths in comparison with those for the G-5 sample.

Additional comments can be made for BDR distributions which exhibit trends that differ somewhat from those previously cited. BDR distributions for the A-4 sample indicate that this sample scatters more of the incident energy than the A-5 sample at short wavelengths and for

polar angles of incidence equal to 10, 30, and 60 degrees. SPR and directional reflectance measurements are higher for the A-4 sample than for the A-5 sample. Furthermore, it was observed in Section 6.1.2 that SPR measurements for the A-7 and A-8 samples were nearly equal. BDR distributions, however, show that the A-7 sample scatters more than the A-8 sample. Directional reflectance measurements for the A-7 sample are higher than for the A-8 sample. Thus, if SPR measurements for these four samples were normalized with directional reflectance, the order of this ratio would agree more favorably with BDR distributions. This ratio could possibly be a better indication of the degree of scattering by one rough surface in comparison with that for another rough surface. This procedure was not undertaken in the present study since directional reflectance measurements for all the samples were not available. SPR measurements for the A-6 sample were observed not to agree with the rms height correlation for wavelengths longer than 2 μm. BDR distributions confirm that this sample scatters more than the other aluminum alloy samples with the exception of the A-9 sample. Directional measurements for this sample are in agreement with the sequence of SPR measurements. Based on these observations, the rms height value reported for the A-6 sample appears in error and should be intermediate to that for the A-8 and A-9 samples. The nearly wavelength independent behavior of SPR for the G-6 and A-6 through A-9 samples for short wavelengths and near-normal incidence is not exhibited by normalized BDR measurements for these samples which show a continuing increase in scattering as wavelength decreases. Since smooth surface SPR displays a noticeable decrease for short wavelengths, absolute BDR values evaluated from Eq. (6.2.1) in which smooth surface SPR appears become less sensitive to wavelength.

In Section 6.1.2 SPR characteristics were discussed by reference to surface roughness parameters rms height and rms slope as well as to optical roughness. Correlation of BDR distributions with these quanitities is examined by first observing that for a given rough surface, scattering increases as optical roughness increases. This is to be expected since the only variable as optical roughness varies for a given rough surface is wavelength. Influence of optical roughness,particularly for samples of different substrate material, is further demonstrated by selecting samples with nearly identical slopes and then comparing BDR distributions for different optical roughness values. According to diffraction BDR models [32], increased scattering should be observed as optical roughness increases. Since rms slopes varied for each sample, an rms slope interval was selected and BDR distributions for surfaces with rms slopes within this interval were examined. The interval size must be selected so that the influence of rms slope is not observed. The G-3, A-4, A-5, and S-7 samples exhibit nearly equal rms slopes, 0.108, 0.101, 0.104, and 0.105, respectively. BDR distributions for these samples are shown in Fig. 6.14 for near-normal incidence. Results for other polar angles of incidence are similar. The variable between the curves in this figure is optical roughness. With the exception of the A-4 sample, BDR distributions exhibit an increase scattering as optical roughness increases. Thus, for prescribed rms slope, scattering increases with increasing optical roughness. The applicability of this conclusion to BDR distributions for optical roughness values greater than 0.25 remains to be evaluated.

Diffraction BDR models also suggest that for a prescribed optical roughness value scattering increases as rms slope increases. Since very few samples exhibited identical optical roughness values for BDR

Sample	σ_m/λ	m_m	Sample	σ_m/λ	m_m
A-4	0.191	0.101	A-5	0.157	0.104
S-7	0.245	0.105	S-7	0.0994	0.105
G-3	0.239	0.108	G-3	0.0968	0.108
A-4	0.143	0.101	A-4	0.0773	0.101
A-5	0.209	0.104	A-5	0.0849	0.104
S-7	0.184	0.105			
G-3	0.179	0.108			

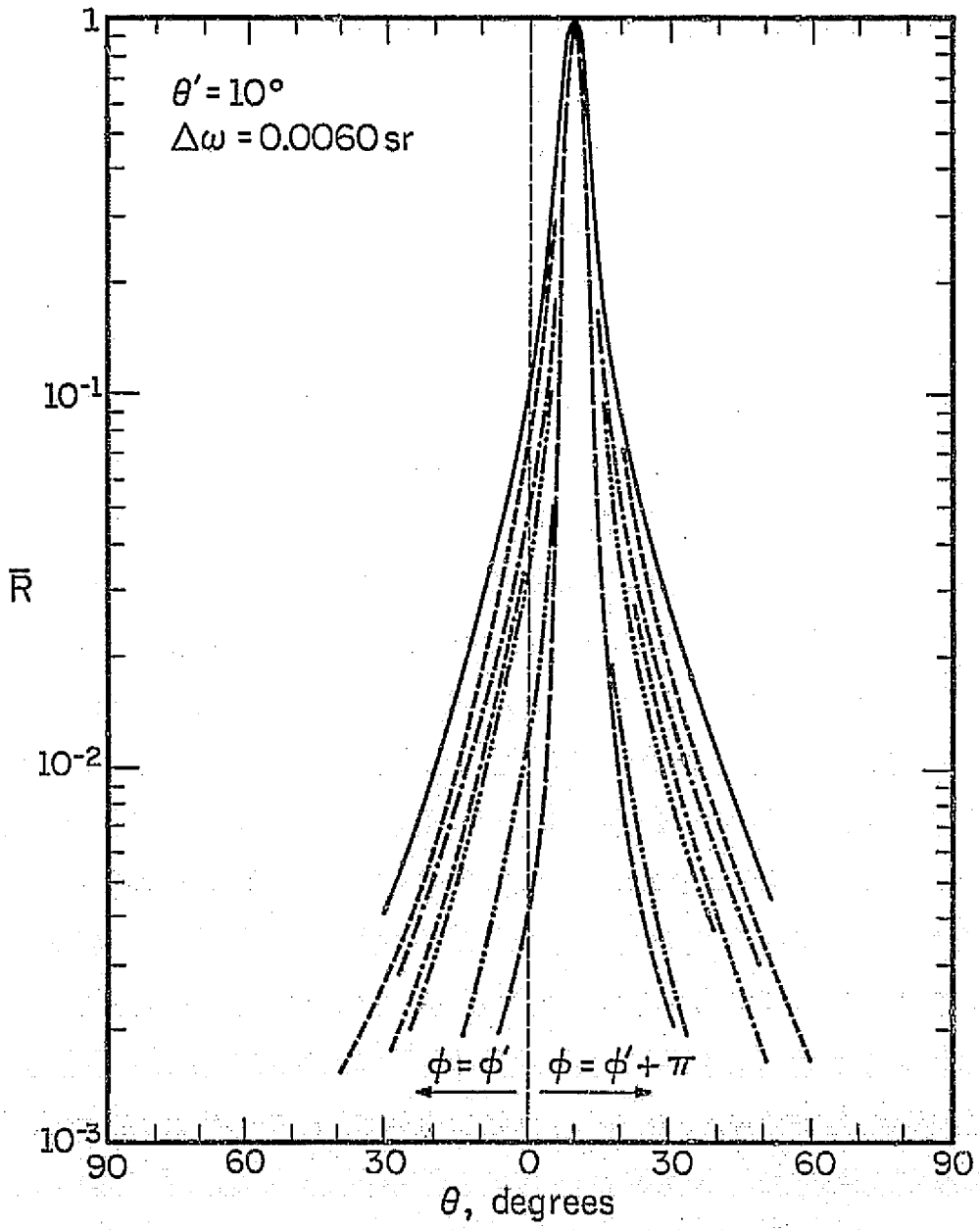

Figure 6.14 BDR Distributions for Prescribed rms Slope ($m_m \simeq 0.1$)

distributions recorded, it was necessary to select an optical roughness interval. The size of this interval was controlled by the desire of examining only the influence of rms slope. Interval sizes of approximately ±5 percent centered about optical roughness values of 0.1 as well as 0.25 and ±12 percent for optical roughness value of 0.55 were selected. BDR distributions for samples with these optical roughness values are illustrated in Figs. 6.15, 6.16, and 6.17 for near-normal incidence. The variable on the graphs is rms slope. With the exception of two optical roughness values (0.133 and 0.156 in Figs. 6.15 and 6.17, respectively), scattering increases as rms slope increases. Thus, for two surfaces with identical optical roughness values, the surface with the larger rms slope is expected to scatter more of the incident energy. These observations, as well as those discussed for SPR, establish the importance of specifying rms slope.

6.3 DIRECTIONAL REFLECTANCE MEASUREMENTS

Directional reflectance measurements were acquired with a heated cavity reflectometer similar to that described in [72]. Basically, this reflectometer consists of a cavity whose walls are heated to a temperature of approximately 750°C. Radiant energy within the cavity hemispherically irradiates a sample held by a sample holder which is located near the cavity center. A specular reference sample of platinum is attached to the sample holder and is employed to reduce errors caused by nonuniform cavity wall intensity. A viewing port allows a monochromator and detector to receive reflected energy from the sample contained within a solid angle about direction of reflection. For uniform irradiation of the sample, the ratio of detector voltage signals recorded when

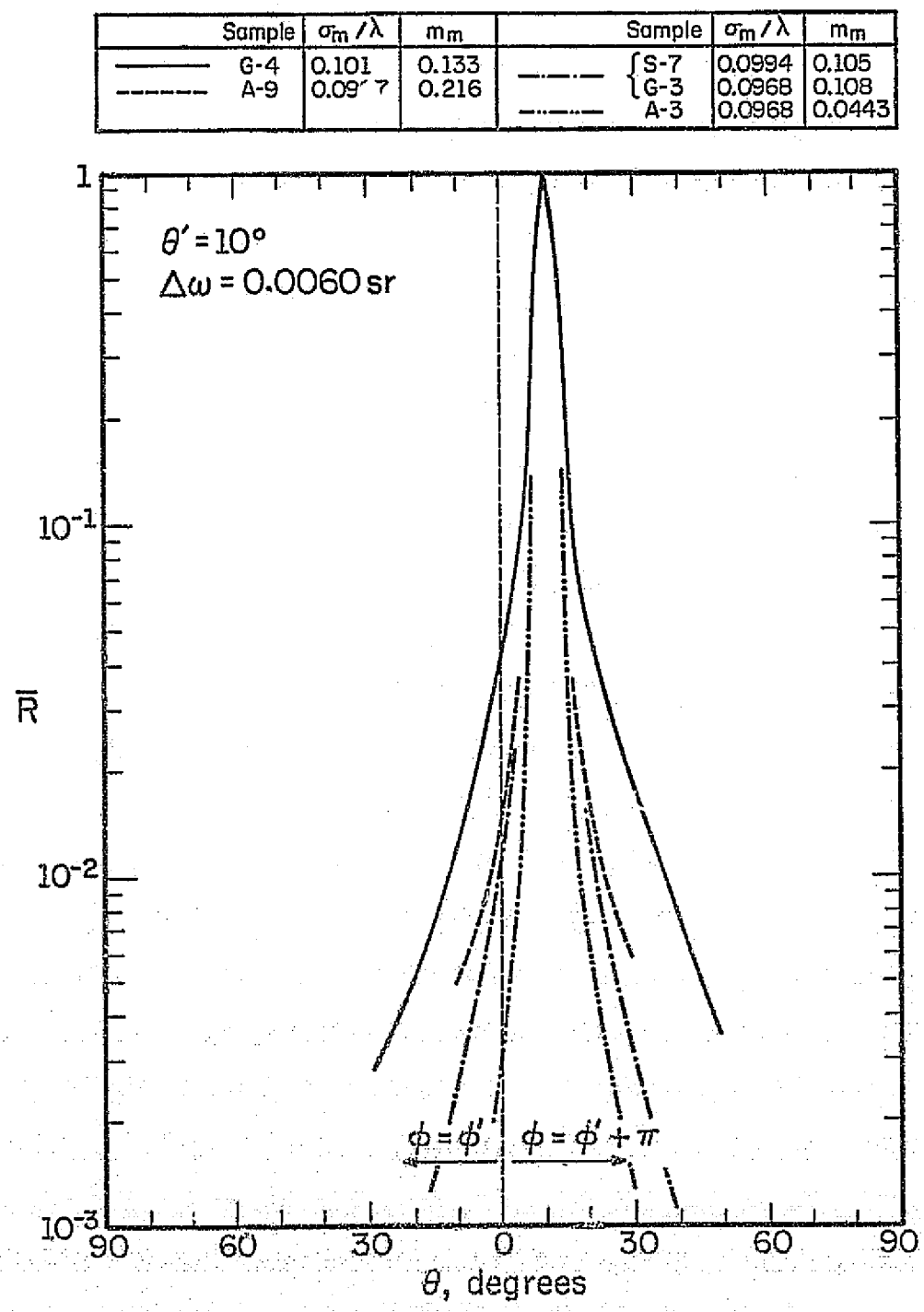

Figure 6.15 BDR Distributions for Prescribed Optical Roughness ($\sigma_m/\lambda \simeq 0.1$)

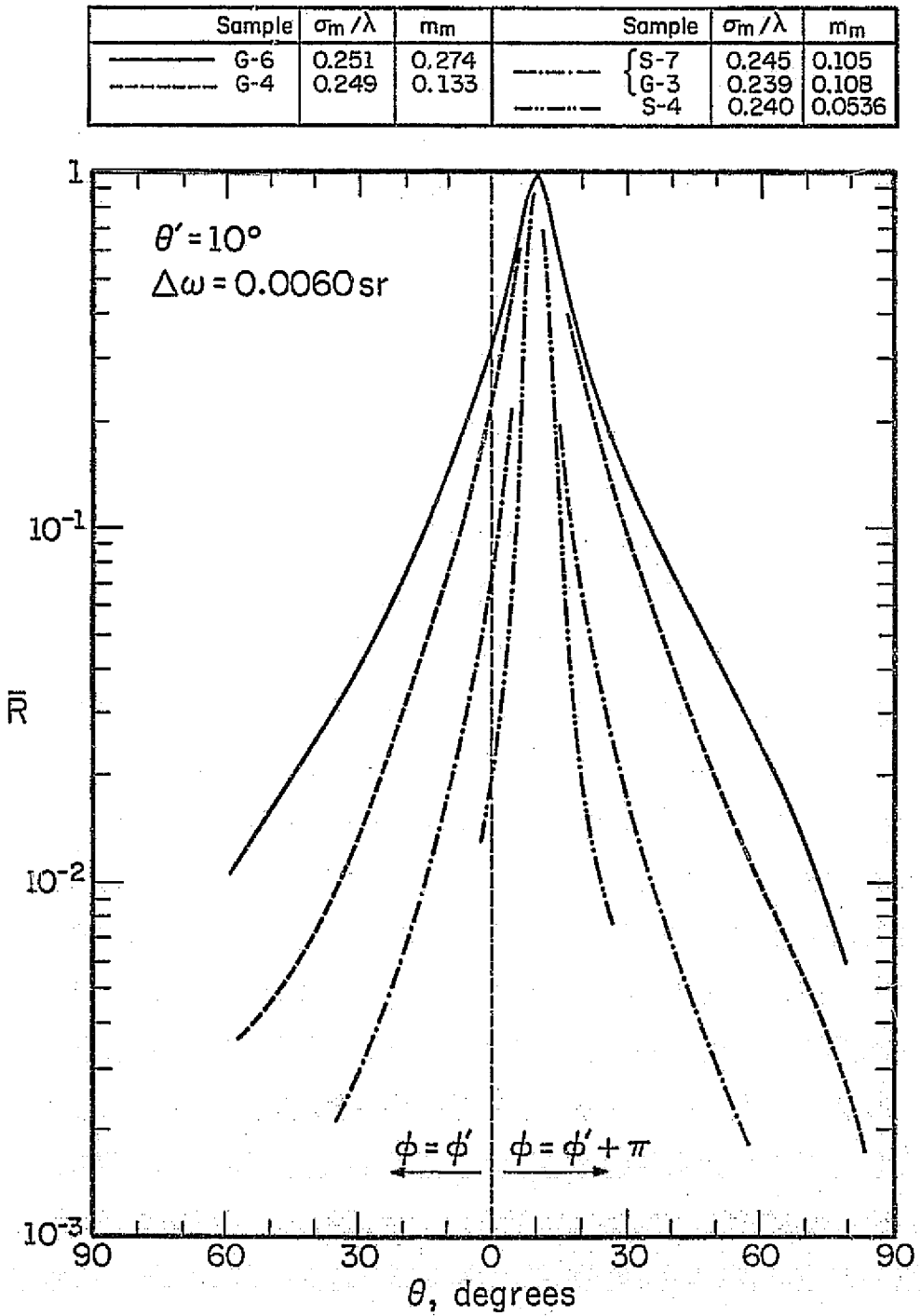

Figure 6.16 BDR Distributions for Prescribed Optical Roughness ($\sigma_m/\lambda \simeq 0.25$)

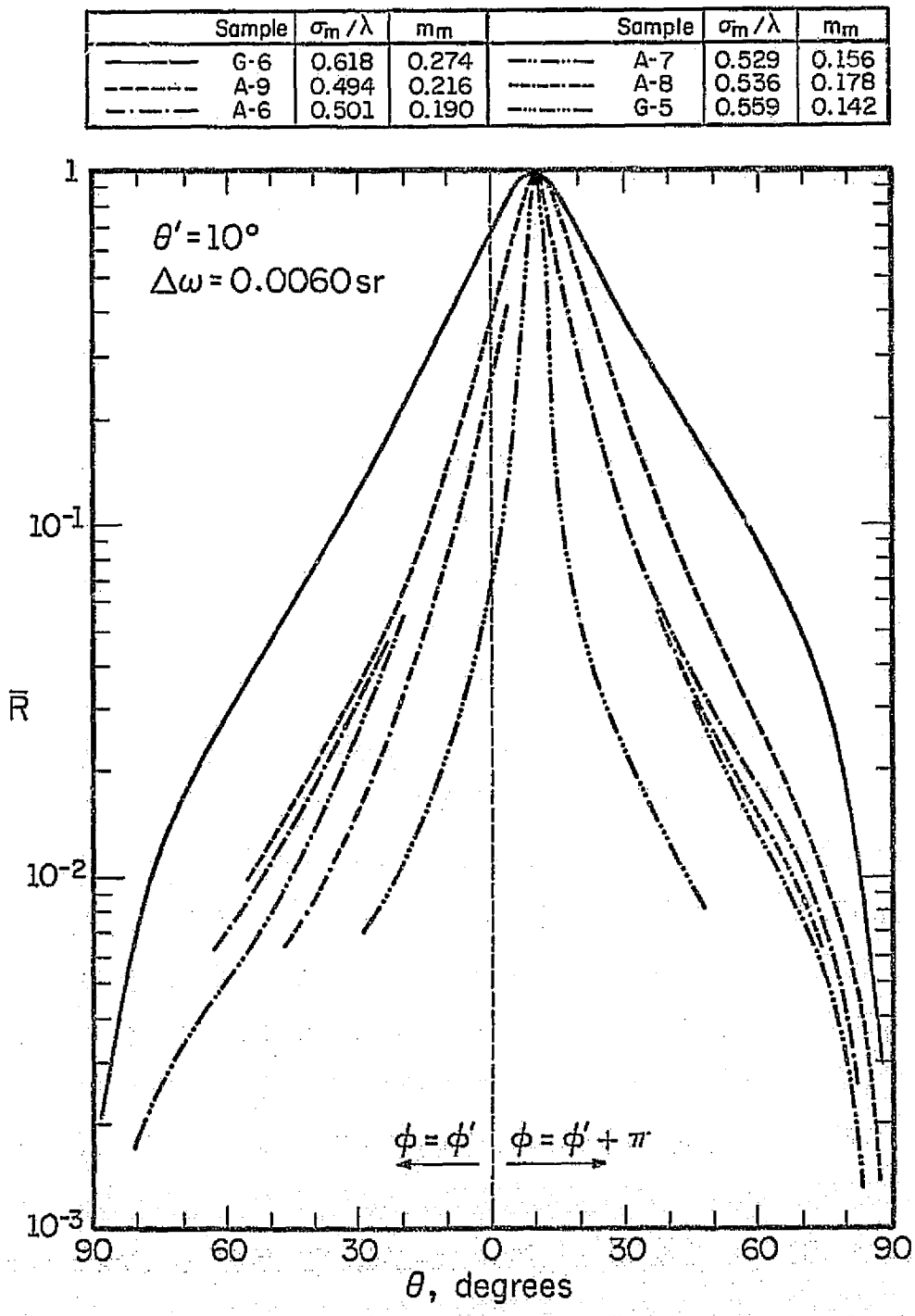

Figure 6.17 BDR Distributions for Prescribed Optical Roughness ($\sigma_m/\lambda \simeq 0.55$)

the sample and reference are viewed is hemispherical-directional reflectance. Imposing the Helmholtz reciprocity requirement for BDR, hemispherical-directional reflectance is equivalent to directional-hemispherical reflectance or,as referred to in this research,directional reflectance. The spectral range for the heated cavity reflectometer used in this research is 2.5 to 12 μm. Since finite size solid angles are necessary and due to the requirement of a viewing port, polar angles of incidence within the angular range of 20 to 60 degrees are permissible. The accuracy of the reflectometer is estimated to be ±2 or 3 percent. Since cooling of the back side of the sample is necessary to maintain the sample surface at room temperature, directional reflectance for the glass samples which might possibly break and allow water in the cavity could not be acquired with the reflectometer. However, conclusions derived from measurements for the metallic samples are expected to be applicable to the glass samples.

Directional reflectance measurements for the aluminum alloy and stainless steel samples are displayed in Figs. 6.18 and 6.19, respectively, as a function of wavelength for polar angles of incidence equal to 30 and 60 degrees. Measurements were acquired for polar angle of incidence equal to 20 degrees but, as is discussed later, are indistinguishable from those for 30 degrees. Directional reflectance for the A-2, S-1, and S-8 samples are similar to those for the A-1 sample shown in Fig. 6.18. The accuracy of the heated cavity reflectometer was examined by comparison of directional reflectance for the A-1 sample with smooth surface SPR presented in Fig. 6.1. The differences observed between these measurements are less than 1 percent with a few data points particularly at polar angle of incidence equal to 60

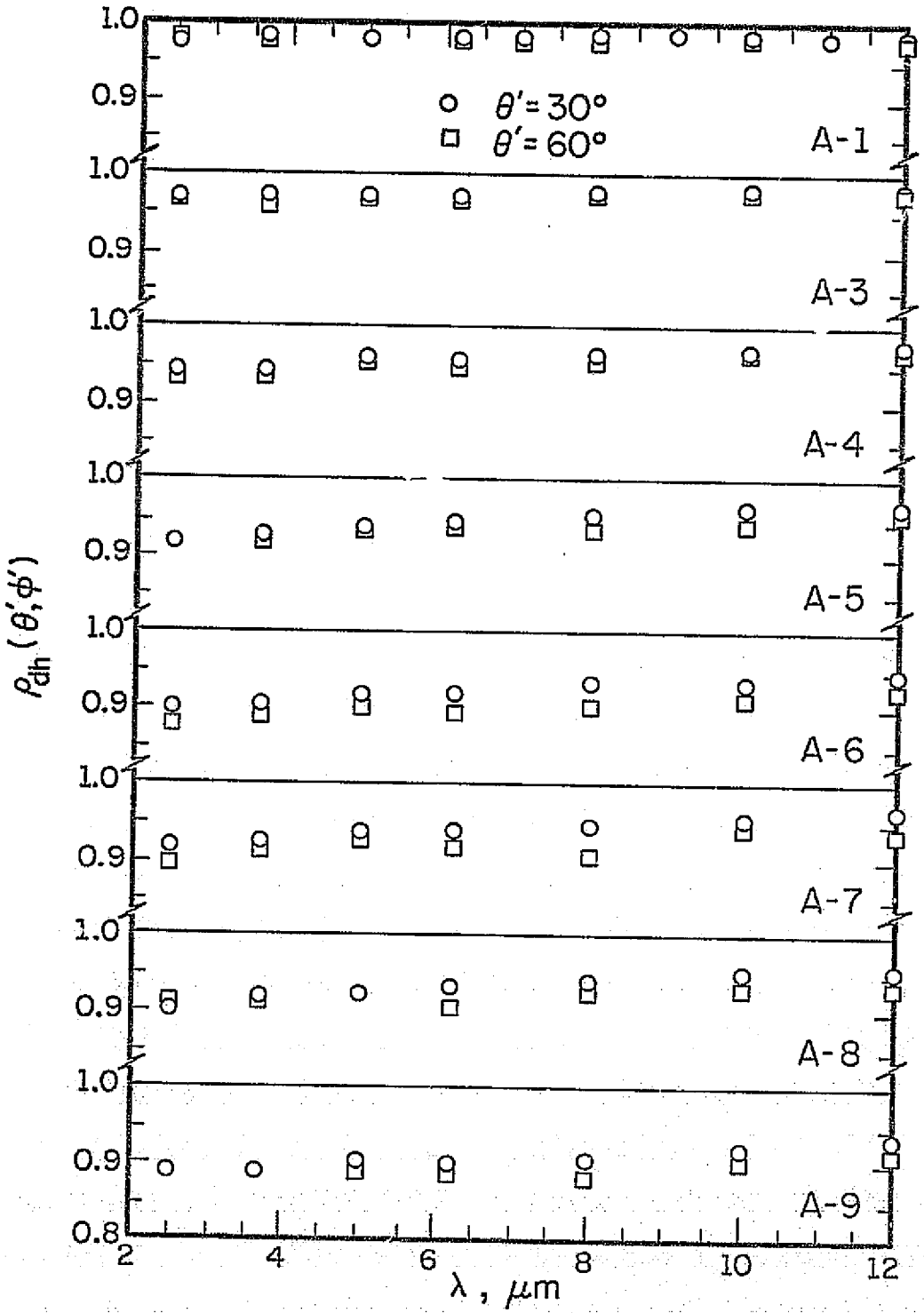

Figure 6.18 Directional Reflectance Measurements for Aluminum Alloy Rough Samples

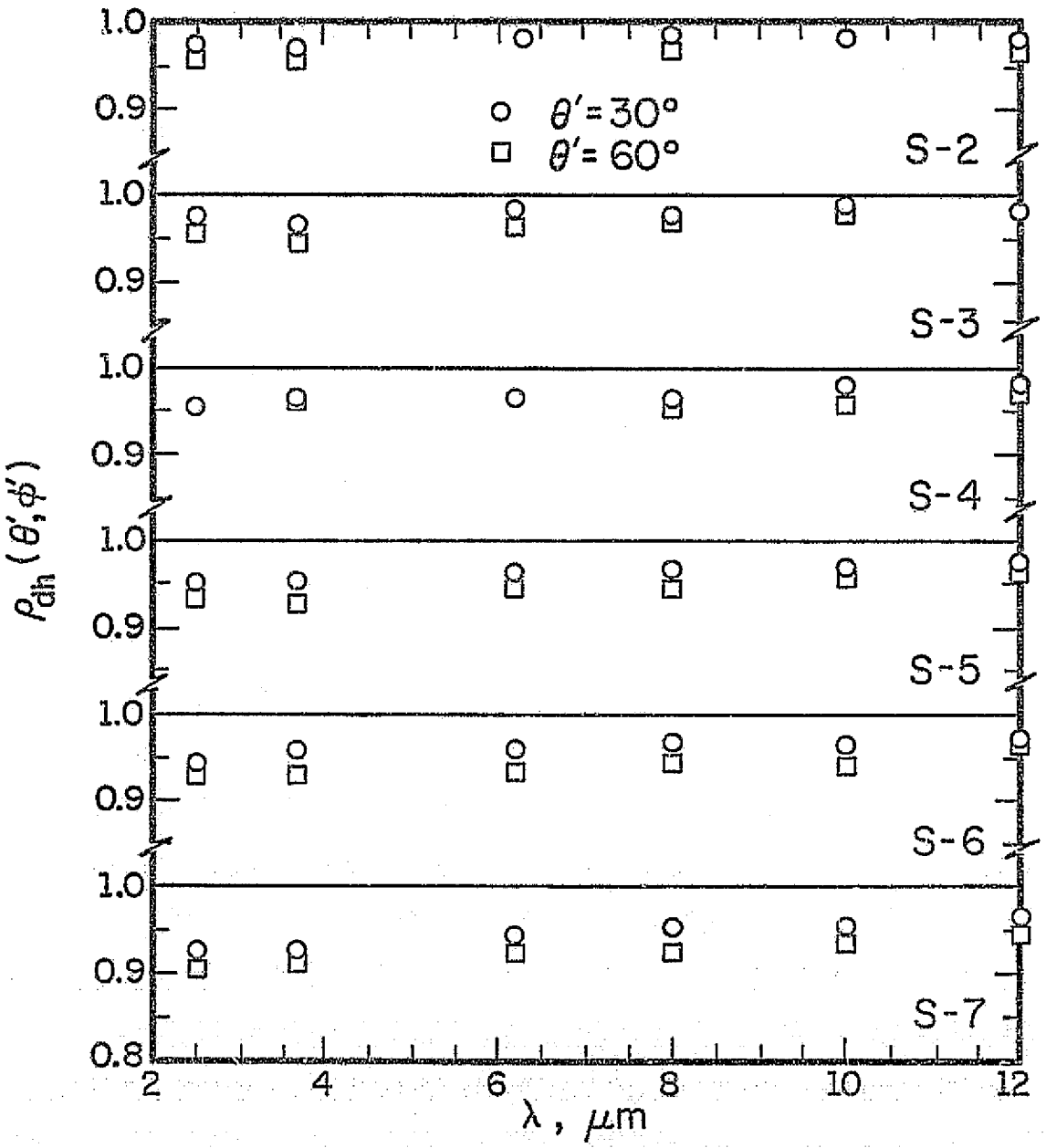

Figure 6.19 Directional Reflectance Measurements for Stainless Steel Rough Samples

degrees exhibiting differences of about 2 percent. Although some directional reflectance trends have been cited in conjunction with the discussion for SPR and BDR, additional trends may be noted. In agreement with SPR and BDR, rough surface directional reflectance approaches that of a smooth surface as wavelength increases. Increasing surface roughness results in decreasing directional reflectance. However, as observed at a wavelength of 2.5 μm, directional reflectance for the roughest sample (A-9) differs by less than 10 percent of smooth surface SPR. Except for the A-5 through A-9 samples for wavelengths shorter than 3.7 μm, directional reflectances are nearly identical for polar angles of incidence equal to 20 and 30 degrees and show a decrease for 60 degrees. Directional reflectance for the A-6 through A-9 samples at wavelengths shorter than 3.7 μm and for polar angle of incidence equal to 20 degrees are lower than those for 30 degrees by approximately 1 percent. With the exception of the S-8 sample and the A-7 as well as A-8 samples whose results nearly coincide, directional reflectances are order with SPR.

As observed in the previous two sections, SPR and BDR measurements could be correlated with optical roughness and rms slope. Similar correlations were examined for directional reflectance measurements by plotting these measurements versus optical roughness as shown in Fig. 6.20 for polar angle of incidence equal to 30 degrees. It is observed in this figure that directional reflectances decrease as optical roughness increases and exhibit a tendency to be ordered in sequence with rms slope for the largest optical roughness values presented for each sample. This latter trend is applicable when samples of different substrate materials are compared and is particularly evident for the four roughest

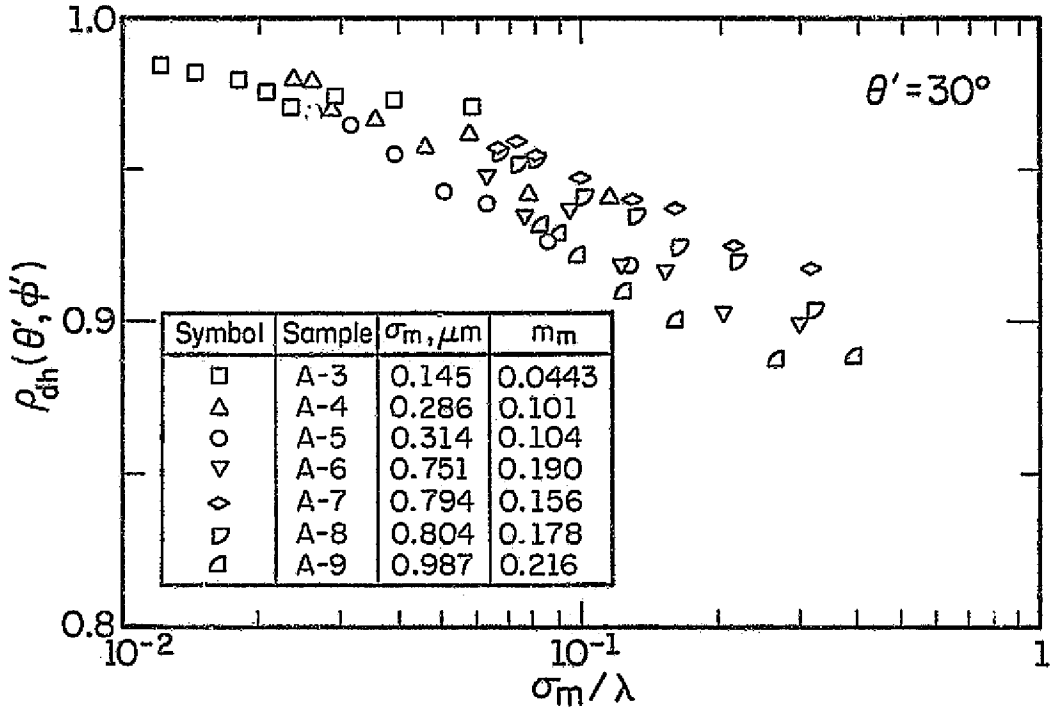

(a) Aluminum alloy samples

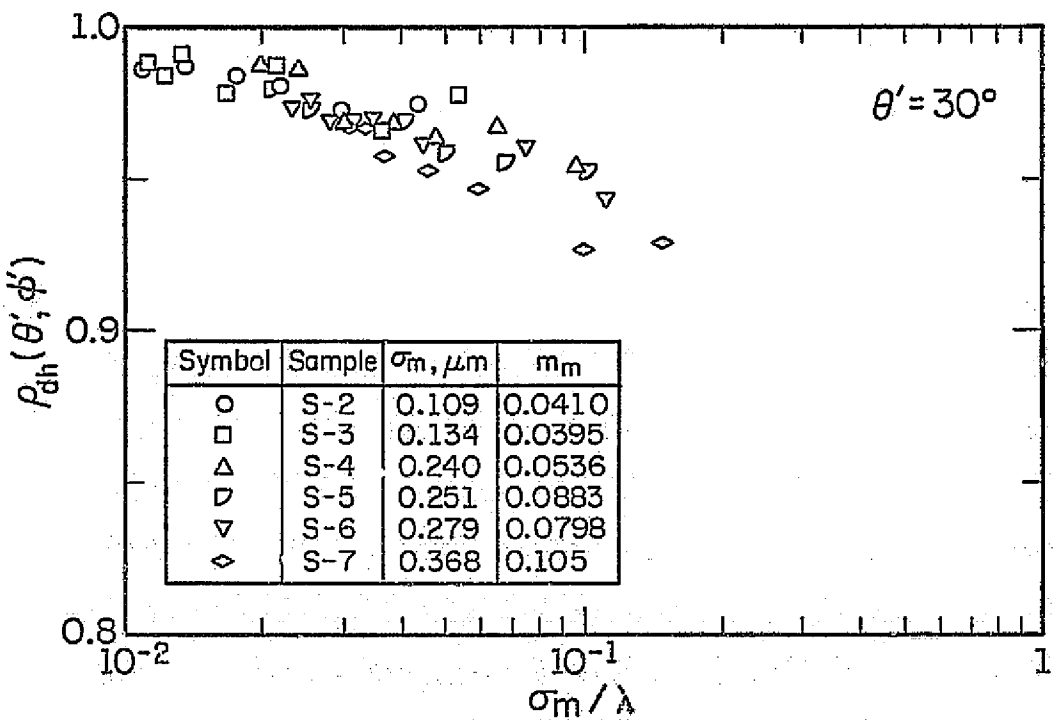

(b) Stainless steel samples

Figure 6.20 Directional Reflectance Measurements for Rough Samples

aluminum alloy samples. Directional reflectance measurements reported by other investigators [4,73] for samples with different rms heights do not exhibit this trend. However, rms slopes which were not reported could have been equal. Directional reflectances at the largest optical roughness values shown for each sample are observed to become less sensitive to optical roughness as optical roughness increases. This trend has been observed in previously reported directional reflectance measurements [73].

2

7. EXAMINATION OF A BDR MODEL

It is the purpose of this chapter to compare the Beckmann BDR model discussed in Chapter 4 with reflectance measurements reported in the previous chapter. As noted in Chapter 4, the Beckmann model is limited to perfectly conducting materials and the method employed to account for energy absorption consists of multiplying the results for a perfect conductor by smooth surface SPR. It has been suggested [32,36] that rough surface directional reflectance be used in this method. Since smooth surface SPR and rough surface directional reflectance differ by less than 10 percent as observed in Chapter 6, the method employed here represents a reasonable approximation to account for energy absorption. Examination of the expression for absolute BDR, Eq. (6.2.1), reveals that the first bracket term can be associated with the magnitude of reflected energy, whereas the second bracket term describes the spatial distribution of reflected energy. The Beckmann model, therefore, is examined for its applicability to represent the magnitude and spatial distribution of reflected energy. If the model satisfactorily predicts the spatial distribution of reflected energy but not the magnitude, then SPR measurements could be utilized for the magnitude of reflected energy. It should be noted that the quantity of measurements and necessary equipment for SPR are far less than for BDR. Predictions of the Beckmann model are compared with rough surface SPR and BDR measurements in Sections 7.1 and 7.2, respectively.

7.1 SPR COMPARISON

In order to compare the Beckmann BDR model with SPR measurements, surface roughness parameters rms height and rms slope must be specified. As observed in Figs. 6.8, 6.9, and 6.10, the specular component of the

Beckmann model exhibits only limited agreement with SPR measurements when mechanical rms height is employed. Including the scattered component evaluated with mechanical rms slope is not expected to significantly improve the agreement between the model and SPR measurements. Therefore, an optical method based on SPR measurements [24,26,32] was utilized to evaluate surface roughness parameters. The parameters so determined are referred to as optical rms height σ_o and optical rms slope m_o. At sufficiently long wavelengths and small solid angle of reflection, the contribution of the scattered component to energy reflected into the specular direction is negligible, and the expression for SPR of the Beckmann model, Eq. (4.2.4), reduces to

$$\frac{\rho_{s,r}(\theta',\phi')}{\rho_{s,o}(\theta',\phi')} \simeq \exp\left[-\left(4\pi \frac{\sigma_o}{\lambda} \cos\theta'\right)^2\right] \tag{7.1.1}$$

Thus, with SPR measurements, wavelength, and polar angle of incidence specified, optical rms height can be evaluated. For shorter wavelengths, both the specular and scattered components contribute to energy reflected into the specular direction, and Eq. (4.2.4) can be solved for optical rms slope to yield

$$m_o = \left[\frac{\Delta\omega(\sigma_o/\lambda)^2 P}{2} \exp\{-[(\sigma_o/\lambda) P]^2\} \sum_{M=1}^{\infty} \frac{[(\sigma_o/\lambda) P]^{2M}}{M(M!)} \Bigg/ \left(\frac{\rho_{s,r}(\theta',\phi')}{\rho_{s,o}(\theta',\phi')} - \exp\{-[(\sigma_o/\lambda) P]^2\}\right)\right]^{1/2} \tag{7.1.2}$$

where $P = 4\pi \cos\theta'$. With optical rms height determined, and polar angle of incidence, wavelength, as well as solid angle of reflection specified, optical rms slope can be evaluated from SPR measurements. Since previously reported studies [26,32] correlated the Beckmann model with near-normal incidence SPR and BDR measurements, rough

surface SPR measurements reported in Figs. 6.2, 6.3, and 6.4 for polar angle of incidence equal to 10 degrees were employed in the optical method. Results of the calculations are presented in Table 7.1 for glass, aluminum alloy, and stainless steel rough samples. Optical rms heights were evaluated from SPR measurements for wavelengths longer than 11 μm and optical rms slopes from shorter wavelengths. The latter results represent average values [26,32] which gave reasonable agreement between the model and measurements. Optical rms height for the A-2 sample, however, was calculated from SPR measurements for wavelengths shorter than 5.0 μm and optical rms slope is not reported since SPR measurements are adequately represented by the specular component. Graphical comparisons of mechanical and optical surface roughness parameters are displayed in Fig. 7.1 where optical rms height is plotted versus mechanical rms height and optical rms slope versus mechanical rms slope. With the exception of five samples, optical rms heights are smaller than mechanical rms heights. Optical peak-to-valley heights [68] which can be expressed in terms of optical rms heights are also generally smaller than mechanical peak-to-valley heights. These observations are contrary to those reported by other investigators [26, 61] where, for metallic surfaces, mechanical rms heights are smaller than optical rms heights. A possible explanation for the conflicting trends is the method by which mechanical rms height values were acquired. The present values as well as those reported in [68] were evaluated from digitized surface profile measurements as discussed in Chapter 5, whereas the other reported values [26,61] were electronically evaluated. Although results from the two methods are expected to be equivalent, no documentation appears to substantiate this conjecture. Optical rms slopes are less than mechanical rms slopes by about the

Table 7.1

Mechanical and Optical Surface Roughness Parameters

Sample	σ_m [1]	σ_o [2]	m_m [3]	m_o [4]
G-2	0.270	0.265	0.0834	0.0109
G-3	0.358	0.323	0.108	0.0139
G-4	0.374	0.491	0.133	0.0208
G-5	0.837	0.708	0.142	0.0366
G-6	0.927	0.950	0.274	0.0536
A-2	0.0570	0.0309	0.0238	
A-3	0.145	0.174	0.443	0.00919
A-4	0.286	0.233	0.101	0.0422
A-5	0.314	0.338	0.104	0.0298
A-6	0.751	0.666	0.190	0.0643
A-7	0.794	0.564	0.156	0.0437
A-8	0.804	0.559	0.178	0.0432
A-9	0.987	0.842	0.216	0.0665
S-2	0.109	0.0800	0.0410	0.0250
S-3	0.134	0.133	0.0395	0.0149
S-4	0.240	0.246	0.0536	0.0147
S-5	0.251	0.238	0.0798	0.0202
S-6	0.279	0.241	0.0883	0.0207
S-7	0.368	0.306	0.105	0.0247
S-8	0.496	0.343	0.0300	0.0130

[1]Mechanical rms height, μm;

[2]Optical rms height, μm;

[3]Mechanical rms slope; and

[4]Optical rms slope.

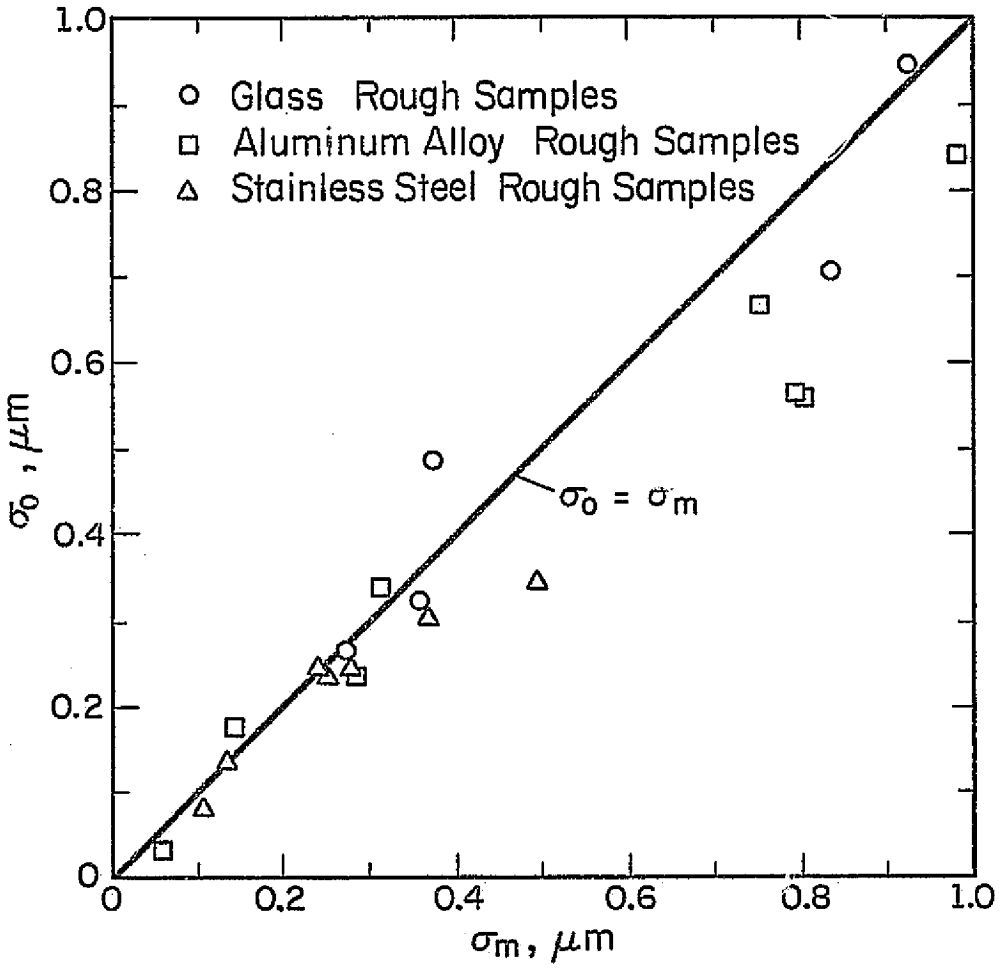

(a) rms heights

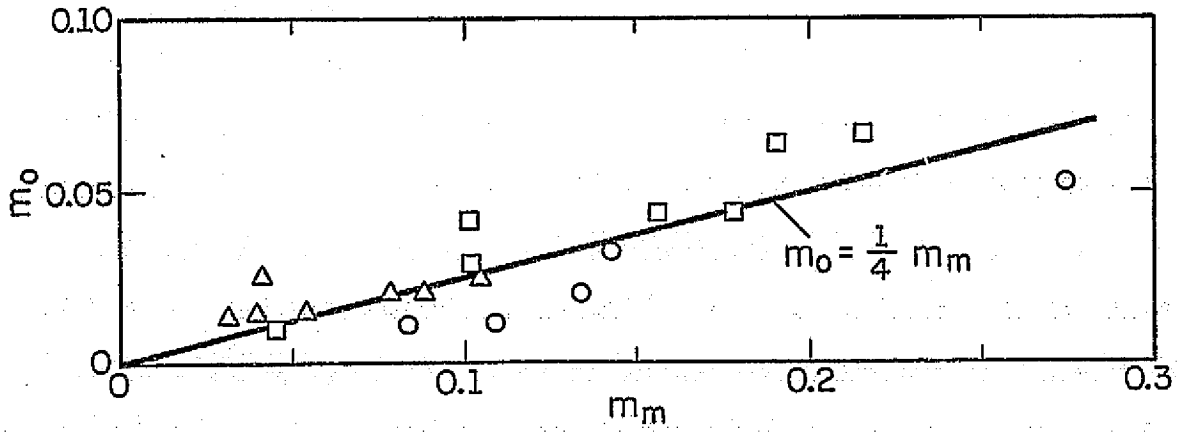

(b) rms slopes

Figure 7.1 Optical and Mechanical Surface Roughness Parameters

factor 4. Part of this difference could be attributed to the method of determination of optical rms slope. Agreement between optical and mechanical rms slopes could be improved but such adjustments reduce the correlation between the model and SPR measurements as is discussed later.

SPR measurements for polar angles of incidence equal to 10 and 30 degrees were correlated with the parameter $(\sigma_m/\lambda) \cos \theta'$ as shown in Figs. 6.8, 6.9, and 6.10. Recognizing this correlation, SPR measurements for polar angles of incidence equal to 10 and 30 degrees are plotted as a function of the parameter $(\sigma_o/\lambda) \cos \theta'$ in Figs. 7.2, 7.3, and 7.4 for glass, aluminum alloy, and stainless steel rough samples, respectively. Trends similar to those reported for $(\sigma_m/\lambda) \cos \theta'$ are displayed in these figures. Using optical rms height and rms slope values reported in Table 7.1, SPR results were calculated from Eq. (4.2.4) and are illustrated in Figs. 7.2, 7.3, and 7.4. The specular component given by Eq. (7.1.1) is represented by a single solid curve. The sum of the specular component and the contribution of the scattered component to energy reflected into the specular direction as expressed by Eq. (4.2.4) is represented by broken curves for polar angles of incidence equal to 10 and 30 degrees. Calculated SPR values increase with increasing $(\sigma_o/\lambda) \cos \theta'$ for samples with optical rms slopes less than about 0.025. The increase of SPR results is attributed to the scattered component. SPR measurements for these samples do not display this characteristic. As expected, agreement between the specular component and measurements is observed at the smallest $(\sigma_o/\lambda) \cos \theta'$ values for each sample and is extended to larger values of this parameter by including the scattered component. As optical rms slope increases, correlation extends to larger $(\sigma_o/\lambda) \cos \theta'$ values. Contrary to what other investigators have reported, specifying a $(\sigma_o/\lambda) \cos \theta'$ value to which correlation exists between the model and measurements is insufficient information. Optical

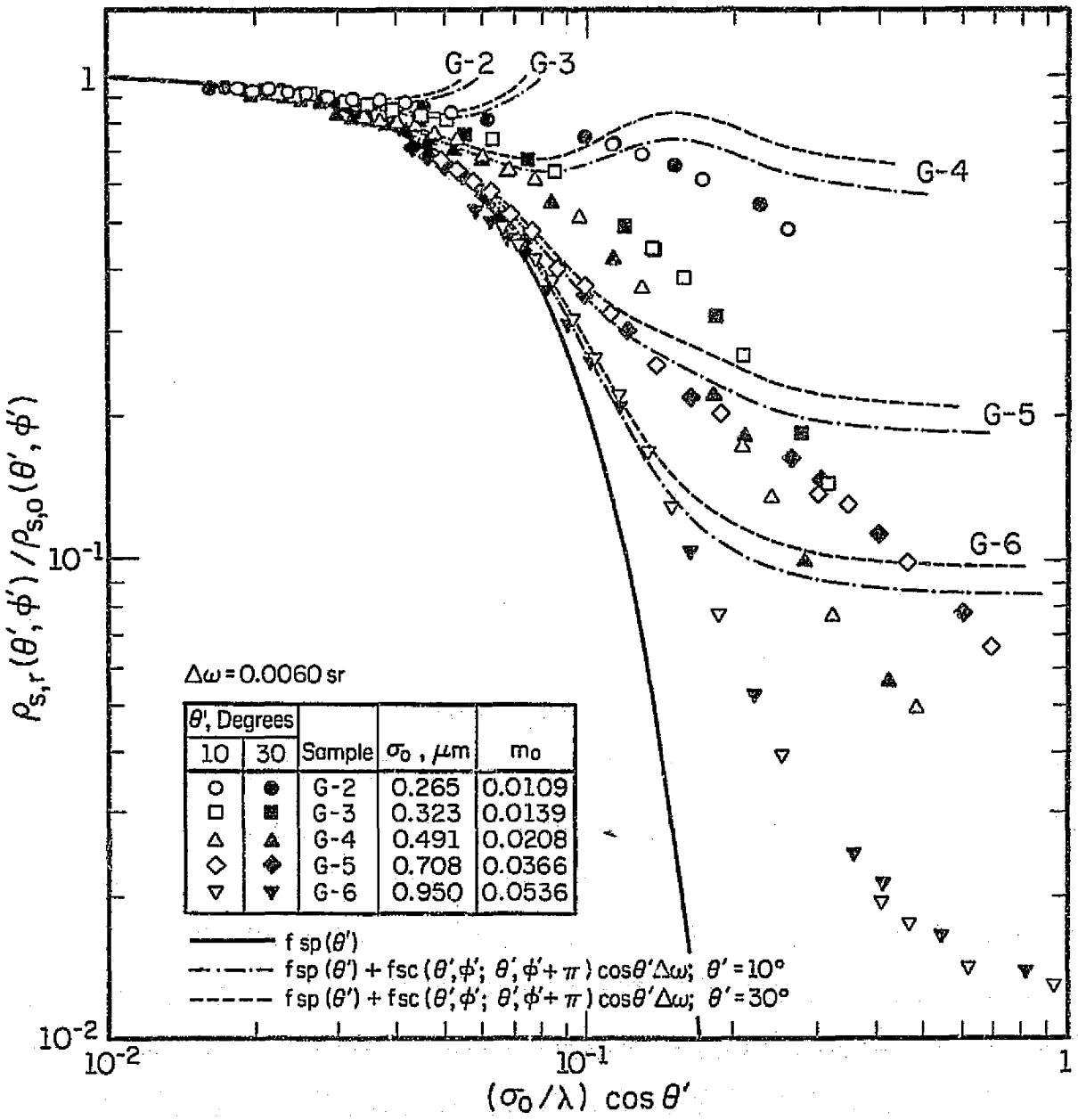

Figure 7.2 Comparison of Beckmann Model with SPR Measurements for Glass Rough Samples

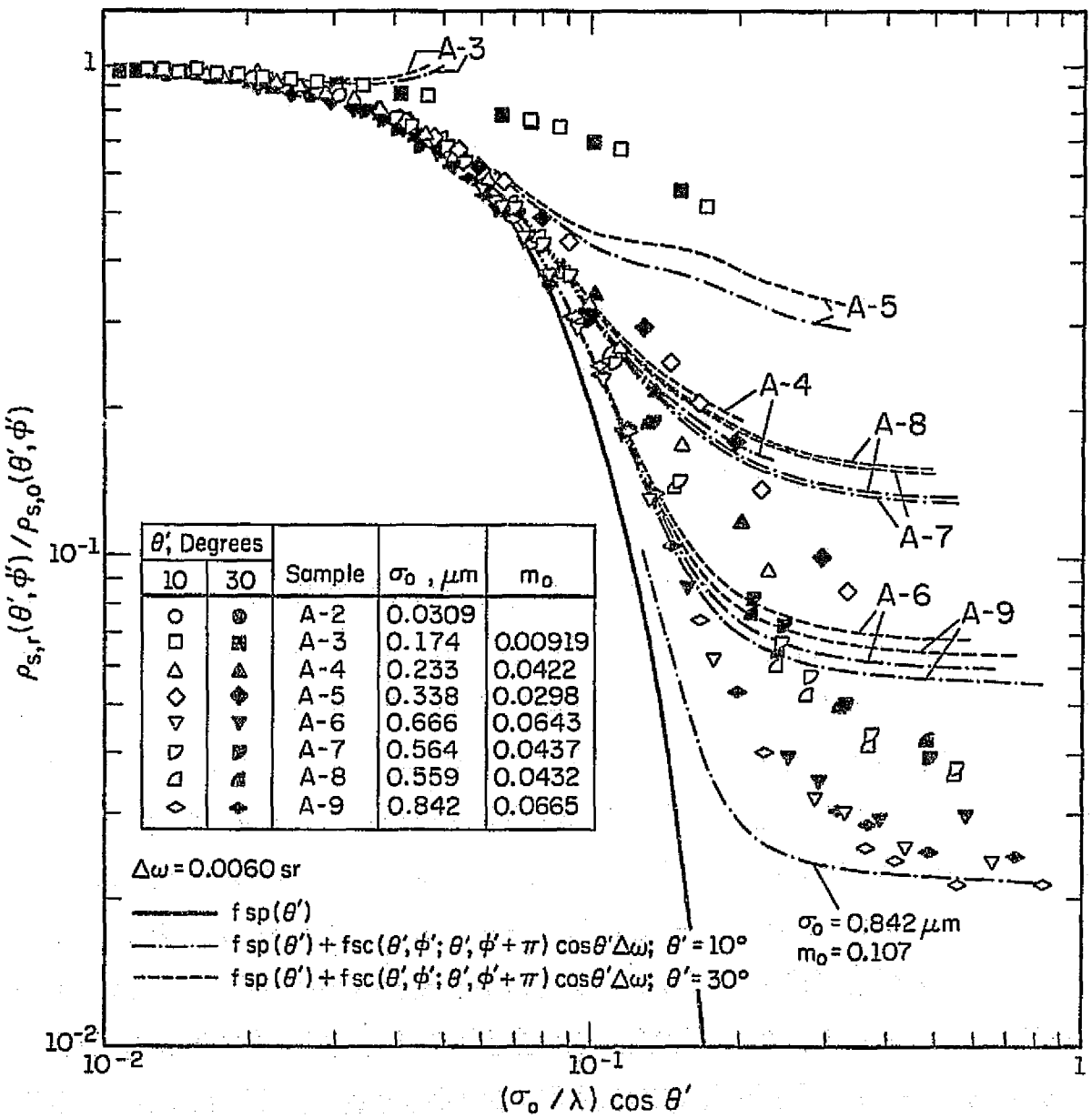

Figure 7.3 Comparison of Beckmann Model with SPR Measurements for Aluminum Alloy Rough Samples

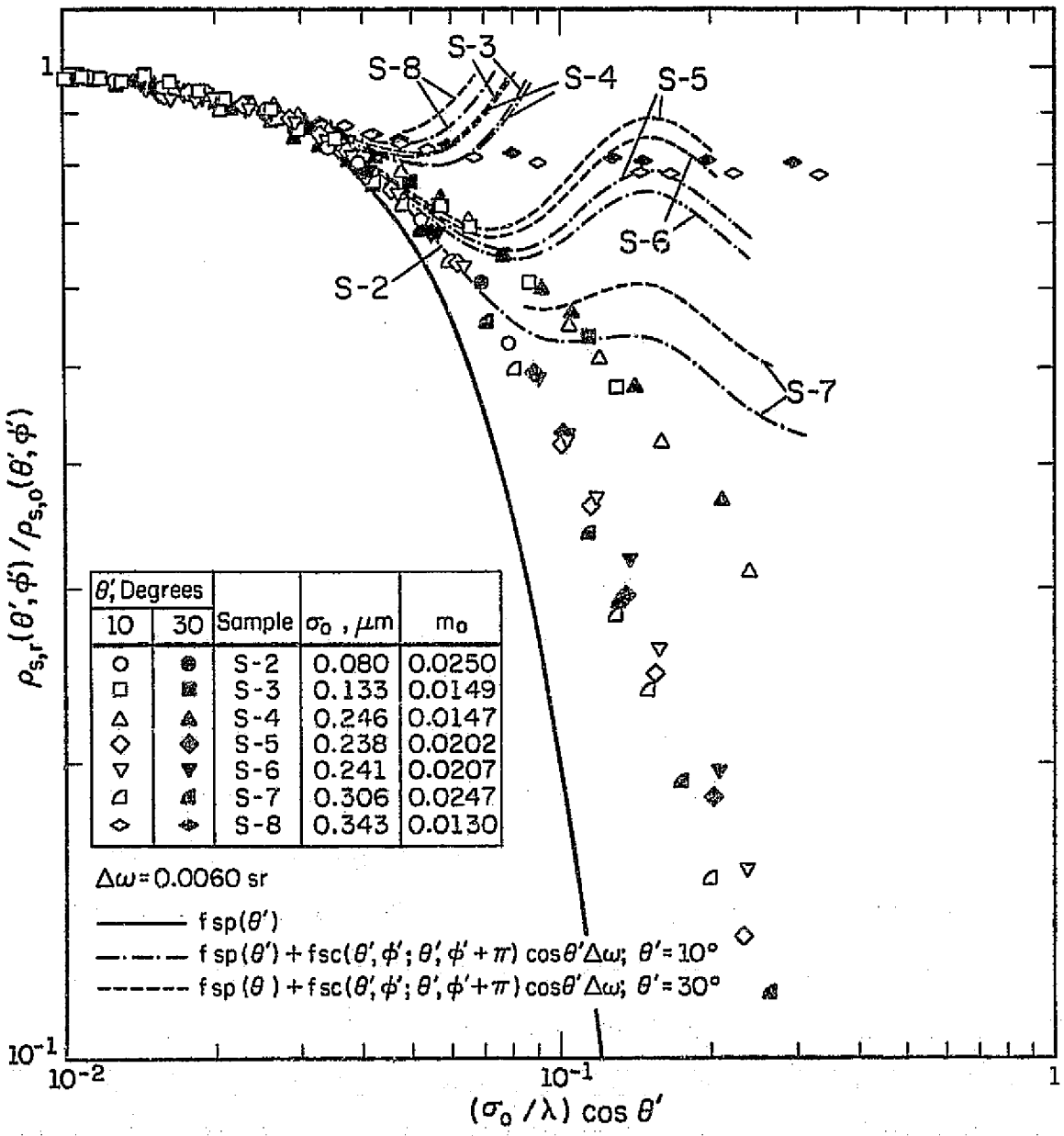

Figure 7.4 Comparison of Beckmann Model with SPR Measurements for Stainless Steel Rough Samples

rms slope must also be reported in defining the range of application of the Beckmann model. For reported SPR measurements, $(\sigma_o/\lambda) \cos \theta'$ values for which agreement exists are less than approximately 27 m_o. A slight reduction of $(\sigma_o/\lambda) \cos \theta'$ values where agreement exists is observed for polar angle of incidence equal to 30 degrees. For larger polar angles of incidence, agreement between the model and SPR measurements is unsatisfactory and further examination is required.

Optical rms slopes larger than those reported in Table 7.1 would significantly improve the correlation at larger $(\sigma_o/\lambda) \cos \theta'$ values for each sample but yield poorer agreement for smaller values. This is illustrated for the A-9 sample in Fig. 7.3 for polar angle of incidence equal to 10 degrees where optical rms slope was adjusted to equal 0.107 so that SPR results and measurements coincide at the two largest $(\sigma_o/\lambda) \cdot \cos \theta'$ values for this sample. For $(\sigma_o/\lambda) \cos \theta'$ values between 0.1 and 0.5, agreement is unsatisfactory. For the larger $(\sigma_o/\lambda) \cos \theta'$ values, however, shadowing effects and multiple reflections which are not accounted for by the model become increasingly important. Thus, it is more appropriate to select optical rms slope from SPR measurements for smaller values where the validity of the model is open to less criticism.

7.2 BDR COMPARISON

In order to compare BDR distributions predicted by the Beckmann model with BDR measurements presented in Chapter 6, surface roughness parameters rms height and rms slope must be specified. There are basically three methods for selection of surface roughness parameters for use in the model. The first method uses mechanical rms heights and rms slopes reported in Table 5.1. For both the second and third methods,

the optical rms heights reported in Table 7.1 are employed. For the second surface roughness parameter, optical rms slopes evaluated for each wavelength as expressed by Eq. (7.1.2) are utilized in the second method, whereas average optical rms slopes given in Table 7.1 are used in the third method. A fourth method which was not considered in the present study consists of a trial and error selection of surface roughness parameters. Results calculated from the Beckmann model for the three methods are compared in Fig. 7.5 with BDR measurements for the A-4 sample at polar angle of incidence equal to 10 degrees and wavelengths of 1.5 and 6.2 μm. Only results for the scattered component are displayed and, therefore, $\overline{R}$ for the Beckmann model is expressed as

$$\overline{R} = \frac{f_{sc}(\theta',\phi';\theta,\phi)\cos\theta\,\Delta\omega}{f_{sp}(\theta') + f_{sc}(\theta',\phi';\theta',\phi'+\pi)\cos\theta'\,\Delta\omega} \qquad (7.2.1)$$

At the shorter wavelength (λ = 1.5 μm), $\overline{R}$ for the Beckmann model is nearly unity in the specular direction which implies that the scattered component dominates. The scattered component in this instance represents 99.6 and 97.3 percent of reflected energy when mechanical and optical rms heights are employed, respectively. At the longer wavelength (λ = 6.2 μm), the specular component accounts for 72.2 and 80.5 percent of reflected energy for mechanical and optical rms heights, respectively. Results calculated at the longer wavelength using mechanical surface roughness parameters display significantly more scattering than that indicated by the measurements. At the shorter wavelength, results calculated using these parameters display more scattering for polar angles of reflection in the vicinity of the specular direction and less scattering at angles removed from this direction. Results for optical surface roughness parameters evaluated using the second and

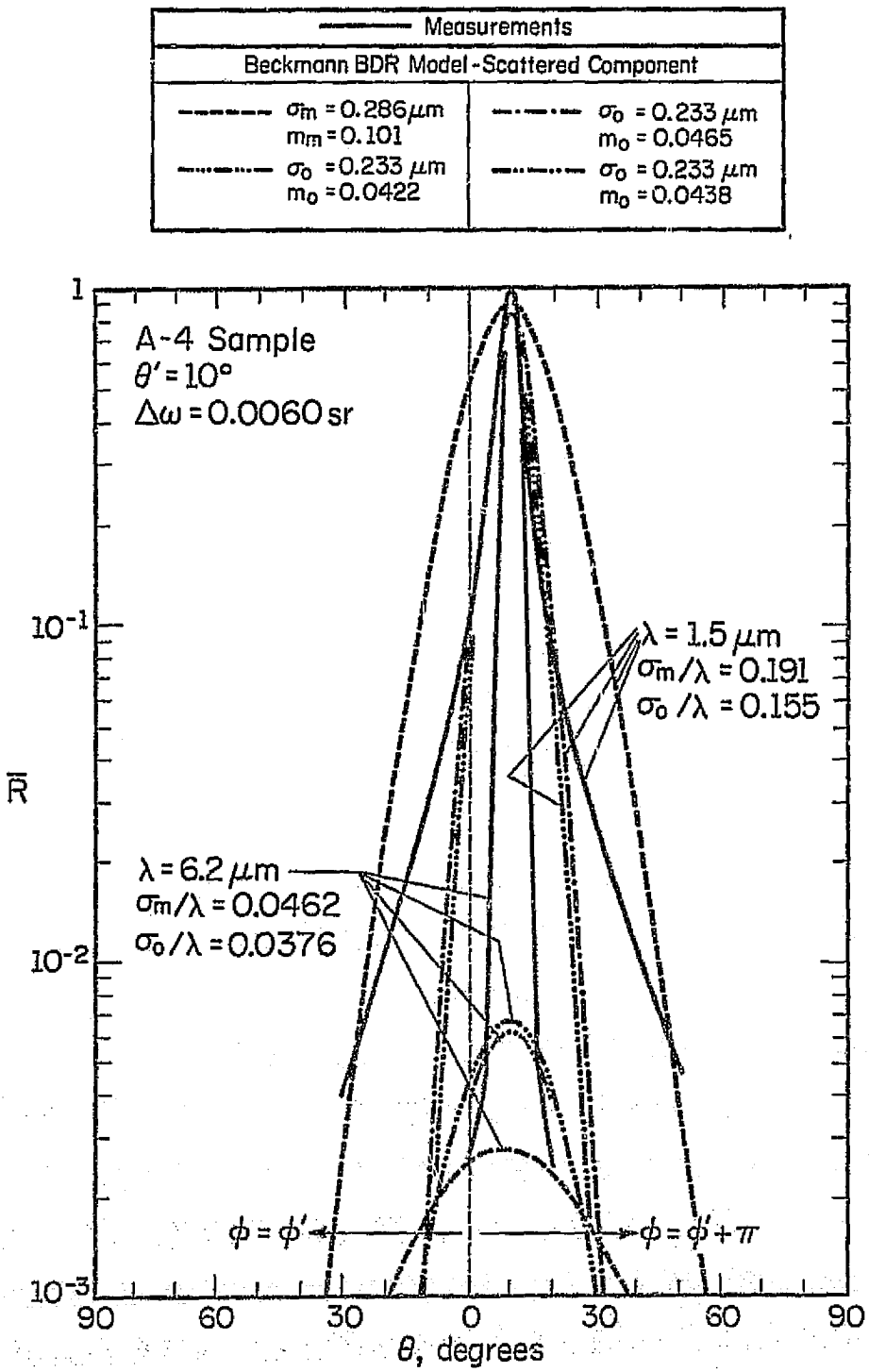

Figure 7.5 Comparison of Beckmann Model for Different Surface Roughness Parameters with BDR Measurements

third methods exhibit reasonable agreement with BDR measurements at the longer wavelength. Agreement exists at the shorter wavelength, however, only for polar angles of reflection near the specular direction and the model displays less scattering at other polar angles of reflection. Of the three considered methods for selection of surface roughness parameters, the second method based on optical rms height and optical rms slope evaluated at each wavelength yields BDR distributions that adequately describe BDR measurements. The agreement, however, is limited to nearly specular reflection BDR distributions. It should be recalled that SPR results from the second method correctly represent SPR measurements for polar angle of incidence equal to 10 degrees and satisfactorily represent SPR measurements for 30 degrees.

Using optical rms heights reported in Table 7.1 and optical rms slopes evaluated from SPR measurements for each wavelength, BDR distributions were calculated from the Beckmann model. Representative BDR distributions for the G-3, A-3, and S-7 samples are displayed with corresponding BDR measurements in Figs. 7.6, 7.7, and 7.8, respectively, for polar angles of incidence equal to 10, 30, 60, and 80 degrees. Only results for the scattered component are displayed since the specular component does not contribute at polar angles of reflection outside a ± 5 degree angular interval of the specular direction. BDR distributions calculated from the Beckmann model adequately represent BDR measurements for wavelengths longer than those shown in these figures and deviate significantly for shorter wavelengths. As polar angle of incidence increases, there is a decrease in the degree of correlation between the model and measurements. The scattered component for polar angle of incidence equal to 80 degrees is observed to exhibit maxima at polar angles of

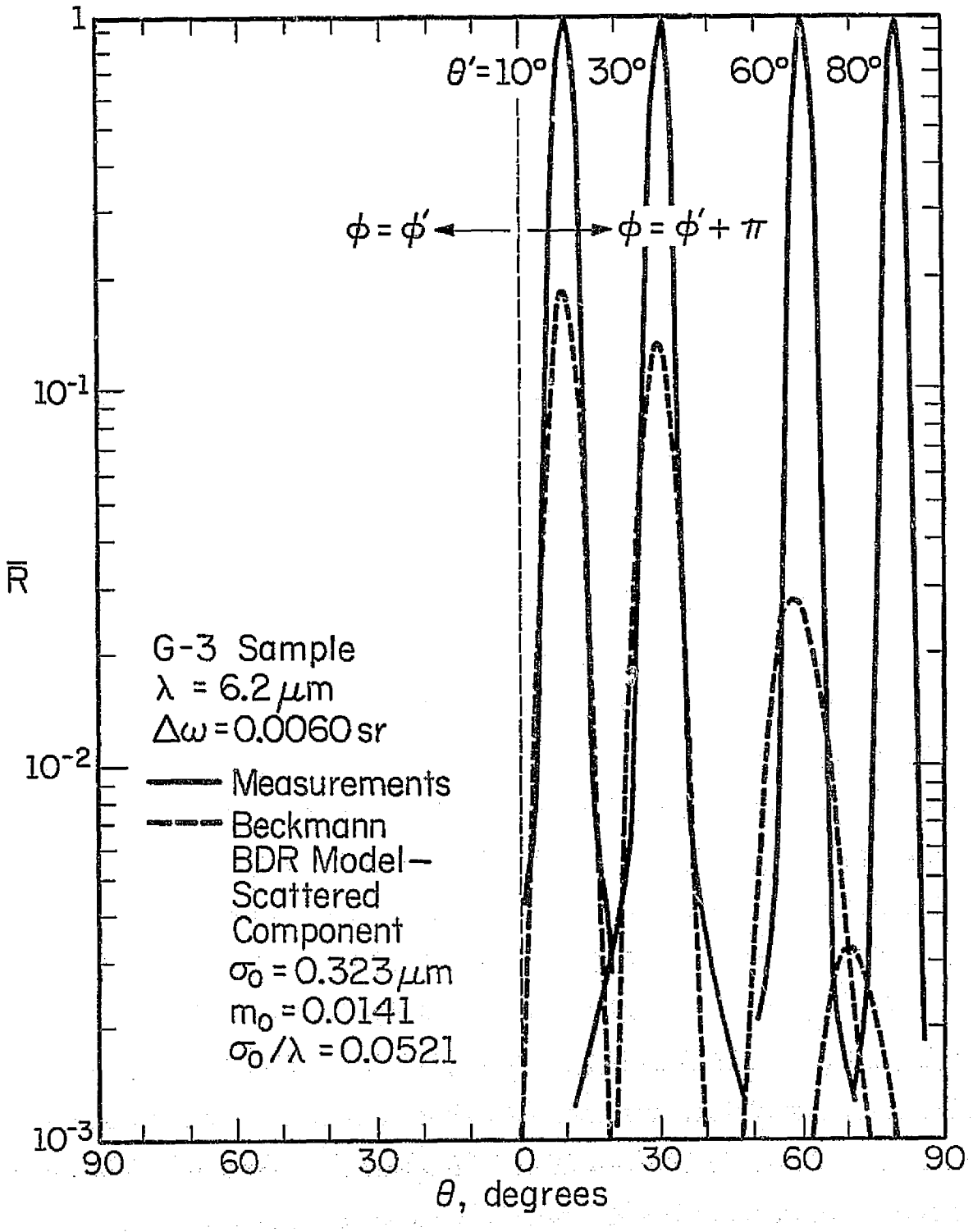

Figure 7.6 Comparison of Beckmann Model with BDR Measurements for G-3 Samples

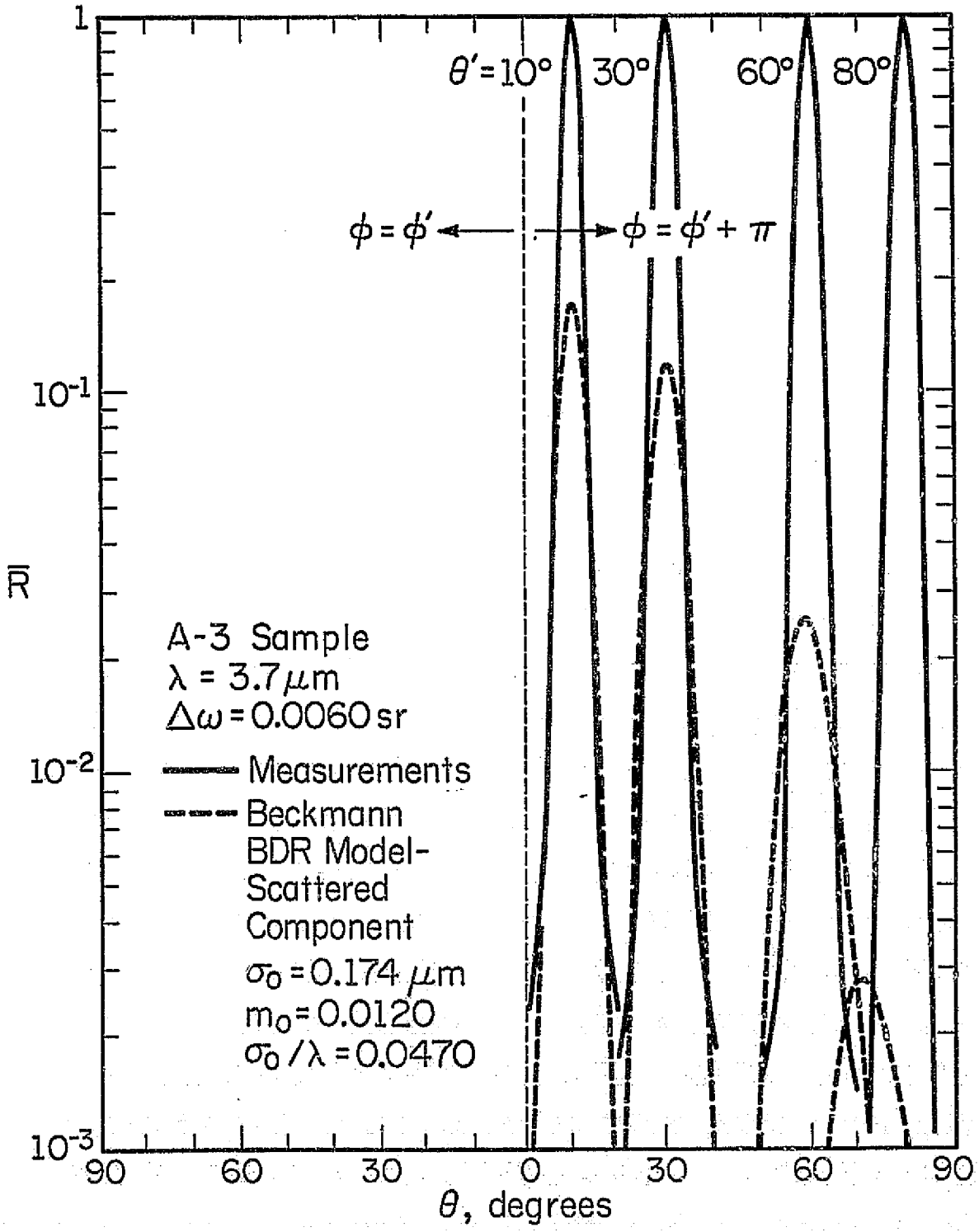

Figure 7.7 Comparison of Beckmann Model with BDR Measurements for A-3 Samples

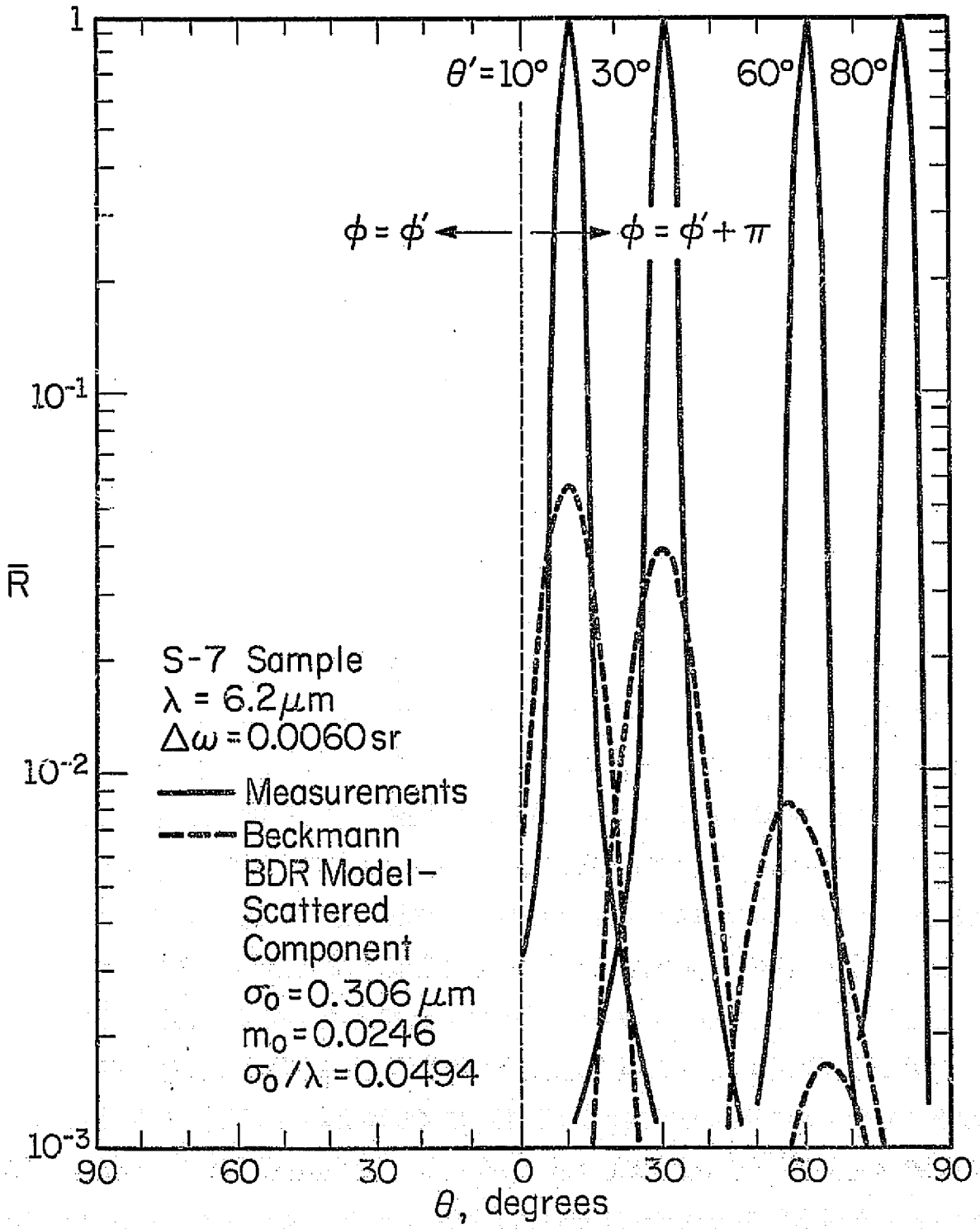

Figure 7.8 Comparison of Beckmann Model with BDR Measurements for S-7 Sample

reflection smaller than the specular direction. BDR measurements do not exhibit this characteristic. The lack of correlation with increasing polar angle of incidence is offset by a decrease in the amount of reflected energy represented by the scattered component. At a polar angle of incidence equal to 80 degrees, the specular component accounts for approximately 98 percent of reflected energy for the optical roughness values (σ_o/λ) shown in these figures and, furthermore, represents BDR measurements. Thus, although BDR measurements are adequately described by the model, SPR measurements and, consequently, the magnitude of reflected energy are not represented by the model as was discussed in the previous section. Based on comparisons presented in Figs. 7.6, 7.7, and 7.8, as well as those not reported, the Beckmann model satisfactorily describes BDR measurements providing optical roughness and rms slope evaluated from SPR measurements for each wavelength are less than 0.05 and 0.02, respectively.

8. SUMMARY AND CONCLUSIONS

An experimental study of surface roughness effects on bidirectional reflectance of metallic surfaces has been reported. A facility capable of irradiating a sample from normal to grazing incidence and recording plane of incidence bidirectional reflectance measurements was developed. Samples consisting of glass, aluminum alloy, and stainless steel materials were selected for examination. Samples were roughened using standard grinding techniques and coated with a radiatively opaque layer of pure aluminum. Mechanical surface roughness parameters rms heights and rms slopes evaluated from digitized surface profile measurements were less than 1.0 μm and 0.28, respectively. Rough surface specular, bidirectional, and directional reflectance measurements for selected values of polar angle of incidence and wavelength of incident energy within the spectral range 1 to 14 μm were reported. The Beckmann bidirectional reflectance model was selected for comparison with reflectance measurements.

Several trends were evident from reflectance measurements. First, as wavelength increased, rough surface monochromatic reflectances (specular, bidirectional, directional) approached the values appropriate to the corresponding reflectances of a smooth surface at the same direction of incident energy. Second, the influence of direction of incident energy on rough surface monochromatic reflectance may be summarized as follows. At short wavelengths, specular reflectance increased with polar angle of incident energy throughout the entire range of polar angle of incidence investigated (10 to 80 degrees). Although the same trend was evident at long wavelengths, it was limited to polar angles of incidence from 10 to 60 degrees; for larger angles, specular reflectance decreased as polar angle of incidence varied from 60 to 80 degrees. Bidirectional reflectance

approached that of a smooth surface as polar angle of incidence varied from near-normal to near-grazing incidence. Directional reflectance was invariant with polar angle of incident energy for polar angles of incidence less than 30 degrees and decreased as polar angle of incidence was increased to larger values. Third, surface roughness significantly influenced the reflectance properties of the materials. Monochromatic specular and directional reflectances diminished as surface roughness increased with this trend being more pronounced at short wavelengths than at long wavelengths. Bidirectional reflectance measurements confirmed that as surface roughness increased, the distribution of reflected energy departed from that of a smooth surface to a distribution with significant amounts of reflected energy in directions of reflection other than the specular direction. The spatial distribution of reflected energy, however, continued to be concentrated in directions of reflection not very far removed from the specular direction for the rough surfaces examined. Fourth, convenient parameters for examining the influence of surface roughness on reflectance measurements are optical roughness and mechanical rms slope. Optical roughness is defined as the ratio of mechanical rms height to wavelength of incident energy and has values less than unity for the rough surfaces examined. As optical roughness decreased, rough surface monochromatic reflectance asymptotically approached that of a smooth surface. As optical roughness increased, specular and directional reflectances decreased and the influence of mechanical rms slope becomes more apparent. For the larger values of optical roughness, specular and directional reflectances are ordered according to mechanical rms slope with smaller reflectance values corresponding to larger rms slope values. Specular reflectances for polar angles of incidence equal to 10 and 30

degrees for each sample lie along a single curve when plotted as a function of the parameter formed by multiplying optical roughness by the cosine of polar angle of incidence; for larger angles, specular reflectances deviated considerably from this correlation. Bidirectional reflectances for rough surfaces with nearly identical mechanical rms slopes demonstrated that as optical roughness increased, greater amounts of reflected energy are found in directions of reflection further removed from the specular direction. Rough surfaces with nearly identical optical roughness displayed a corresponding trend as mechanical rms slope increased. These conclusions illustrate the importance of reporting surface roughness parameters rms height and rms slope in experimental studies similar to that presented here.

The Beckmann bidirectional reflectance model was compared with reflectance measurements to establish its usefulness in describing the magnitude and spatial distribution of energy reflected from rough surfaces. Comparisons reveal several general conclusions. First, specular and bidirectional reflectance results calculated from the model using mechanical surface roughness parameters did not agree with the corresponding monochromatic reflectance measurements. Specifically, bidirectional reflectance results evaluated at long wavelengths displayed greater amounts of reflected energy in directions of reflection other than the specular direction. At short wavelengths, a similar trend is evident but is limited to directions of reflection near the specular direction; at larger directions of reflection, results evaluated from the model exhibited smaller amounts of reflected energy. Second, a significant improvement between predictions of the model and reflectance measurements is observed when optical surface roughness parameters were used in the model.

An optical method based on monochromatic specular reflectance measurements for near-normal incidence provided optical rms height and optical rms slope evaluated at each wavelength. Optical rms height then replaces mechanical rms height in the definition of optical roughness. Average values of optical rms slopes calculated from those for each wavelength were used to evaluate specular reflectance results from the model. Agreement between the results calculated from the model using optical surface roughness parameters and reflectance measurements is summarized in the following observations. Monochromatic specular reflectance measurements for polar angle of incidence equal to 10 degrees are adequately described by specular reflectance results evaluated from the model when values of optical roughness multiplied by the cosine of polar angle of incidence are less than 27 times average optical rms slope. Results for polar angle of incidence equal to 30 degrees exhibited a slight reduction in this limiting value, and a lack of agreement is observed for larger polar angles of incidence. Bidirectional reflectance results calculated from the model using optical rms height and optical rms slope evaluated for each wavelength adequately represented monochromatic bidirectional reflectance measurements provided optical roughness and optical rms slope are less than 0.05 and 0.02, respectively.

This study of surface roughness effects on bidirectional reflectance has suggested several areas of further investigation. First, reflectance measurements for optical roughness and rms slope values greater than those reported would assist in further defining as well as extending the cited trends and correlations. Second, reflectance measurements for rough surfaces with different coating materials as well as without a coating would aid in further understanding and defining the influence of the various

surface characteristics. Third, evaluation and interpretation of surface roughness parameters derived from profilometer measurements or possibly from scanning electron microscope photographs require further examination. Fourth, polarization effects should be considered in future studies. Finally, examination of recently reported expressions for the scattering of electromagnetic waves from rough surfaces could produce a bidirectional reflectance model that has a different range of engineering application than that for the Beckmann model.

REFERENCES

1. Eckert, E. R. G., "Messung der Reflexion von Wärmstrahlen an Technischen Oberflachen," Forschung auf dem Gebiete des Ingenieurwessens, 7, 265 (1936).

2. Münch, B., "Die Richtungsverteilung bei der Reflexion von Wärmestrahlung und ihr Einfluss Auf die Wärmeubertragung," Mitteilunger aus den Institut für Thermodynmak und Verbrennungsmotoranban au der Eidgenössischen Technischen Hochschule in Zürich, No. 16 (1955).

3. Agnew, J. T. and McQuistan, R. B., "Experiments Concerning Infrared Diffuse Reflectance Standards in the Range 0.8 to 20.0 Microns," J. Opt. Soc. Amer., 43, 999 (1953).

4. Birkebak, R. C. and Eckert, E. R. G., "Effects of Roughness of Metal Surfaces on Angular Distribution of Monochromatic Reflected Radiation," Trans. ASME, J. Heat Transfer, 87C, 85 (1965).

5. Torrance, K. E. and Sparrow, E. M., "Biangular Reflectance of an Electric Nonconductor as a Function of Wavelength and Surface Roughness," Trans. ASME, J. Heat Transfer, 87C, 283 (1965).

6. Torrance, K. E. and Sparrow, E. M., "Off-Specular Peaks in the Directional Distribution of Reflected Thermal Radiation," Trans. ASME, J. Heat Transfer, 88C, 223 (1966).

7. Herold, L. M. and Edwards, D. K., "Bidirectional Reflectance Characteristics of Rough, Sintered-Metal, and Wire-Screen Surface Systems," AIAA J., 4, 1802 (1966).

8. Love, T. J. and Francis, R. E., "Experimental Determination of Reflectance Function for Type 302 Stainless Steel," Progress in Astronautics and Aeronautics, Academic Press, New York (1967).

9. Collignon, F., "Etude des Indicatrices de Réflexion d'une Surface Rugueuse Soumise au Rayonnement Thermique," Rev. Gén. Therm., 8, 733 (1969).

10. Shcherbina, D. M., Kirichenko, A. P., and Aliev, R. S., "Characteristic Reflection Curves with Normal Irradiation of a Surface," High Temp., 6, 351 (1968).

11. Shcherbina, D. M. and Kirichenko, A. P., "Precision in Measuring the Emissivity Factor in Reflecting Furnaces," Meas. Tech., No. 7, 871 (1968).

12. "Surface Texture," American Standard, ASA B46.1-1962.

13. Smith, T. F. and Hering, R. G., "Bidirectional Reflectance of a Randomly Rough Surface," AIAA Paper No. 71-465, presented at AIAA Sixth Thermophysics Conference (April 1971), to be published in Progress in Astronautics and Aeronautics, Vol. 29.

14. Bennett, H. E., "Influence of Surface Roughness, Surface Damage and Oxide Films on Emittance," Symposium on Thermal Radiation of Solids, NASA SP-55, 145 (1965).

15. Sparrow, E. M. and Cess, R. D., Radiation Heat Transfer, Brooks/Cole, Belmont, California (1966).

16. Brandenberg, W. M., "The Reflectivity of Solids at Grazing Angles," Measurement of Thermal Radiation Properties of Solids, NASA SP-31, 75 (1963).

17. Holl, H. B., "Specular Reflection and Characteristics of Reflected Light," J. Opt. Soc. Amer., 57, 683 (1967).

18. Hering, R. G. and Smith, T. F., "Surface Radiation Properties from Electromagnetic Theory," Int. J. Heat Mass Transfer, 11, 1567 (1968).

19. Ruiz-Urbieta, M., Sparrow, E. M., and Eckert, E. R. G., "Methods for Determining Film Thickness and Optical Constants of Films and Substrates," J. Opt. Soc. Amer., 61, 351, (1971).

20. Beattie, J. R. and Conn, G. K. T., "Optical Constants of Metals in the Infrared--Principles of Measurement," Phil. Mag., 46, Series 7, 222 (1955).

21. Juenker, D. W., "Digital Evaluation of the Complex Index of Refraction from Reflectance Data," J. Opt. Soc. Amer., 55, 295 (1965).

22. Jones, M. C. and Palmer, D. C., "A Technique for the Measurement of Spectral Reflectance at Low Temperatures in the Infrared and Far Infrared," Progress in Astronautics and Aeronautics, 21, 543, Academic Press, New York (1969).

23. Gorton, A. F., "Reflection from, and Transmission through, Rough Surfaces," Phys. Rev., 7, Second Series, 66 (1916).

24. Bennett, H. E., "Specular Reflectance of Aluminized Ground Glass and the Height Distribution of Surface Irregularities," J. Opt. Soc. Amer., 53, 1389 (1963).

25. Bennett, H. E. and Porteus, J. O., "Relation between Surface Roughness and Specular Reflectance at Normal Incidence," J. Opt. Soc. Amer., 51, 123 (1961).

26. Smith, T. F. and Hering, R. G., "Comparison of Bidirectional Reflectance Measurements and Model for Rough Metallic Surfaces," ASME Proceedings of the Fifth Symposium on Thermophysical Properties, 429 (1970).

27. Pouey, M. and Fabre, D., "Quelques Expériences de Diffusion du Rayonnement Ultraviolet par des Surfaces Rugueuses,"Optica Acta, 16, 471 (1969).

28. Latta, M. R., "The Scattering of 10.6 Micron Radiation from Ground Glass Surfaces," J. Opt. Soc. Amer., 59, 493 (1969).

29. Beckmann, P. and Spizzichino, A., The Scattering of Electromagnetic Waves from Rough Surfaces, The MacMillan Co., New York (1963).

30. Leader, J. C., "Multiple Scattering of Electromagnetic Waves from Rough Surfaces," J. Opt. Soc. Amer., 60, 1552 (1970).

31. Hunderi, O. and Beaglehole, D., "Study of the Interaction of Light with Rough Metal Surfaces. II. Theory," Phys. Rev., B.2, 321 (1970).

32. Houchens, A. F. and Hering, R. G., "Bidirectional Reflectance of Rough Metal Surfaces," Progress in Astronautics and Aeronautics, 20, 65, Academic Press, New York (1967).

33. Toporets, A. S., "Specular Reflection of Light from a Rough Surface," Opt. Spectry, 24, 62 (1968).

34. Gordinskii, G. M., "The Statistical Interference of Light upon Reflection from Matte-Glass Surfaces," Opt. Spectry, 15, 57 (1963).

35. Middleton, W. E. K. and Wyszecki, G., "Colors Produced by Reflection at Grazing Incidence from Rough Surfaces," J. Opt. Soc. Amer., 41, 1020 (1957).

36. Toporets, A. S., "Specular Reflection from a Rough Surface," Opt. Spectry, 16 54 (1964).

37. Pouey, M., Fabre, D., and Romand, J., "Indicatrices de Diffusion dans l'ultraviolet Lointain," Optica Acta, 15 159 (1968).

38. Vanetsian, R. A., Lebedeva, L. P., Krayushkina, V. A., and Ivanovskaya, A. S., "Diffusion Reflection of Laser Radiation," Soviet J. Opt. Tech., 36, 251 (1969).

39. Leader, J. C., "Bidirectional Scattering of Electromagnetic Waves from Rough Surfaces," McDonnell Douglas, MDC 70-022 (1970).

40. Voishvillo, N. A., "Reflection of Light by a Rough Glass Surface at Large Angles of Incidence of the Illuminating Beam," Opt. Spectry, 22, 517 (1967).

41. Torrance, K. E. and Sparrow, E. M., "Theory for Off-Specular Reflection from Roughened Surfaces," J. Opt. Soc. Amer., 57, 1105 (1967).

42. Look, D. C., Jr., and Love, T. J., "Investigation of the Effects of Surface Roughness upon Reflectance," Progress in Astronautics and Aeronautics, 24, 123, The MIT Press, Cambridge, Mass. (1970).

43. Smith, A. M., Müller, P. R., Frost, W., and Hsia, H. M., "Super- and Sub-Specular Maxima in the Angular Distribution of Polarized Radiation Reflected from Roughened Dielectric Surfaces," Progress in Astronautics and Aeronautics, 24, 249, The MIT Press, Cambridge, Mass. (1970).

44. Hering, R. G. and Smith, T. F., "Apparent Radiation Properties of a Rough Surface," Progress in Astronautics and Aeronautics, 23, 337, Academic Press, New York (1970).

45. Pouey, M., "Vacuum Ultraviolet Reflective Scattering Distributions," Optica Acta, 1, 105 (1969).

46. Treat, C. H. and Wildin, M. W., "Investigation of a Model for Bi-directional Reflectance of Rough Surfaces," Progress in Astronautics and Aeronautics, 23, 77, Academic Press, New York (1970).

47. Brandenberg, W. M., and Neu, J. T., "Unidirectional Reflectance of Imperfectly Diffuse Surfaces," J. Opt. Soc. Amer., 56, 97 (1966).

48. Miller, E. R. and Vun Kannon, R. S., "Development and Use of a Bi-directional Spectroreflectometer," Progress in Astronautics and Aeronautics, 20, 219, Academic Press, New York (1967).

49. Kruse, P. W., McGlauchlin, L. D., and McQuistan, R. B., Elements of Infrared Technology, John Wiley and Sons, New York (1962).

50. Smith, R. A., Jones, F. E., and Chasmar, R. P., Detection and Measment of Infrared Radiation, Oxford University Press, London (1957).

51. Simon, I., Infrared Radiation, D. Van Nostrand Co., Inc., Princeton, New Jersey (1966).

52. Forsythe, W. E., Measurement of Radiant Energy, McGraw-Hill, New York (1937).

53. Jenkins, F. A. and White, H. E., Fundamentals of Optics, McGraw-Hill, New York (1957).

54. Perkin-Elmer Instructional Manual, Vol. 3A, Model 112 Single Beam Double Pass Infrared Spectrometer (1956).

55. Plyler, E. K. and Peters, C. W., "Wavelengths for Calibration of Prism Spectrometers," J. Res., NBS 45, 462 (1950).

56. Acquista, N. and Plyler, E. K., "Calibrating Wavelengths in the Region from 0.6 to 2.6 Microns," J. Res., NBS 49, 13 (1952).

57. Downie, A. R., Magoon, M. C., Purcell, T., and Crawford, B., Jr., "The Calibration of Infrared Prism Spectrometers," J. Opt. Soc. Amer., 43, 941 (1953).

58. Fryer, R. E., "Computer Calibration of the Wavelength Drum of a Prism Spectrometer," App. Opt., 6, 275 (1967).

59. Birkebak, R. C., "Monochromatic Directional Distribution of Reflected Thermal Radiation from Roughened Surfaces," Ph.D. Dissertation, Mechanical Engineering Department, University of Minnesota, Minneapolis, Minnesota (1962).

60. Houchens, A. F., "Real Surface Effects on Radiative Heat Transfer," Ph.D. Dissertation, Department of Mechanical and Industrial Engineering, University of Illinois at Urbana-Champaign, Urbana, Illinois (1970).

61. Birkebak, R. C., "Optical and Mechanical RMS Surface Roughness Comparison," App. Opt., 10, 1970 (1971).

62. The Metal Analyst, Buehler Ltd., Evanston, Illinois (1965).

63. Dewitt, D. P., "Comments on the Surface Characterization of Real Metals," Symposium on Thermal Radiation of Solids, NASA SP-55, 141 (1965).

64. Funai, A. I. and Rolling, R. E., "Inspection Techniques for the Characterization of Smooth, Rough, and Oxidized Surfaces," Progress in Astronautics and Aeronautics, 20, 41, Academic Press, New York (1967).

65. Hass, G., "Optical Properties of Metals," American Institute of Physics Handbook, Second Edition, 6-103, McGraw-Hill, New York (1963).

66. Bennett, H. E., Bennett, J. M., and Ashley, E. J., "Infrared Reflectance of Evaporated Aluminum Films," J. Opt. Soc. Amer., 52, 1245 (1962).

67. Johari, O., "Total Materials Characterization with the Scanning Electron Microscope," Res./Dev., 12 (July 1971).

68. Stevison, D. F., "Effect of Surface Roughness on the Reflectance of Refractory Metals," AFML TR-66-232 (December 1966).

69. Wallach, J., "Surface Topography Description and Measurement," General Electric, Report No. 69-C-163 (1969).

70. Bendat, J. S. and Piersol, A. G., Measurement and Analysis of Random Data, John Wiley and Sons, New York (1966).

71. Torrance, K. E., "Off-Specular Peaks and Angular Distribution of Reflected Thermal Radiation," Ph.D. Dissertation, Mechanical Engineering Department, University of Minnesota, Minneapolis, Minnesota (1966).

72. Dunkle, R. V., Edwards, D. K., Gier, J. T., Nelson, K. E., and Roddick, R. D., "Heated Cavity Reflectometer for Angular Reflectance Measurements," Progress in International Research on Thermodynamic and Transport Properties, ASME, 541, Academic Press, New York (1962).

73. Birkebak, R. C., Dawson, J. P., McCullough, B. A., and Wood, B. E., "Hemispherical Reflectance of Metal Surfaces as a Function of Wavelength and Surface Roughness," Int. J. Heat Mass Transfer, 10, 1225, (1967).